# Numerical Simulations of Oil Spills and Wind Turbine Flows for Applications in Offshore Environmental Sustainability

by
Shuolin Xiao

A thesis submitted to the Department of Mechanical Engineering,
Cullen College of Engineering
in partial fulfillment of the requirements for the degree of

DOCTOR OF PHILOSOPHY

in Mechanical Engineering

Chair of Committee: Dr. Di Yang

Committee Member: Dr. Dong Liu

Committee Member: Dr. Rodolfo Ostilla Monico

Committee Member: Dr. Zheng Chen

Committee Member: Dr. Mostafa Momen

University of Houston
August 2020

# *Acknowledgements*

Firstly, I would like to express my sincere gratitude to my advisor Prof.Di Yang for the continuous support of my Ph.D study and related research, for his patience, motivation, and immense knowledge. His guidance helped me in all the time of research and writing of this thesis. I could not have imagined having a better advisor and mentor for my Ph.D study.

Besides my advisor, I would like to thank the rest of my thesis committees: Prof.Dong Liu, Prof.Mostafa Momen, Prof. Rodolfo Ostilla Monico and Prof. Zheng Chen, for their insightful comments and encouragement, but also for the hard question which incented me to widen my research from various perspectives.

I thank my labmates for research discussions, for the sleepless nights we were working together before deadlines, and for all the fun we have had in the last five years.

Last but not the least, I would like to thank my family: my parents and to my wife Yan Liu for supporting me spiritually throughout writing this thesis and my life in general....

# *Abstract*

Environmental sustainability has currently become one of the biggest issues faced by the mankind. The high demand of fossil fuel has resulted in considerable offshore oil drilling activities, significantly increasing the possibility of offshore oil spill accident. Specifically, the 2010 Deepwater Horizon accident has shocked the world with its severe adverse impact on the ocean ecosystem and the human society around the Gulf of Mexico. On the other hand, the technological advancement of floating turbines has made offshore wind a feasible resource to help supply the high energy demand. This doctoral dissertation covers three research topics related to offshore environmental sustainability, including the dynamics of multiphase buoyant plumes related to subsea hydrocarbon blowout, the effects of surface oil plume on upper-ocean radiative transfer related to the adverse impact of offshore oil spill on the ocean ecosystem, and the fluid dynamics of offshore floating wind farm for energy harvesting. A number of high-fidelity numerical simulation models are developed and applied to tackle these challenging problems, including the large-eddy simulation model for the oceanic and atmospheric turbulent flows, the Eulerian large-eddy simulation model for particle plume dispersion in ocean environment, the high-order spectral method for ocean waves, the Monte Carlo photon transport model for ocean radiative transfer, and the actuator disk model for wind turbines. The results show that the inherent properties of oil droplets including their size and rising velocity, under the background of cross-flow, will significantly affect their temporal-spatial distribution and the resulting photosynthesis within the ocean mixed layer. Besides, pitch motions will be induced on offshore wind turbines via their interaction with ocean surface wave, leading to modified wake flow statistics and power extraction rate compared with that on shore. Therefore, these findings can give guidance for fast-response strategy when oil spills happen and design of offshore wind turbines.

# Table of Contents

# List of Tables

# List of Figures

# Chapter 1

# Introduction

As the advancement of technology continues to rise, the natural resources have been unceasingly and increasingly depleted and degraded, imposing an urgent demand on the improvement of long-term environmental quality. Generally, the human activity regarding environmental sustainability can be divided into three categories, namely, pollution production, renewable resource utilization, and non-renewable resource consumption.

In particular, the pollution brought by oil spills spreading over habitats including the ocean or coastal waters is disastrous, by releasing tons of liquid petroleum hydrocarbon into the environment. Therefore, evaluation on the consequence of such emergency accident should be performed and effective response should be given in time, helping to minimize the entire influence on the environment as much as possible. Owing to the absorption properties of the oil droplets, as exhibited by their dark appearances, the photosynthesis of plankton should be significantly affected due to the limited radiation they received after the occurrence of oil spills. Meanwhile, the knowledge on the temporal and spatial distribution of these oil droplets under complex marine situation should be acquired in advance if possible, in order to identify their spreading pattern and employ an emergency response promptly and efficiently. To make things complex, the fate of these crude oils is determined by a lot of factors, including their size distribution, rising velocity, background crossflow, and the coupling between the surface wave and the turbulence underneath when the oil particles enter into the ocean mixing layer. These determinants are decided by not only the inherent properties of the crude oil in discharge, but also the marine environment far beyond the blowout point, thus bringing a far-ranging and long-term effect on the ecosystem. With a given distribution of oil droplets, the radiative transfer through the polluted seawater column is the function of the absorption and scattering properties of the seawater and crude oil mixture as well as the shape formed by surface wave when the radiation penetrates into the seawater from the air side. Consequently, the inclusion of simulating both the evolution of oil droplets and radiation transfer is challenging in terms of complexities and computational cost imposed.

Technically speaking, the dispersion of these petroleum hydrocarbon including oil droplets and bubbles can be tracked under the framework of fluid mechanics by treating the seawater as the carrier phase and oil droplets and bubbles as dispersed phases. This task can be fulfilled through an Euler-Lagrangian and Euler-Euler description, respectively, which are the cutting-edge technologies for multiple-phase flow modeling. However, the Euler-Lagrangian approach is extremely computationally costly, especially when the ocean environment is involved and make itself a large-scale problem, though this method can track each oil droplet and bubble individually. In comparison, Euler-Euler description follows the evolution of the disperse phase by dynamically obtaining its concentration field, which only characterizes the averaged features within a single computational cell–volume without losing the overall information about the disperse phase, thus exhibiting a relatively fast and low computation consumption. As for the carrier phase, the large-eddy simulation can model the detailed turbulence down to the computational cell with unresolved small-scale effects using the subgrid-scale models, which has been demonstrated efficiently for investigations on the oil spill related problems in previous studies. As a consequence, the behavior of the discharged liquid petroleum hydrocarbon can be well described and dynamically tracked with reasonable computational cost under the framework of large-eddy simulation in an Euler-Euler description. At a specified time, by Mie theory, the concentration distribution of the crude oil as well as the inherent optical properties of oil droplets and natural seawater will determine the absorption and scattering properties of the seawater and crude oil mixture. Afterwards, the information regarding radiative transfer can be obtained through Monte-Carlo simulation, which is favorable since it is easy to be programmed in a parallelized manner. Within the framework of Monte-Carlo simulation, the shape of surface wave can determine the deflected direction of radiation when the refraction happens after its penetration into the seawater at each initial position where the bundle of photons are launched. For each instantaneous surface wave, it can be obtained via high-order spectral-wave model, which can be coupled with the large-eddy simulation by serving as a top boundary condition.

As one of the clean and renewable energies, wind energy serves as an alternative to fossil energy without generation of greenhouse gases. Compared with onshore wind farms, offshore wind turbines can experience higher wind speeds and offer higher yields, making it a promising direction for current and future industrial power generation based on wind energy. This is due to the fact that atmospheric boundary layer is formed over open sea without any natural barriers or man made buildings, leaving more space available for offshore wind power installation. On the other hand, the extra presence of interaction between wind and ocean surface wave imposes a challenging task to obtain a optimized layout arrangement of single offshore wind turbines as well as large wind farms. Specifically, the offshore wind fields can be modulated considerably by the swell waves owing to their well-organized wave forms and large-amplitude orbital velocity, especially in the lower portion of the atmospheric boundary layer. Besides, the presence of swell wave will introduce an extra strong forcing to the offshore wind turbines platforms, building up a strong vibration mode on the entire system, which can further complicates the coupling between wind fields and ocean surface wave. Therefore, the wake-flow statistics behind the wind turbines and the resulting modulated wind-power extraction rate under the pitch motion of the platform should be investigated thoroughly to provide an insight on the design of offshore wind turbines and large wind farms. Numerically, the aforementioned problem can be described under the framework of large-eddy simulation, where the progression of the swell waves provides a dynamic bottom boundary condition with instantaneous sea-surface wave elevation and surface orbital velocity. These information can be obtained through high-order spectral-wave model, which are described in details in the following chapters. Furthermore, the effects of the wind turbines can be introduced via the actuator-disk model that imposes a turbine-induced force into the wind field.

# Chapter 2

# Large-Eddy Simulation of Bubble Plume in Stratified Crossflow

## 2.1 Introduction

When bubbles are released into the water, they drive the surrounding water to rise together as a multiphase plume. Underwater release of multiphase bubble/fluid mixed plume can occur naturally can occur naturally (e.g., natural petroleum seeps from seafloor [121, 154]), artificially (e.g., reservoir destratification and aeration systems [7, 79, 123, 164]), or accidentally (e.g., subsea wellhead blowout accidents [20, 152]). The dynamics of the bubble-driven plume near the source of the subsea release is strongly affected by the bubble-induced buoyancy effect and the stable water stratification [7, 133, 136]. During the plume rising process, ambient water gets entrained into the plume by the turbulent eddies at the edge of the plume and lifted to higher elevations. In a stably stratified water environment (i.e., the water density decreases gradually towards higher elevation), the net buoyancy of the plume decreases with height due to the increasing density difference between the lifted water within the plume and ambient water around the plume. The reduced buoyancy eventually results in the detrainment of the entrained water at a height of maximum rise (named the peel height, $h_p$), and a falling plume is formed outside the rising inner plume [7, 133, 136]. The detrained water falls as a downward plume to a neutral buoyancy level (named the trap height, $h_t$), and then disperses horizontally to form an intrusion layer [7, 130].

Asaeda & Imberger [7] performed water tank experiments of bubble-driven plumes in stratified

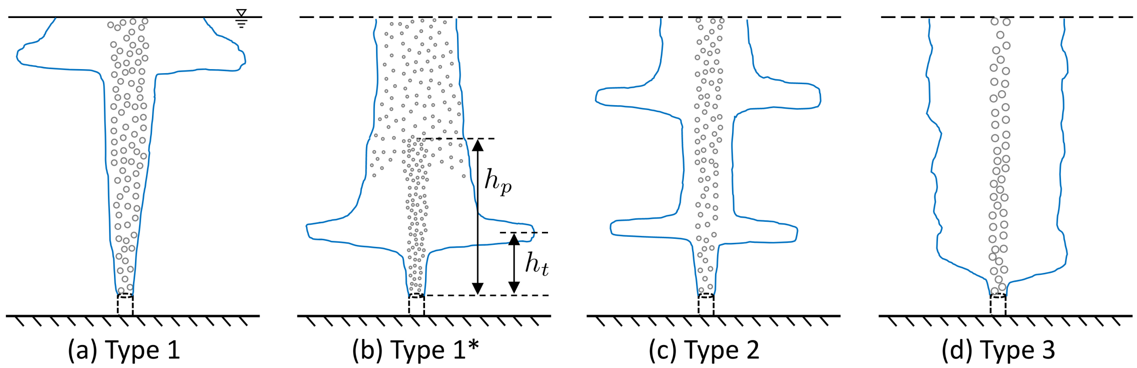


Figure 2.1: Schematic of plume structure types in stratified water without crossflow based on the plume classification defined by Asaeda & Imberger [7] and Socolofsky, Crounse & Adams [135].

water without crossflow and classified the plume structures into three types. In this classification, Type 1 plume has a large gas flow rate and weak stratification, allowing the plume to reach the water surface directly without forming the peeling event [Fig. 2.1(a)]; Type 2 plume has moderate gas flow rate and water stratification, resulting in distinct peeling events to form stable intrusion layers [Fig. 2.1(c)]; Type 3 plume has low gas flow rate and strong stratification, resulting in irregular peeling process and unstable intrusion [Fig. 2.1(d)].

By performing a large set of laboratory experiments, Socolofsky, Crounse & Adams [135] and Socolofsky & Adams [130, 136] further extended and generalized the plume classification of Asaeda & Imberger [7]. They found that the plume structure can be classified based on a key dimensionless parameter, i.e., the dimensionless bubble rise velocity defined as [130, 135, 136]

$$W_N = w_r/(B_0 N)^{1/4}, \tag{2.1}$$

where $w_r$ is the bubble rise velocity, $B_0$ is the kinematic buoyancy flux induced by the bubble source, and $N$ is the buoyancy frequency of the stratified water. For fixed $B_0$ and $N$, the value of $W_N$ increases when $w_r$ increases, which can be realized by increasing the size of the released bubbles. Socolofsky & Adams [130, 136] used sufficient water depths in their experiments so that the Type 1 plume [Fig. 2.1(a)] did not occur. Instead, they observed a new Type 1* plume when $W_N < 1.5$ [136], which usually occurs when the plume is driven by small bubbles that have small rise velocity relative to the surrounding water. As illustrated in Fig. 2.1(b), the small bubbles accumulate above the source to form a strong buoyancy flux and drive the plume to rise. When the plume reaches the peeling region, the lateral flow motions associated with the peeling process widen the bubble plume diameter and reduce the bubble mass concentration. Above the peel height, although the small bubbles can continue to drive the plume, the reduced bubble mass concentration results in a weakened buoyancy flux that is insufficient to form distinct intrusion beyond the first peel height. As the dimensionless rise velocity further increases to $1.5 < W_N < 2.4$ [136], the plume falls into the Type 2 category [Fig. 2.1(c)]. The major difference between Type 2 and Type 1* plumes is that the bubbles in Type 2 plume has sufficient buoyancy and rise velocity to resist the lateral diffusion at the peel height and maintain the bubble concentration beyond the first peel height, which allows the formation of successive intrusion layers if the water depth is sufficient [Fig. 2.1(c)]. As $W_N$ further increase to $W_N > 2.4$ (usually for plume with large bubbles), the plume becomes Type 3 with irregular peeling and unsteady intrusion [136]. This plume classification based on $W_N$ [130, 135, 136] has been successfully applied to classify the plume structures in several recent studies [e.g., 31, 44, 133, 134, 170].

In an open water environment, crossflow often occurs and can further complicate the dynamics of the bubble-driven multiphase plume [e.g., 37, 133, 152, 179]. As shown in Fig. 2.2(a), a strong crossflow can tilt the bubble column and entrained water stream in the multiphase plume at different angles away from the vertical direction due to their different vertical velocities, causing them to quickly separate at a critical height $h_s$ above the plume source [131]. After the separation from the bubble column, the further transport of the plume flow may be tracked and modeled relatively easily without the influence of the bubble buoyancy [37]. If the crossflow is relatively weak [Fig. 2.2(b)], the bubbles and entrained water flow in the plume cannot be separated directly by the crossflow before the multiphase plume reaches the peel height [131], resulting in inclined rising/falling double-plume structure with increased complexity in the plume dynamics due to the crossflow. Socolofsky & Adams [131] performed a large number of experiments to study bubble-driven plumes in both unstratified and stratified crossflows. They observed the plume structures from the side using the laser-induced fluorescence method. It should be noted that most of their reported experiments were for plumes in unstratified crossflow, and only four exploratory cases (i.e. no crossflow, as well as weak, moderate and strong crossflows) with water stratification were

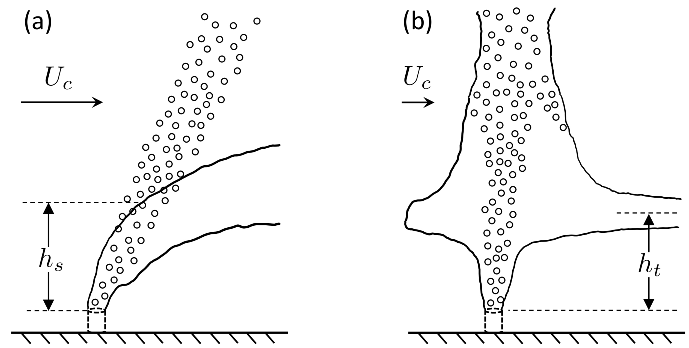


Figure 2.2: Schematic of plume structures in stratified water with (a) strong and (b) weak crossflows. Here, $U_c$ denotes the crossflow velocity, $h_s$ denotes bubble and water plumes separation height [131], and $h_t$ denotes the trap height of the detrained water [130, 131].

included to illustrate the complex plume dynamics in stratified crossflow. Although these limited number of experiments provided valuable insights about the macroscopic plume structures in stratified crossflow, they did not provide the three-dimensional characteristics of the plumes or the simultaneous information of the velocity, bubble and dye concentration fields. To date, the detailed plume dynamics under stratified crossflow conditions is still not well understood.

In recent years, large-eddy simulation (LES) has become a valuable numerical tool for modeling the detailed turbulent flow physics in buoyant plumes [e.g., 26, 35, 36, 43, 46, 47, 58, 168]. LES captures the unsteady turbulent plume dynamics over a range of spatial and temporal scales down to the computational grid scale, and models the unresolved small-scale effects using the subgrid-scale (SGS) models [94]. Among different strategies for modeling the multiphase bubble-driven plumes, the Eulerian–Eulerian approach has been widely adopted due to its relatively low computational cost [134]. In the Eulerian–Eulerian approach, the water in and around the plume is treated as a continuous phase and its turbulent flow motions are modeled in LES by solving the filtered Navier–Stokes equations; the bubble field is treated as a dispersed particle phase and described using a Eulerian concentration function, and its evolution is modeled by solving a filtered advection–diffusion equation. The Eulerian–Eulerian LES approach has been successfully applied in several recent studies to model the buoyant multiphase plumes in stratified water environment [e.g., 26, 43, 44, 168–170].

In this chapter, the dynamics of bubble-driven plume in stably stratified water with crossflow is modeled using the Eulerian–Eulerian LES bubble plume model developed in previous study

[170]. The simulations focus on conditions with relatively weak crossflow, aiming at capturing the rich dynamics of the plume when it is affected by both the stratification and the crossflow. Three different crossflow speeds are considered, i.e., $U_c = 0.5$, 1 and 2 cm/s. For each crossflow speed, four plume conditions with different bubble rise velocities are considered, i.e., $w_r = 3$, 6, 12 and 20 cm/s, for which the corresponding dimensionless rise velocity based on Eq. (2.1) are $W_N = 0.53$, 1.06, 2.12, and 3.53, respectively. As discussed in detail in Sec. 2.3, these simulation cases are set up such that the weak crossflow does not force the bubbles and the entrained water stream to separate too early, allowing the bubble/water mixed plume to have sufficient interaction with the stratified water to form the intrusion. Moreover, a reference case without crossflow is also simulated for $w_r = 6$ cm/s for comparison purpose. Based on the LES results, both the instantaneous and time-averaged plume structures from the various simulation cases are compared to elucidate the effects of crossflow on the plume characteristics. The interactions of the bubble-driven plume with water stratification and crossflow also strongly affect how materials carried by the plume are dispersed into the surrounding water. To track the material transport process, a dye tracer is released into the plume and its transport is simulated in the LES by solving the filtered advection–diffusion equation for the dye concentration. The statistics of the dye fluxes due to both the mean flow and turbulence are quantified, and the results for different simulation cases are compared.

The remainder of this chapter is organized as follows. The LES model is described in detail in Sec. 2.2. The configurations of the simulation cases are discussed in Sec. 2.3. The simulations and statistical analysis results are reported in Sec. 2.4. Finally, conclusions are given in Sec. 2.5.

## 2.2 Large-eddy simulation model description

The current LES model uses the Cartesian coordinate system defined as $\mathbf{x} = (x, y, z)$, where $x$ and $y$ are the horizontal coordinates and $z$ is the vertical coordinate. The corresponding velocity vector is denoted as $\mathbf{u} = (u, v, w)$. In the LES model, the water flow in and around the plume is modeled as a continuous phase carrier flow, which is governed by the filtered Navier–Stokes equations [1, 170],

$$\nabla \cdot \widetilde{\mathbf{u}} = 0 \tag{2.2}$$

and

$$\frac{\partial \widetilde{\mathbf{u}}}{\partial t} + \widetilde{\mathbf{u}} \cdot \nabla \widetilde{\mathbf{u}} = -\frac{1}{\rho_0} \nabla \widetilde{P} - \nabla \cdot \boldsymbol{\tau}^d + \left(1 - \frac{\widetilde{\rho}}{\rho_0}\right) g \mathbf{e}_z + \left(1 - \frac{\rho_b}{\rho_0}\right) \frac{\widetilde{C}_b}{\rho_b} g \mathbf{e}_z. \tag{2.3}$$

Here, the tilde denotes the variable resolved by the LES computational grid; $\rho_0$ is the reference water density; $\widetilde{\rho}$ is the resolved local water density; $\rho_b$ is the density of air in the bubbles; $g$ is the gravitational acceleration; $\mathbf{e}_z$ is the unit vector in the vertical direction; $\widetilde{C}_b$ is the resolved mass concentration of air bubbles; $\tau^d = \tau - [\mathrm{tr}(\tau)/3]\mathbf{I}$ is the deviatoric part of the subgrid-scale stress tensor $\tau = \widetilde{\mathbf{u}\mathbf{u}} - \widetilde{\mathbf{u}}\widetilde{\mathbf{u}}$, where $\mathrm{tr}(\tau)$ is the trace of $\tau$ and $\mathbf{I}$ is the identity tensor; and $\widetilde{P} = \widetilde{p} + \rho_0[\mathrm{tr}(\tau)/3 + (\widetilde{\mathbf{u}} \cdot \widetilde{\mathbf{u}})/2 - gz]$ is the modified pressure, where $\widetilde{p}$ is the resolved water pressure. The last two terms in Eq. (2.3) are the buoyancy forces due to water stratification and bubble concentration, respectively, which are modeled based on the Boussinesq approximation [26, 170].

Following previous LES studies [e.g., 26, 70, 92, 115, 169, 170], the water density stratification is modeled by simulating a temperature field $\theta$ governed by a filtered convection–diffusion equation

$$\frac{\partial \widetilde{\theta}}{\partial t} + \nabla \cdot (\widetilde{\mathbf{u}}\widetilde{\theta}) = -\nabla \cdot \boldsymbol{\pi}_\theta \tag{2.4}$$

and the density field $\widetilde{\rho}$ is assumed to vary linearly with $\widetilde{\theta}$ as

$$\widetilde{\rho} = \rho_0[1 - \alpha_t(\widetilde{\theta} - \theta_0)], \tag{2.5}$$

where $\boldsymbol{\pi}_\theta = \widetilde{\mathbf{u}\theta} - \widetilde{\mathbf{u}}\widetilde{\theta}$ is the SGS thermal flux, $\alpha_t$ is the thermal expansion coefficient, and $\theta_0$ is the reference temperature corresponding to the reference water density $\rho_0$.

In the current LES model, the bubbles are modeled as a dispersed phase transported by the carrier flow, with their instantaneous local concentration being described by a continuous Eulerian concentration function $C_b(\mathbf{x}, t)$. The evolution of the concentration field is simulated by solving a filtered transport equation,

$$\frac{\partial \widetilde{C}_b}{\partial t} + \nabla \cdot (\widetilde{\mathbf{v}}_b \widetilde{C}_b) = -\nabla \cdot \boldsymbol{\pi}_b + q_b, \tag{2.6}$$

where $\widetilde{\mathbf{v}}_b$ is the Lagrangian transport velocity of bubbles, $\boldsymbol{\pi}_b = \widetilde{\mathbf{u}C_b} - \widetilde{\mathbf{u}}\widetilde{C}_b$ is the SGS flux of bubble mass concentration, and $q_b$ is a volumetric source term representing the release of the air bubbles from a localized source (being zero outside the source region). The bubble transport velocity $\widetilde{\mathbf{v}}_b$ is modeled as [26, 45, 170]

$$\widetilde{\mathbf{v}}_b = \widetilde{\mathbf{u}} + w_r \mathbf{e}_z + \frac{w_r}{g}\frac{\mathrm{D}\widetilde{\mathbf{u}}}{\mathrm{D}t}, \tag{2.7}$$

where $w_r$ is the rise velocity of bubbles relative to the surrounding carrier flow caused by the bubble buoyancy, and $\mathrm{D}\widetilde{\mathbf{u}}/\mathrm{D}t = \partial\widetilde{\mathbf{u}}/\partial t + \widetilde{\mathbf{u}} \cdot \nabla\widetilde{\mathbf{u}}$ is the material derivative (or Lagrangian acceleration) of the carrier flow velocity. Following previous study [187], the bubble rise velocity is parameterized based on

$$w_r = \frac{\mathrm{Re}_b \mu}{\rho_0 d}, \tag{2.8}$$

where $\mu$ is the water viscosity and $d$ is the equivalent spherical diameter of the bubble. The particle Reynolds number $\mathrm{Re}_b$ can be parameterized in explicit function form as [32]

$$\begin{cases} \begin{aligned} \mathrm{Re}_b = \;& N_D/24 - 1.7569 \times 10^{-4} N_D^2 \\ & +6.9252 \times 10^{-7} N_D^3 \\ & -2.3027 \times 10^{-10} N_D^4, && \text{if } N_D \leq 73, \\ \log_{10}\mathrm{Re}_b = \;& -1.7095 + 1.33438W - 0.11591W^2, && \text{if } 72 < N_D \leq 580, \\ \log_{10}\mathrm{Re}_b = \;& -1.81391 + 1.34671W - 0.12427W^2 \\ & +0.006344W^3, && \text{if } 580 < N_D \leq 1.55 \times 10^7, \end{aligned} \end{cases} \tag{2.9}$$

where $N_D = 4\rho_0(\rho_0 - \rho_b)gd^3/3\mu^2$ and $W = \log_{10} N_D$.

In addition, the transport of dye tracers is also simulated in the LES model to capture the effects of the plume dynamics and crossflow on transporting materials. The evolution of the dye mass concentration field $\widetilde{C}_{dye}$ is governed by the filtered transport equation

$$\frac{\partial\widetilde{C}_{dye}}{\partial t} + \nabla \cdot \left(\widetilde{\mathbf{u}}\widetilde{C}_{dye}\right) = -\nabla \cdot \boldsymbol{\pi}_{dye} + q_{dye}, \tag{2.10}$$

where $q_{dye}$ is a source term for the dye release and $\boldsymbol{\pi}_{dye} = (\widetilde{\mathbf{u}C_{dye}} - \widetilde{\mathbf{u}}\widetilde{C}_{dye})$ is the SGS dye concentration flux. Unlike the bubbles, the concentration function of the dye tracers is transported by the carrier flow as a passive scalar, thus the resolved carrier flow velocity $\widetilde{\mathbf{u}}$ is used in the convective term in Eq. (2.10).

Similar to prior LES studies of bubble-driven plumes [e.g., 26, 43, 44, 112, 170], the molecular viscosity and molecular diffusivity terms are omitted in the filtered LES governing equations (2.3), (2.4), (2.6) and (2.10) due to their negligible effects compared with the corresponding SGS flux terms. The LES governing equations are closed by parameterizing the SGS terms with proper turbulence closures. In particular, the SGS stress tensor $\boldsymbol{\tau}^d$ is parameterized using the Lilly–Smagorinsky eddy-viscosity type model [86, 128], $\boldsymbol{\tau}^d = -2\nu_{sgs}\widetilde{\mathbf{S}}$, where $\widetilde{\mathbf{S}} = [\nabla\widetilde{\mathbf{u}} + (\nabla\widetilde{\mathbf{u}})^T]/2$ is the resolved strain rate tensor, $\nu_{sgs} = (c_s\Delta)^2|\widetilde{\mathbf{S}}|$ is the modeled SGS eddy viscosity, $c_s$ is the Smagorinsky model coefficient, and $\Delta$ is the LES grid (filter) scale. The value of $c_s$ is determined dynamically during the simulation using the Lagrangian-averaged scale-dependent dynamic SGS model [15]. The SGS fluxes of the scalar quantities are then parameterized as $\boldsymbol{\pi}_\theta = -(\nu_{sgs}/\mathrm{Pr}_{sgs})\nabla\widetilde{\theta}$, $\boldsymbol{\pi}_b = -(\nu_{sgs}/\mathrm{Sc}_{sgs})\nabla\widetilde{C}_b$, and $\boldsymbol{\pi}_{dye} = -(\nu_{sgs}/\mathrm{Sc}_{sgs})\nabla\widetilde{C}_{dye}$, with the constant SGS Prandtl number $\mathrm{Pr}_{sgs} = 0.4$ and SGS Schmidt number $\mathrm{Sc}_{sgs} = 0.4$ [6, 24, 73, 89, 99, 147, 170].

The current LES model uses a hybrid numerical scheme for solving the governing equations for the flow and scalar field evolutions. For the flow field, Eqs. (2.2) and (2.3) are discretized by the pseudo-spectral method in the horizontal directions on collocated grids and the second-order central finite difference method in the vertical direction on staggered grids [3]. The velocity field is advanced in time by the second-order Adams–Bashforth scheme. The divergence-free constraint of the velocity field is ensured by solving the pressure field from a Poisson equation constructed based on Eq. (2.2). The pressure is then used to project the predicted velocity field onto the divergence-free space. Equation (2.4) is also discretized by the hybrid pseudo-spectral and finite difference method and integrated in time by the second-order Adams–Bashforth scheme.

Unlike the flow equations, Eqs. (2.6) and (2.10) are for the spatially nonhomogeneous bubble and dye concentration fields and are not discretized by the pseudo-spectral method. Instead, they are discretized by a finite-volume method developed by previous study [23], which uses the carrier flow velocity field interpolated from the pseudo-spectral/finite-difference flow solver's computational grids to the finite-volume grids of the scalar field solver based on a constrained interpolation scheme that conserves the velocity divergence-free condition. The LES solver for Eqs. (2.6) and (2.10) uses a bounded third-order upwind scheme for the advection term [49] and advances in time using the second-order Adams–Bashforth scheme [23]. Although the bounded finite-volume

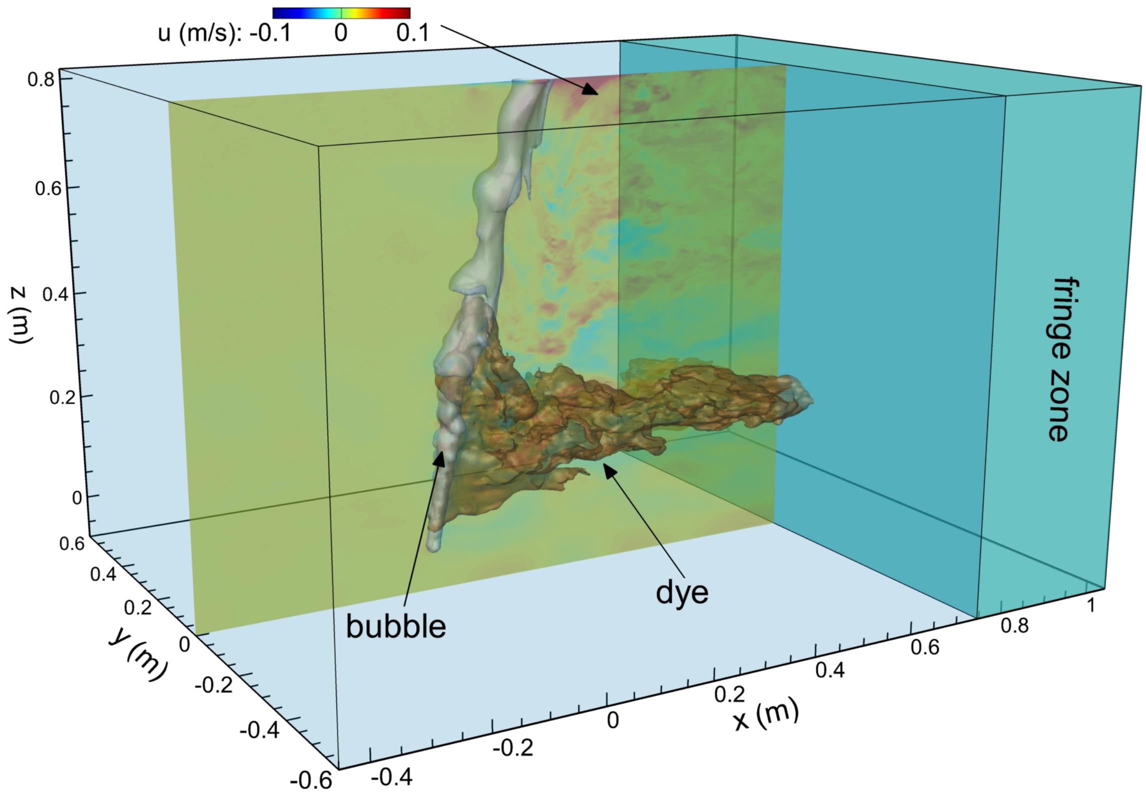


Figure 2.3: Three dimensional instantaneous plume for case W6U2.

method induces additional numerical dissipation to the LES scalar solver, it provides the necessary boundedness to the simulated particle concentration field to suppress the occurrence of numerical oscillation that may result in unphysical negative concentration [23]. The current hybrid LES model uses the dissipative finite-volume method only for the particle concentration field, while uses the pseudo-spectral method combined with the advanced LASD SGS model to reserve the high-order accuracy of the simulated turbulent flow velocity and temperature fields. The current hybrid LES model has been successfully applied in several prior studies of particle transport in turbulent flows and showed good agreements with experimental data and theoretical predictions [e.g., 1, 22, 24, 109, 110].

The pseudo-spectral method used in the current LES is based on the Fourier series transformation, which typically requires periodic boundary conditions in the horizontal directions. In order to enable the application of inflow/outflow conditions in the streamwise direction for modeling the plume interacting with a crossflow, in this study the fringe zone method [12, 28, 124] is adopted. As illustrated in Fig. 2.3, a fringe zone of finite streamwise thickness adjacent to the outflow boundary of the simulation domain is used to force the velocity field back to its value at the inflow boundary, which allows the simulation of the non-periodic flow using the periodic pseudo-spectral flow solver. Specifically, let $x_{fr}$ and $x_{out}$ be the $x$ coordinates for the starting location of the fringe zone and the outflow boundary of the simulation domain, respectively. The velocity within the fringe zone $x_{fr} \leq x \leq x_{out}$ is imposed as $\widetilde{\mathbf{u}}(x, y, z) = \widetilde{\mathbf{u}}(x_{fr}, y, z)[1 - f(x)] + (U_c \mathbf{e}_x) f(x)$, where $U_c$ is the imposed crossflow speed in the $x$ direction at the inflow boundary, $\mathbf{e}_x$ is the unit vector in the $x$ direction, and $f(x) = 0.5 - 0.5 \cos[\pi(x - x_{fr})/(x_{out} - x_{fr})]$ is the fringe function. Similar fringe zone method has been successfully applied in the Fourier-series-based pseudo-spectral LES model for simulating non-periodic turbulent flows past trees [e.g., 27, 28] and wind turbines [e.g., 142, 143].

In the simulation, the top boundary of the simulation domain is kept flat, where the free-slip and impermeability conditions (i.e. $\partial \widetilde{u}/\partial z = \partial \widetilde{v}/\partial z = 0$ and $\widetilde{w} = 0$) are used for the velocity field. At the top boundary, a no-flux condition ($\partial \widetilde{C}_{dye}/\partial z = 0$) is used for the dye concentration field, and an outflux condition ($\Phi_s = w_r \widetilde{C}_b|_{surface}$) is used to let the gas leave the simulation domain through the top boundary. Similar top surface conditions have been used in previous study [170]. The bottom boundary of the simulation domain is set to be flat, where the free-slip and impermeability conditions are applied for the velocity field and the no-flux condition is used for both the bubble and dye concentrations. Recently, the current LES solver with the fringe zone method and similar top and bottom boundary conditions has also been successfully applied to model the dynamics of oil jet in crossflow [1], and good agreement with the data of a towing tank experiment [101] was obtained.

## 2.3 Configuration of simulation cases

The physical parameters of the simulations are chosen to be similar to those used in the previously reported laboratory experiment and numerical simulations [125, 170]. In all the simulation cases, the computational domain height is set to be $H = 0.9\,\mathrm{m}$. The air bubbles with density $\rho_b = 1.4\,\mathrm{kg/m^3}$ are released at a total volume release rate of $Q_b = 1.5 \times 10^{-6}\,\mathrm{m^3/s}$ from a localized source at 0.08 m above the bottom boundary. This source location mimics the typical laboratory experimental condition in which the plume source is placed at some distance above the bottom of the water tank to avoid significant influence of the bottom boundary on the plume dynamics [e.g., 7, 75, 101, 125, 131, 186]. Similar configuration of plume source location has also been used in other recent LES studies [1, 170]. The corresponding kinematic buoyancy flux induced by the bubble source is $B_s = gQ_b(\rho_0 - \rho_b)/\rho_0 = 1.47 \times 10^{-5}\,\mathrm{m}^4/\mathrm{s}^3$, where $\rho_0 = 1000\,\mathrm{kg/m}^3$. By setting the origin of the coordinate system to be at the center of the bubble releasing source, the vertical domain ranges from $z = z_{bot} = -0.08\,\mathrm{m}$ to $z = z_{top} = 0.82\,\mathrm{m}$. The air bubble source is smeared smoothly using a super Gaussian function over a finite cylindrical volume of $V_s = \pi b_s^2 h$, with a source radius $b_s = 7\,\mathrm{mm}$ and a height $h = 6.25\,\mathrm{mm}$ (i.e., two times of the vertical grid size, which is specified below).

The water in the simulation domain is linearly stratified from $z = -0.08\,\mathrm{m}$ (bottom) to $z = 0.72\,\mathrm{m}$ with a constant density gradient of $\partial\rho/\partial z = -50\,\mathrm{kg/m}^4$, which corresponds to a buoyancy frequency of $N = \sqrt{-(g/\rho_0)\partial\rho/\partial z} = 0.7\,\mathrm{s}^{-1}$. The top 0.1 m of the simulation domain has a uniform water density of $\rho_0 = 1000\,\mathrm{kg/m}^3$ to mimic the effect of the surface mixed layer in oceans and large water reservoirs. This uniform density layer helps to prevent the plume flow from reflecting back to the lower portion of the simulation domain by the top surface to ensure that the observed plume phenomena are governed by the interaction between the bubble-driven plume and the stratified crossflow. Similar setup of water stratification with a top layer of uniform water density has also been used in previous experimental and numerical studies of bubble-driven plumes [e.g., 125, 170].

The passive scalar dye is released into the center of the plume at a height of 3.75 cm (i.e. 12 vertical grid sizes) above the air bubble source with a mass release rate of $Q_{dye} = 6.45 \times 10^{-3}\,\mathrm{mg/s}$. This slight upward shift of the dye release source with respect to the bubble source results in the dye being injected at a location where the plume has gain sufficient vertical velocity to carry the dye. Otherwise, if the dye was released at the same location as the bubbles, the dye plume would be fractionated due to the weak upward plume velocity with respect to the imposed crossflow at the source location. A considerable fraction of dye would be carried away directly from the source by the crossflow, which would not only reduce the available amount of dye for tracing the plume dynamics, but also directly contaminate the lower portion of the dye concentration field generated by the plume dynamics.

As listed in Table 2.1, four different bubble rise velocities are considered in this study, i.e. $w_r = 3$, 6, 12 and 20 cm/s. These rise velocities correspond to the equivalent bubble diameters of $d = 0.31$, 0.53, 1.01 and 2.02 mm, respectively, based on the empirical parameterization shown in Eqs. (2.8) and (2.9). It should be noted that the current LES model uses $w_r$ as the input parameter in Eq. (2.7). The corresponding bubble equivalent diameters $d$ may be slightly different if a different parameterization of $w_r(d)$ is used for the estimation, which does affect the simulation results since $d$ is not directly used as an input parameter in the LES model. The corresponding values of the dimensionless bubble rise velocity based on Eq. (2.1) for the four $w_r$ are $W_N = 0.53$, 1.06, 2.12 and 3.53, respectively. These conditions cover the three representative plume categories according to the plume classification identified in the previous experimental studies [130, 131, 136]: (1) the cases with $W_N = 0.53$ and 1.06 fall into the Type-1* regime, in which the distinct peeling event occurs and the bubble column above it is dispersed horizontally due to the radial motion of the peeling flow; (2) the case with $W_N = 2.12$ is in the Type-2 regime, in which the distinct peeling event occurs but the bubble column remain narrow above it; (3) the case with $W_N = 3.53$ is in the Type-3 regime, in which the peeling events become unstable and occur continuously along the rising plume.

Note that due to the additional effect of the crossflow, the actual plume structures for the four $W_N$ cases considered in this study are expected to be different from the schematics shown in Fig. 2.1(b–d) that are for the plumes without crossflow. For each bubble condition, three different crossflow speeds are investigated, i.e. $U_c = 0.5$, 1 and 2 cm/s. In addition, a reference case without crossflow is also considered for $w_r = 6$ cm/s. Each simulation case is named in terms of the corresponding bubble rise velocity and crossflow speed [see Table 2.1]. For example, the case with $w_r = 3$ cm/s and $U_c = 0.5$ cm/s is referred to as case Wr3-Uc05. These relatively weak crossflow speeds are chosen to ensure that the crossflow does not force the bubbles and the entrained water stream in the plume to separate too early so that the bubble/water mixed plume can have sufficient interaction with the stratified water to generate the peeling and intrusion. For Type 1* and Type 2 plumes that have distinct peeling process, the strength of the crossflow may be estimated based on the critical separation height $h_{s,0}$ with the plume peel height $h_{p,0}$. Here, $h_{s,0}$ denotes the bubble/water separation height in the crossflow without stratification, which can be estimated based on the empirical parameterization from Socolofsky & Adams [131], i.e.,

$$h_{s,0} = \frac{5.1 B_0}{(U_c w_r^{2.4})^{0.88}} \,, \tag{2.11}$$

and $h_{p,0}$ denotes the peel height for plume in stratified water without crossflow, which can be estimated based on the empirical parameterization from Socolofsky & Adams [136], i.e.,

$$h_{p,0} = 5.2 \left( \frac{B_0}{N^3} \right)^{1/4} \exp \left\{ -\frac{1}{10.1} \left[ \frac{w_r}{(B_0 N)^{1/4}} - 1.8 \right]^2 \right\} \,. \tag{2.12}$$

As suggested by Socolofsky & Adams [131] and Socolofsky, Adams & Sherwood [133], the plume structure is dominated by the crossflow effect if $h_{s,0} < h_{p,0}$ and by the stratification effect if $h_{s,0} > h_{p,0}$. As shown in Table 2.1, the condition $h_{s,0} > h_{p,0}$ is satisfied for the cases with $w_r = 3$ and 6 cm/s, suggesting that the stratification effect dominates in these cases. On the other hand, for the cases with $w_r = 12$ and 20 cm/s, the estimated $h_{s,0}$ are comparable smaller than $h_{p,0}$, suggesting that the crossflow is expected to generate more significant impact on the plume dynamics. Overall, the three crossflow conditions considered here fall into the weak crossflow category [131]. As shown by the simulation results in Sec. 2.4, although the crossflow can tilt the plume, it is not strong enough to force the bubble/water separation and prevent the plume peeling process from occurring. In all the reported cases, the bubble-driven plume interacts with the stratified water to create the peeling process and form the rising/falling double plume structure.

As illustrated in Fig. 2.3, for the simulation cases with crossflow, the horizontal domain dimensions are set to be $L_x = 1.5$ m and $L_y = 1.2$ m for the $x$ and $y$ directions, respectively. The simulation domain is discretized using $N_x \times N_y \times N_z = 320 \times 256 \times 289$ grid points, with even grid spacing in each direction. In the $x$ direction, a uniform streamwise velocity $U_c$ is imposed at the inflow boundary at 0.45 m upstream from the bubble source. The last 0.3 m of the streamwise domain is set to be the fringe zone for imposing the outflow condition, as explained in Sec. 2.2. For case Wr6-Uc0 without the crossflow, the simulation domain is set to be $(L_x, L_y, H) = (1.5, 1.5, 0.9)$ m, which has equal dimensions in the $x$ and $y$ directions. No fringe zone is used in case Wr6-Uc0. To have identical grid resolution as other simulation cases with the crossflow, the simulation domain in case Wr6-Uc0 is discretized using $N_x \times N_y \times N_z = 320 \times 320 \times 289$ grid points. The bubble

Table 2.1: Key parameters for the LES cases.

| Case ID | $w_r$ (cm/s) | $U_c$ (cm/s) | $B_0$ ($m^4/s^3; 10^{-5}$) | $N$ ($s^{-1}$) | $W_N$ | $h_{p,0}$ (m) | $h_{s,0}$ (m) |
|---|---|---|---|---|---|---|---|
| Wr3-Uc05 | 3 | 0.5 | 1.47 | 0.7 | 0.53 | 0.36 | 13.06 |
| Wr3-Uc1 | 3 | 1 | 1.47 | 0.7 | 0.53 | 0.36 | 7.10 |
| Wr3-Uc2 | 3 | 2 | 1.47 | 0.7 | 0.53 | 0.36 | 3.86 |
| Wr6-Uc0 | 6 | 0 | 1.47 | 0.7 | 1.06 | 0.40 | $\infty$ |
| Wr6-Uc05 | 6 | 0.5 | 1.47 | 0.7 | 1.06 | 0.40 | 3.02 |
| Wr6-Uc1 | 6 | 1 | 1.47 | 0.7 | 1.06 | 0.40 | 1.64 |
| Wr6-Uc2 | 6 | 2 | 1.47 | 0.7 | 1.06 | 0.40 | 0.89 |
| Wr12-Uc05 | 12 | 0.5 | 1.47 | 0.7 | 2.12 | 0.42 | 0.70 |
| Wr12-Uc1 | 12 | 1 | 1.47 | 0.7 | 2.12 | 0.42 | 0.38 |
| Wr12-Uc2 | 12 | 2 | 1.47 | 0.7 | 2.12 | 0.42 | 0.21 |
| Wr20-Uc05 | 20 | 0.5 | 1.47 | 0.7 | 3.53 | 0.31 | 0.24 |
| Wr20-Uc1 | 20 | 1 | 1.47 | 0.7 | 3.53 | 0.31 | 0.13 |
| Wr20-Uc2 | 20 | 2 | 1.47 | 0.7 | 3.53 | 0.31 | 0.07 |

source in case Wr6-Uc0 is located at the center of the horizontal domain at the same depth as in other simulation cases with crossflow. All the 13 simulation cases included in this study have the same grid resolution of $(\Delta x, \Delta y, \Delta z) = (4.6875, 4.6875, 3.125)$ mm.

## 2.4 Results

### 2.4.1 Instantaneous plume characteristics

Figures 2.4 shows the instantaneous plume for case Wr6-Uc05, where the thick solid lines are the iso-lines of $C_b = 0.001\,\mathrm{kg/m^3}$, which are used to indicate the shape and location of the bubble column and these indications apply in figures listed in this subsection. The basic dynamics of the bubble-driven plume in stably stratified water can be seen from the scalar and velocity fields of this case. Due to their smaller density than the surrounding water, the air bubbles rise towards the water surface along a column, which is slightly tilted towards the $+x$ direction due to the crossflow. The bubble-induced buoyancy also drives the water around the bubble source to rise together as a plume of water/bubble mixture. The turbulent eddies at the edge of the plume cause entrainment of surrounding water into the plume when it rises through the stably stratified water, and lift the higher density water to higher elevations where the ambient water has a lower density. This density

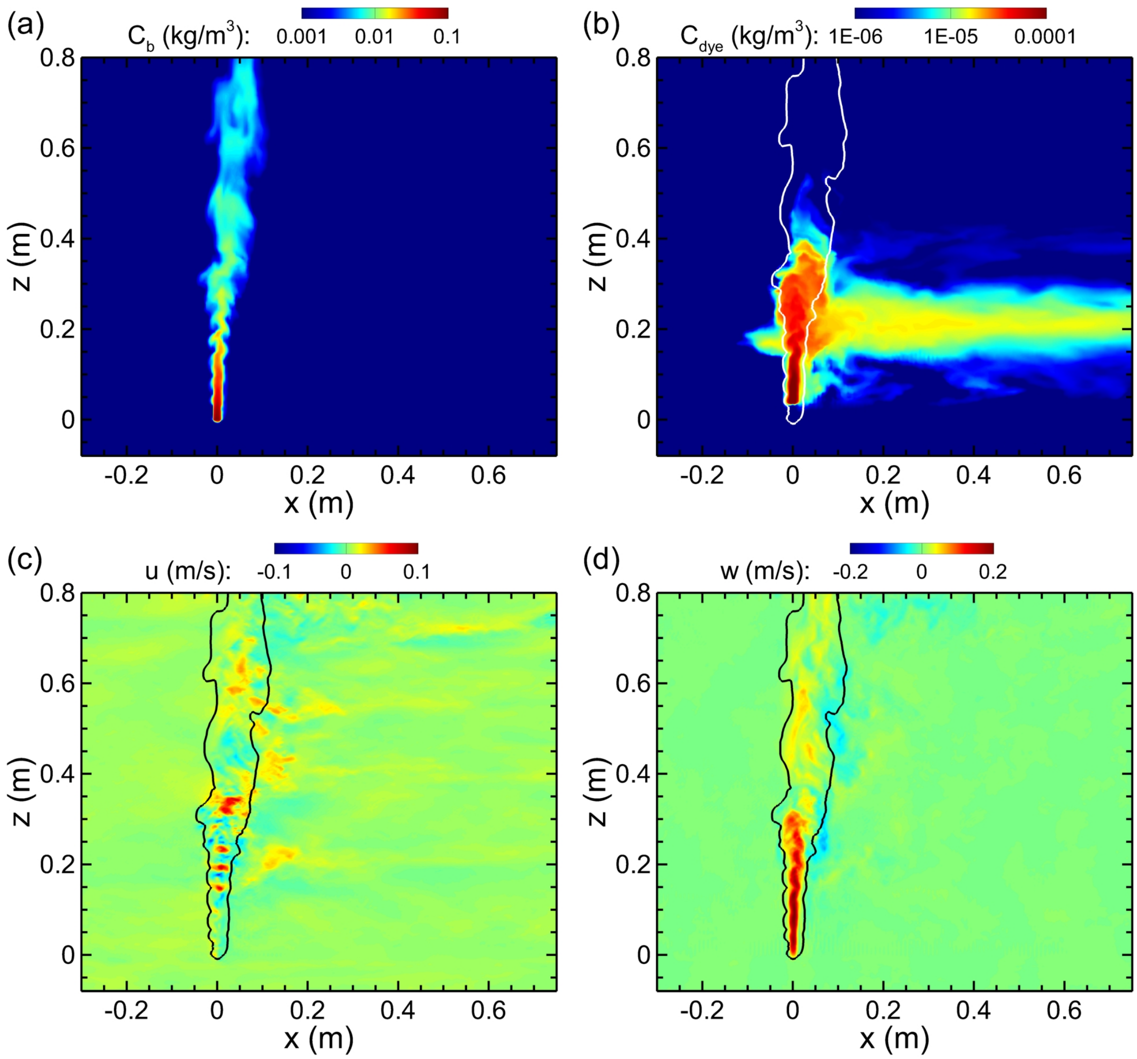


Figure 2.4: Instantaneous plume velocity and scalar fields on the $(x, z)$-plane across the source location for case Wr6-Uc05 (i.e. $w_r = 6\,\mathrm{cm/s}$, $U_c = 0.5\,\mathrm{cm/s}$): (a) bubble concentration $C_b$; (b) dye concentration $C_{dye}$; (c) streamwise velocity $u$; (d) vertical velocity $w$.

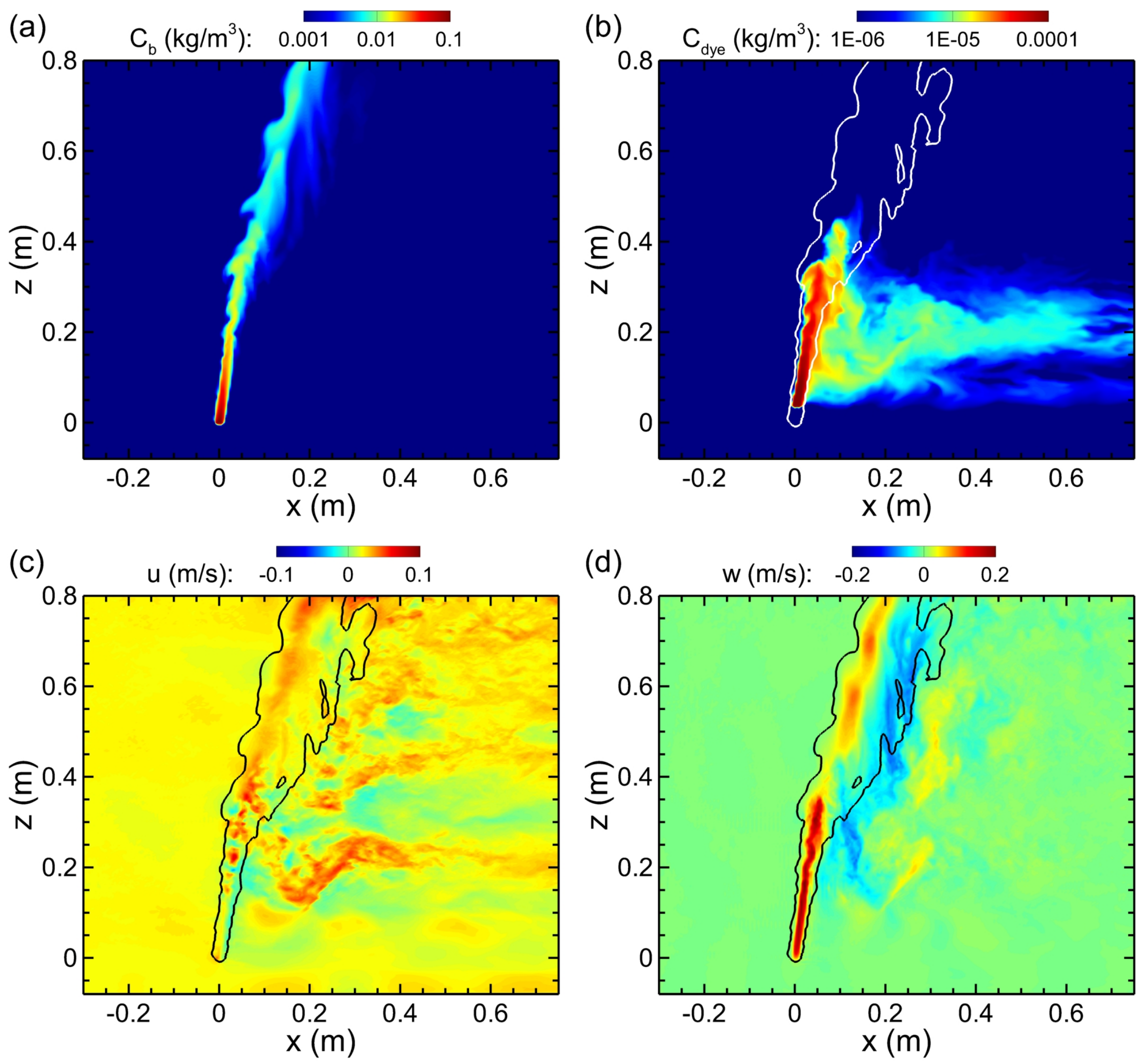


Figure 2.5: Instantaneous plume velocity and scalar fields on the $(x, z)$-plane across the source location for case Wr6-Uc2 (i.e. $w_r = 6\,\mathrm{cm/s}$, $U_c = 2\,\mathrm{cm/s}$): (a) bubble concentration $C_b$; (b) dye concentration $C_{dye}$; (c) streamwise velocity $u$; (d) vertical velocity $w$.

difference results in a downward force to act against the buoyancy induced by the bubbles, which eventually causes the water flow in the plume to lose the upward momentum and detrain from the bubble column at the peel height (i.e. the maximum elevation of the entrained water [136]) around $z = 0.4\,\mathrm{m}$. The detrained water fall as a downward plume to the neutral buoyancy level, and then continue to move horizontally in the $+x$ direction to form an intrusion layer at around $z = 0.2\,\mathrm{m}$.

Note that if there is no crossflow, the bubble/water plume would rise almost vertically and the detrained water would form an annular plume to fall along the outside of the rising plume [7, 130, 170]. With the weak crossflow of $U_c = 0.5\,\mathrm{cm/s}$, the overall plume structure in case Wr6-Uc05 is no longer axisymmetric and the development of the intrusion layer biases heavily towards the downstream direction of the crossflow, with weak intrusion towards the upstream direction. If the crossflow becomes faster, as shown in Fig. 2.5 for case Wr6-Uc2, the overall plume structure further tilts towards the downstream direction of the crossflow. With the $U_c = 2\,\mathrm{cm/s}$ crossflow speed, the intrusion towards the upstream direction is completely prohibited. In case Wr6-Uc2, the detrained water falls at a higher speed than that in case Wr6-Uc05 [Fig. 2.5(d) versus Fig. 2.4(d)]. This is because the faster crossflow tilts the bubble/water plume sufficiently away from being vertical, allowing the downward plume to fall on the downstream side of the rising plume with less contact. Compared to case Wr6-Uc05, the dye concentration in the intrusion layer in case Wr6-Uc2 is more diluted, with noticeable horizontal transport of dye directly away from the lower part of the plume by the crossflow. The bubble column in case Wr6-Uc2 also shows a clear increase of tilt angle at the peel height (around $z = 0.4\,\mathrm{m}$) as the peeling process expands the bubble column and dilutes the bubble concentration, resulting in smaller upward velocity for the plume above the peel height [Fig. 2.5(d)].

Changing the bubble rise velocity also affects the dynamics of the plume in the crossflow. Figures 2.6 and 2.7 show the instantaneous plumes for cases Wr20-Uc05 and Wr20-Uc2, respectively. Compared to the cases with smaller bubble rise velocity of $w_r = 6\,\mathrm{cm/s}$, the bubble columns in the cases with $w_r = 20\,\mathrm{cm/s}$ exhibit less horizontal dispersion and smaller tilt angle because of the stronger buoyancy of the larger bubbles. Note that the cases with $w_r = 20\,\mathrm{cm/s}$ have the same dimensionless rise velocity of $W_N = 3.53$, which falls in the plume category of Type-3 featuring

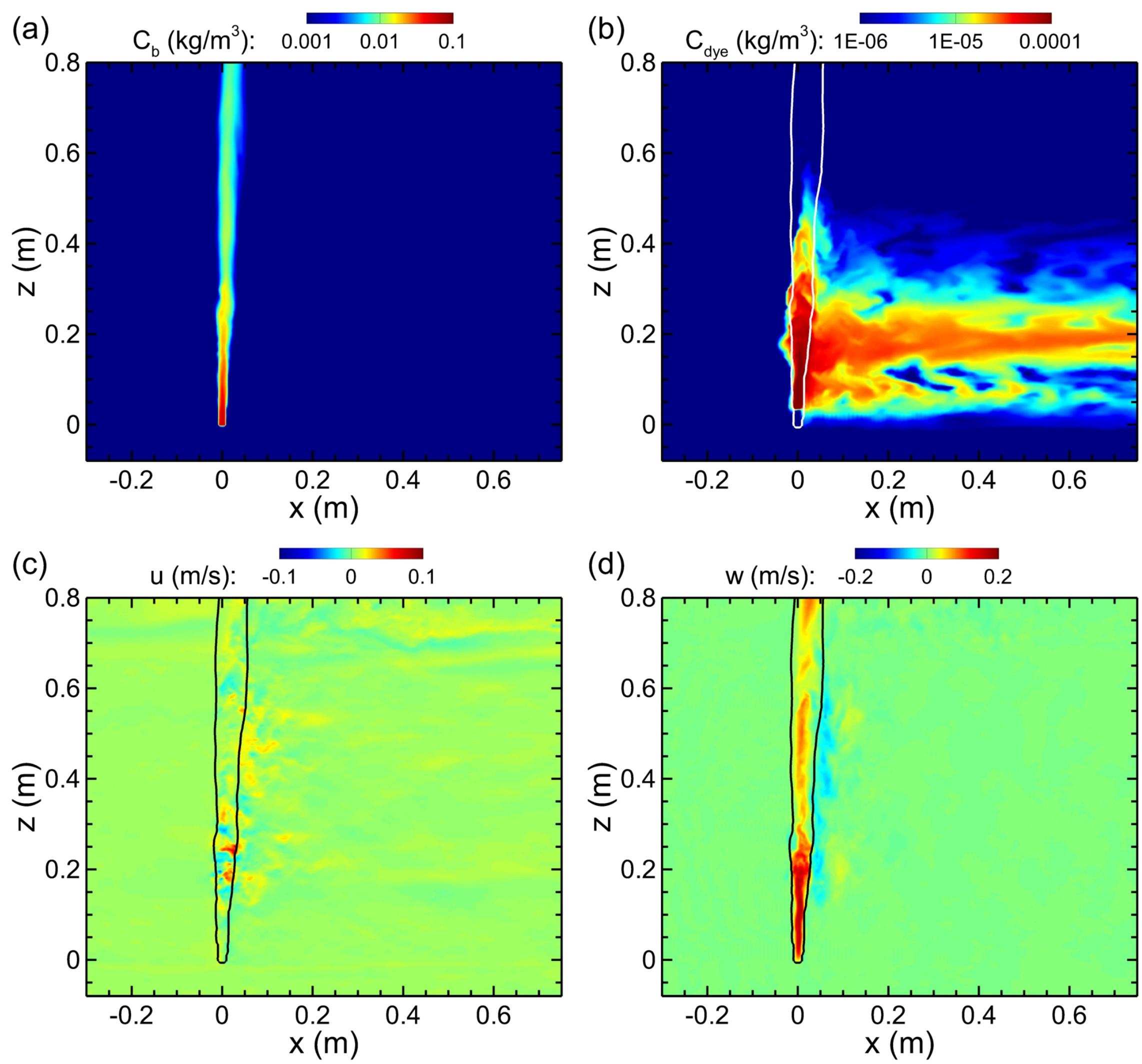


Figure 2.6: Instantaneous plume velocity and scalar fields on the $(x, z)$-plane across the source for case Wr20-Uc05 (i.e. $w_r = 20\,\mathrm{cm/s}$, $U_c = 0.5\,\mathrm{cm/s}$): (a) bubble concentration $C_b$; (b) dye concentration $C_{dye}$; (c) streamwise velocity $u$; (d) vertical velocity $w$.

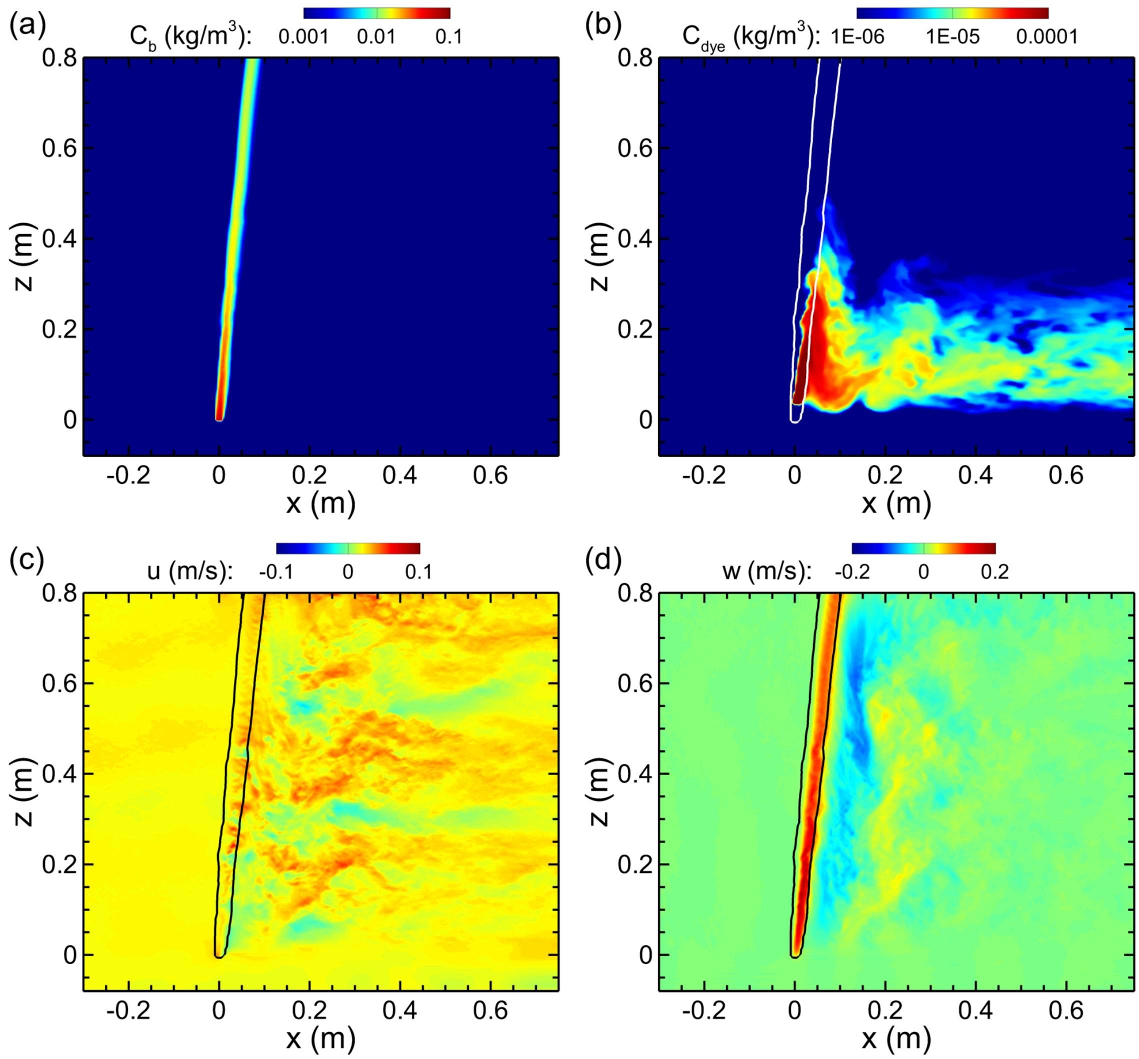


Figure 2.7: Instantaneous plume velocity and scalar fields on the $(x, z)$-plane across the source for case Wr20-Uc2 (i.e. $w_r = 20\,\mathrm{cm/s}$, $U_c = 2\,\mathrm{cm/s}$): (a) bubble concentration $C_b$; (b) dye concentration $C_{dye}$; (c) streamwise velocity $u$; (d) vertical velocity $w$.

unstable continuous peeling process along the edge of the rising plume [130, 131, 136]. The combination of the unstable peeling in cases Wr20-Uc05 and Wr20-Uc2 with the crossflow causes a considerable amount of dye to leak from the plume at a wide range of heights, resulting in more vertical spreading of the dye intrusion layer than that in the cases with $w_r = 6\,\mathrm{cm/s}$ [see Figs. 2.6(b) and 2.7(b) versus Figs. 2.4(b) and 2.5(b)]. The comparison between cases Wr20-Uc05 and Wr20-Uc2 also shows that the increase of crossflow speed causes the plume in case Wr20-Uc2 to be further tilted towards the $+x$ direction, resulting in a stronger falling plume on the downstream side of the rising plume [Figs. 2.6(d) and 2.7(d)] that pushes the upper edge of the intrusion layer to a lower elevation than that in case Wr20-Uc05 [Figs. 2.6(b) and 2.7(b)].

### 2.4.2 Mean plume statistics

The instantaneous plume field exhibits considerable fluctuations in velocities and scalar concentrations due to the turbulence effect of the plume flow as well as the unsteadiness of the peeling process [125]. Here the time average is performed to obtain the mean plume field, which helps to illustrate the effect of crossflow on the averaged plume structure and material transport. Hereinafter, the time average of a physical quantity $f$ is denoted as $\overline{f}$.

Figure 2.8 shows the time-averaged dye concentration for the plume of $w_r = 6\,\mathrm{cm/s}$ with four different crossflow speeds of $U_c = 0$, 0.5, 1 and $2\,\mathrm{cm/s}$. For case Wr6-Uc0 [Fig. 2.8(a)], without the presence of crossflow, the time-averaged dye concentration is nearly axisymmetric about the plume center axis. The spatial distribution of the dye concentration shows that a main peeling event occurs at around $z = 0.4\,\mathrm{m}$, causing most of the initially entrained water to detrain from the rising plume (as indicated by the much lower dye concentration further above) and fall to the neutral buoyancy level to form the thin intrusion layer at around $z = 0.2\,\mathrm{m}$. Only a very small fraction of entrained water continues to rise upward and gets fully trapped by a secondary peeling/intrusion process in the region at $0.4 z 0.6\,\mathrm{m}$. For case Wr6-Uc05 [Fig. 2.8(b)], the weak crossflow of $U_c = 0.5\,\mathrm{m/s}$ significantly suppresses the upstream intrusion (i.e., towards the $-x$ direction) and slightly increases the vertical expansion of the primary intrusion layer at around $z = 0.2\,\mathrm{m}$ on the downstream side of the plume. The trace of the secondary peeling/intrusion process can be seen from the horizontal intrusion of the dye at around $z = 0.4\,\mathrm{m}$, which has much

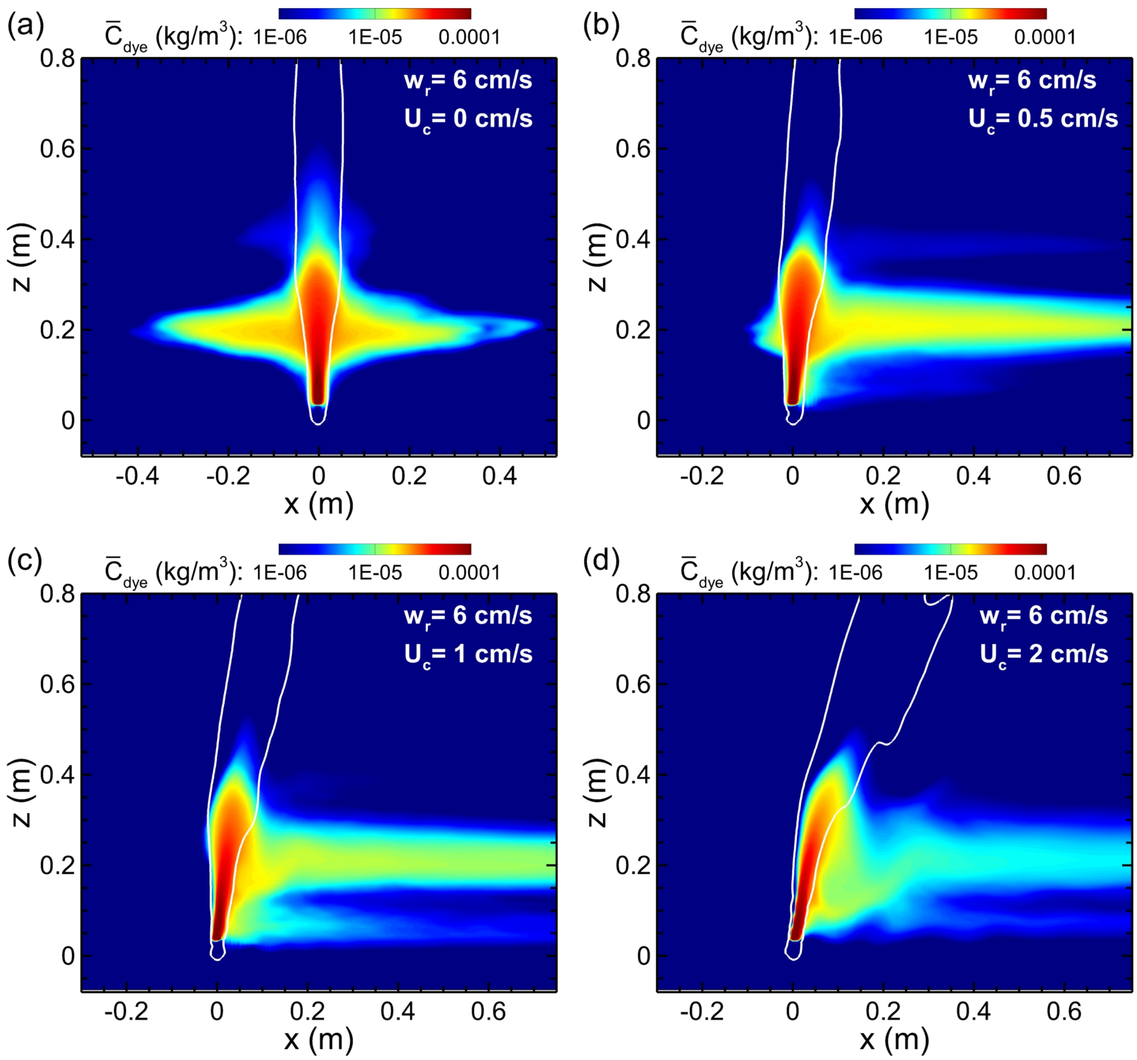


Figure 2.8: Time-averaged plumes on the $(x, z)$-plane across the source for $w_r = 6\,\text{cm}$: (a) Wr6-Uc0; (b) Wr6-Uc05; (c) Wr6-Uc1; (d) Wr6-Uc2. The color contours are for the time-averaged dye concentration.

lower dye concentration than that in the main intrusion layer. As the crossflow speed further increases, in cases Wr6-Uc1 [Fig. 2.8(c)] and Wr6-Uc2 [Fig. 2.8(d)], nearly all the initially entrained water detrains from the rising plume at the peel height around $z = 0.4\,\mathrm{m}$, and no clear sign of secondary peeling/intrusion process is observed further above. Instead, a secondary intrusion layer is found to extend directly from the bottom stem of the rising plume at around $z = 0.08\,\mathrm{m}$ due to the direct diffusion of water and dye away from the rising plume by the crossflow.

Figure 2.9 compares the time-averaged dye concentration for the plumes of $w_r = 3$, 6, 12 and $20\,\mathrm{cm/s}$ with the same crossflow speed of $U_c = 2\,\mathrm{cm/s}$. Similar to the observation from the instantaneous plume fields shown in Figs. 2.5 and 2.7, the time-averaged plumes shown in Fig. 2.9 also exhibit different characteristics under the same crossflow condition when the bubble rise velocity is changed. In particular, the mean bubble columns in cases Wr3-Uc2 and Wr6-Uc2 are clearly affected by both the peeling process and the crossflow, exhibiting an expansion of the bubble column width and an increase of its tilt angle above the peel height above around $z = 0.4\,\mathrm{m}$. Some bubbles in case Wr3-Uc2 are also pushed down quite a bit by the falling plume from the peeling event, as indicated by the convex bubble concentration iso-line shown in Fig. 2.9(a) at around $(x, z) = (0.2, 0.25)\,\mathrm{m}$. In cases Wr3-Uc2 and Wr6-Uc2, most of the dye is carried into the primary intrusion layer at around $z = 0.2\,\mathrm{m}$, but the secondary intrusion layer at the lower elevation around $z = 0.08\,\mathrm{m}$ is still noticeable. As the bubble rise velocity increases to $w_r = 12\,\mathrm{cm/s}$ in case Wr12-Uc2 [Fig. 2.9(c)], the primary peeling process occurs at a lower elevation near $z = 0.3\,\mathrm{m}$, and the narrow rising plume also releases water and dye continuously into the crossflow at low elevation. As a result, the dye concentration in the secondary intrusion layer at around $z = 0.08\,\mathrm{m}$ reaches a comparable level as that in the primary intrusion layer at around $z = 0.2\,\mathrm{m}$. In case Wr20-Uc2 [Fig. 2.9(d)], the unstable and continuous peeling processes completely dominate and the dye is transported by the crossflow into a continuous intrusion layer ranging from about $z = 0.02$ to $0.3\,\mathrm{m}$, with higher dye concentration near the lower elevation.

The presence of crossflow can break the axisymmetry of the bubble-driven plume, causing the flow and dye concentration fields to have more complex three-dimensional (3D) features. To illustrate these 3D features of the time-averaged plume structure, in Fig. 2.10 the iso-surfaces

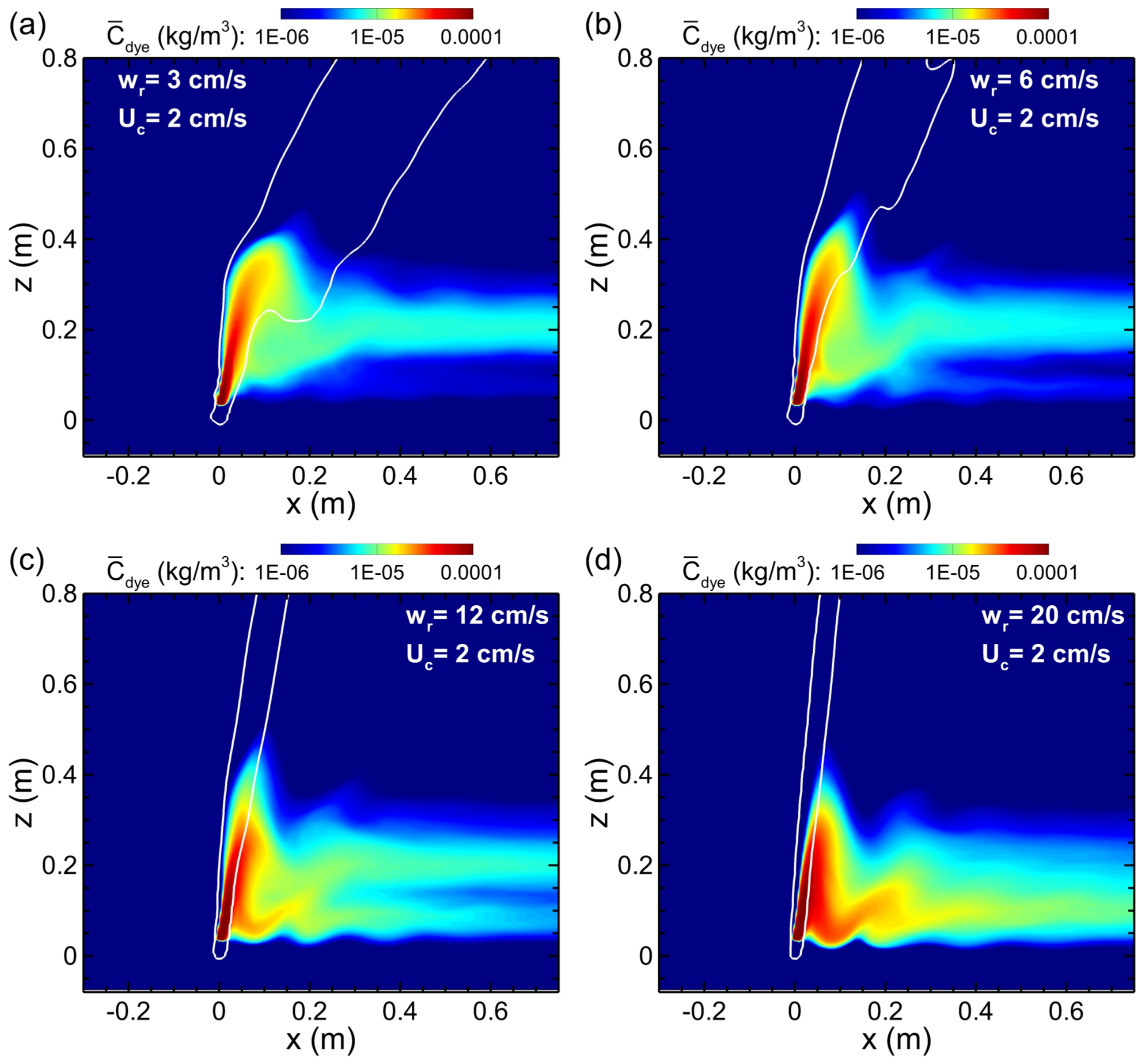


Figure 2.9: Time-averaged plumes on the $(x, z)$-plane across the source for $U_c = 2\,\text{cm}$: (a) Wr3-Uc2; (b) Wr6-Uc2; (c) Wr12-Uc2; (d) Wr20-Uc2. The color contours are for the time-averaged dye concentration.

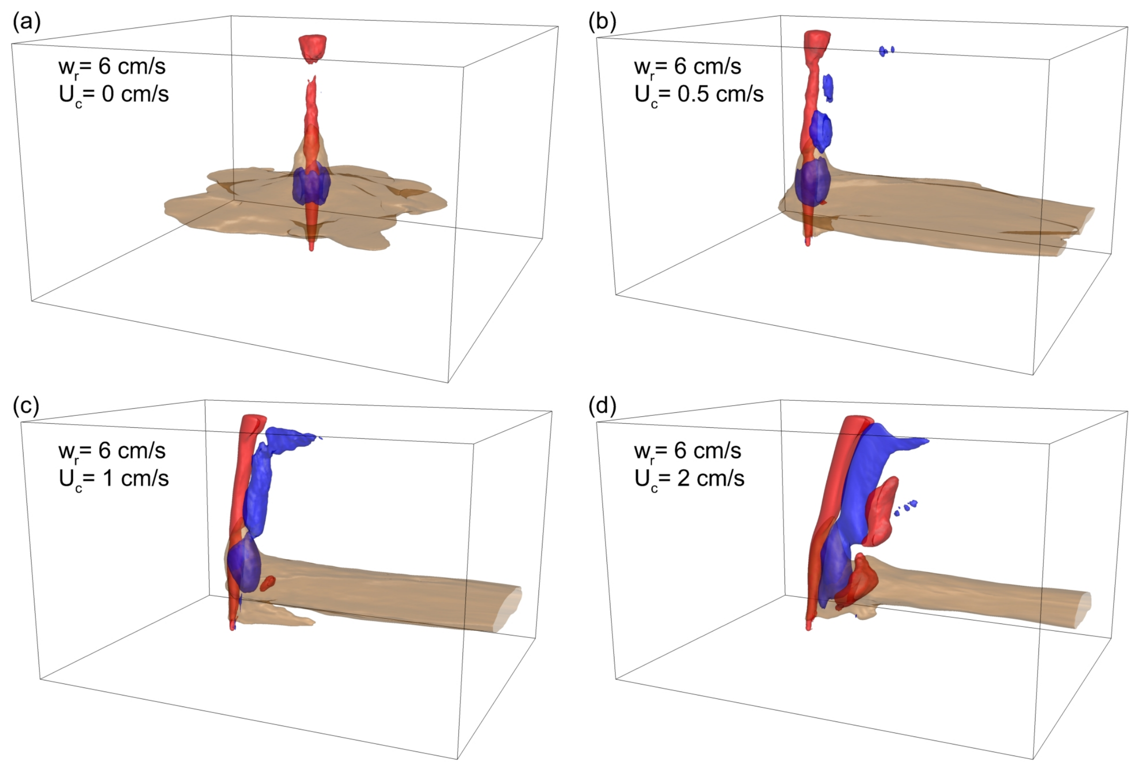


Figure 2.10: Time-averaged 3D plumes for $W_r = 6\,\mathrm{cm}$: (a) Wr6-Uc0; (b) Wr6-Uc05; (c) Wr6-Uc1; (d) Wr6-Uc2. The red iso-surfaces are for $\overline{w} = 1.5\,\mathrm{cm/s}$, the blue ones are for $\overline{w} = -1.5\,\mathrm{cm/s}$, and $\overline{C}_{dye} = 4\,\mathrm{mg/m^3}$ is indicated by brown.

of the flow vertical velocity and dye concentration of the time-averaged plumes are plotted together. Figure 2.10(a) shows the 3D mean plume structure for case Wr06-Uc0. Without the crossflow, the overall mean plume structure in case Wr06-Uc0 appears to be quite symmetric about the central axis of the plume, including the straight rising plume (indicated by the red-colored iso-surfaces of $\overline{w} = 1.5\,\mathrm{cm/s}$), the annular falling plume (indicated by the blue-colored iso-surfaces of $\overline{w} = -1.5\,\mathrm{cm/s}$), and the pancake-shaped intrusion layer (indicated by the brown-colored iso-surfaces of $\overline{C}_{dye} = 4\,\mathrm{mg/m^3}$). Note that the time-averaged plume shown in Fig. 2.10(a) is not perfectly axisymmetric. This is as expected because the instantaneous plume snapshots for time average are sampled from only one LES run. Assemble averaging using additional independent instantaneous samples of the turbulent plume field are needed, which can be obtained by performing separate LES runs with different small disturbance added into the initial condition of the LES. Moreover, the box shape of the computational domain in case Wr06-Uc0 also makes it difficult to obtain perfect axisymmetric plume. Nevertheless, the simulation result from case Wr06-Uc0 can still serve as a reference to help illustrate the effect of crossflow on the 3D plume characteristics.

Figure 2.10(b–d) shows the time-averaged 3D plume for $w_r = 6\,\mathrm{cm/s}$ under the three different crossflow conditions. As the crossflow speed increases, the falling plume shifts more towards the downstream side (with respect to the crossflow) of the rising plume, causing the falling plume to no longer surround the rising plume. This reduced contact causes the magnitude of the vertical flow velocity in both the rising and falling plumes to become greater, as indicated by the increase of volumes enclosed by the iso-surfaces of $\overline{w} = \pm 1.5\,\mathrm{cm/s}$ shown in Fig. 2.10(b–d). Note that in case Wr06-Uc2 [Fig. 2.10(d)], the high vertical velocity in the falling plume causes it to overshoot, resulting in another rising flow on the downstream side of the falling plume to bring the water back to the neutral buoyancy elevation. The shape of the intrusion layer also exhibits significant variation as the crossflow speed increases. In case Wr06-Uc05 with $U_c = 0.5\,\mathrm{cm/s}$ [Fig. 2.10(b)], the intrusion layer (indicated by the brown-colored iso-surfaces of dye concentration) is narrow in the vertical direction and wide in the spanwise direction. As the crossflow speed further increases, the vertical expansion of the intrusion layer further increases while the spanwise width decreases, confining the intrusion of water and dye into a narrow tube-shaped region [Fig. 2.10(c,d)].

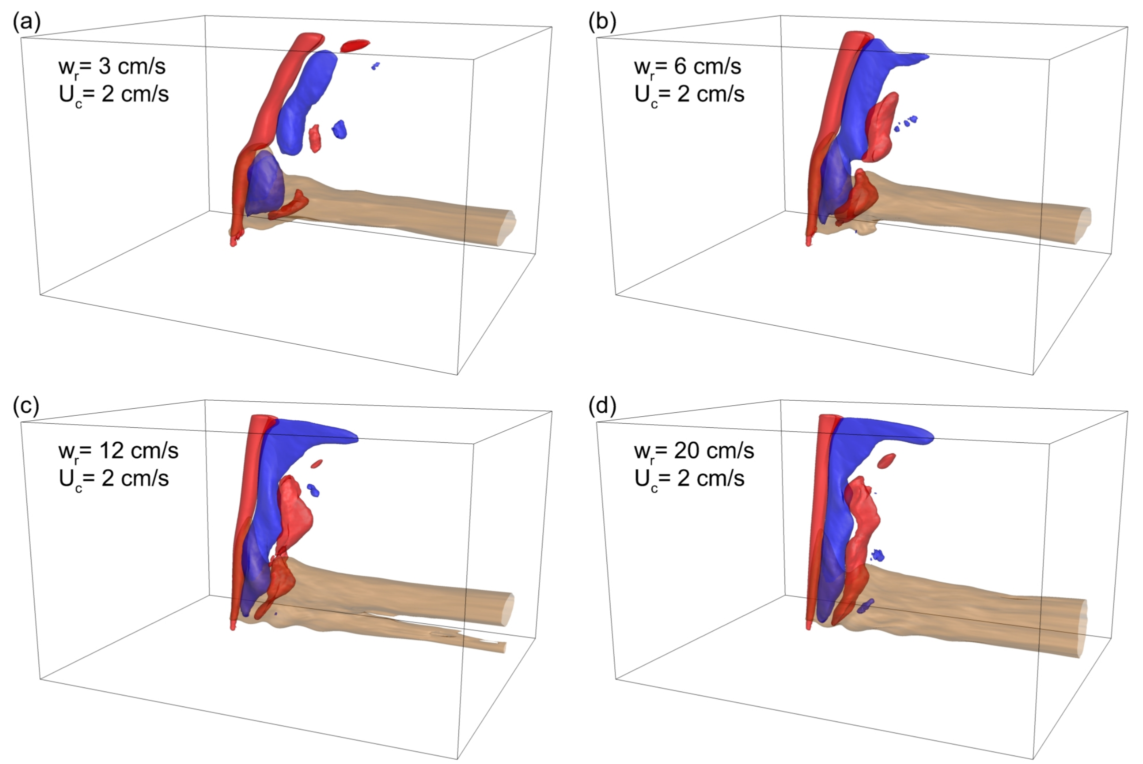


Figure 2.11: Time-averaged 3D plumes for $U_c = 2\,\mathrm{cm}$: (a) Wr3-Uc2; (b) Wr6-Uc2; (c) Wr12-Uc2; (d) Wr20-Uc2. The red iso-surfaces are for $\overline{w} = 1.5\,\mathrm{cm/s}$, the blue ones are for $\overline{w} = -1.5\,\mathrm{cm/s}$, and $\overline{C}_{dye} = 4\,\mathrm{mg/m^3}$ is indicated by brown.

Figure 2.11 shows the time-averaged 3D plumes for the four different bubble rise velocities under the same crossflow condition of $U_c = 2\,\mathrm{cm/s}$. As the bubble rise velocity increases, the plume varies from having a strong distinct peeling event in case Wr3-Uc2 to form the isolated falling plume below the peel height [Fig. 2.11(a)], to having a continuous peeling process in case W20-Uc2 to form the continuous and smooth falling plume from bottom to top along the downstream side of the rising plume [Fig. 2.11(d)]. For all the four cases shown in Fig. 2.11, the $2\,\mathrm{cm/s}$ crossflow confines the spanwise width of the intrusion region. Cases Wr3-Uc2 and Wr6-Uc2 exhibit similar tube-shape intrusion region [Fig. 2.11(a,b)]. In case Wr12-Uc2, the secondary intrusion region can be seen clearly below the primary tube-shape intrusion region [Fig. 2.11(c)]. In case Wr20-Uc2, the combined effect of stronger crossflow and continuous peeling process forms a continuous intrusion region (i.e., no separated primary and secondary intrusions) that is narrow in the spanwise direction but tall in the vertical direction [Fig. 2.11(d)].

### 2.4.3 Dye flux statistics

The exchange of material between the plume and the ambient water as well as the material transport into the intrusion layer can be analyzed by quantifying the streamwise flux of dye based on the LES data. In particular, The time-averaged streamwise flux of dye, $\overline{uC_{dye}}$, can be decomposed as

$$\overline{uC_{dye}} = \overline{u'C'_{dye}} + \overline{u}\overline{C}_{dye} \, , \tag{2.13}$$

where $u' = u - \overline{u}$ is the turbulent fluctuation of the streamwise velocity and $C'_{dye} = C_{dye} - \overline{C}_{dye}$ is the turbulent fluctuation of the dye concentration. In Eq. (2.13), $\overline{u'C'_{dye}}$ represents the turbulent entrainment due to the streamwise velocity fluctuation and $\overline{u}\overline{C}_{dye}$ represents the dye transport by the mean streamwise flow.

Figures 2.12 and 2.13 show the contours of $\overline{u'C'_{dye}}$ and $\overline{u}\overline{C}_{dye}$, respectively, on the $(x,z)$-plane across the plume source for $w_r = 6\,\mathrm{cm/s}$ under different crossflow conditions. Note that the contour range plotted in Fig. 2.13 is four times the range plotted in Fig. 2.12, and in Figures 2.12 to Fig. 2.15, the solid black lines are the iso-lines of $\overline{w} = 1\,\mathrm{cm/s}$ and the dashed black lines are the iso-lines of $\overline{w} = -1\,\mathrm{cm/s}$, which are used to indicate the locations of the rising and falling plumes,

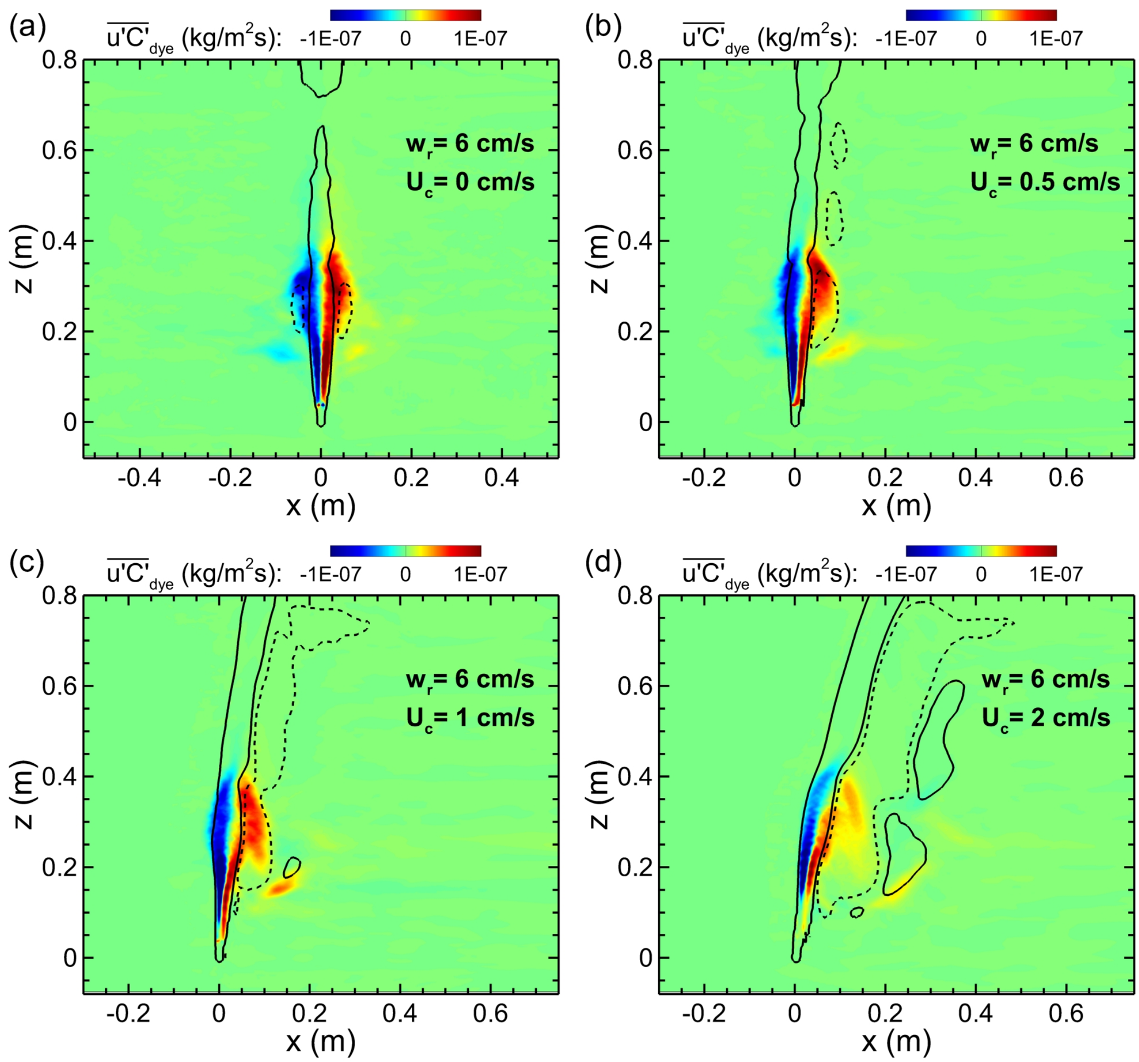


Figure 2.12: Time-averaged streamwise dye entrainment flux $\overline{u'C'_{dye}}$ (i.e., the color contours) on the $(x, z)$-plane across the source for the cases with $w_r = 6\,\mathrm{cm}$: (a) Wr6-Uc0; (b) Wr6-Uc05; (c) Wr6-Uc1; (d) Wr6-Uc2.

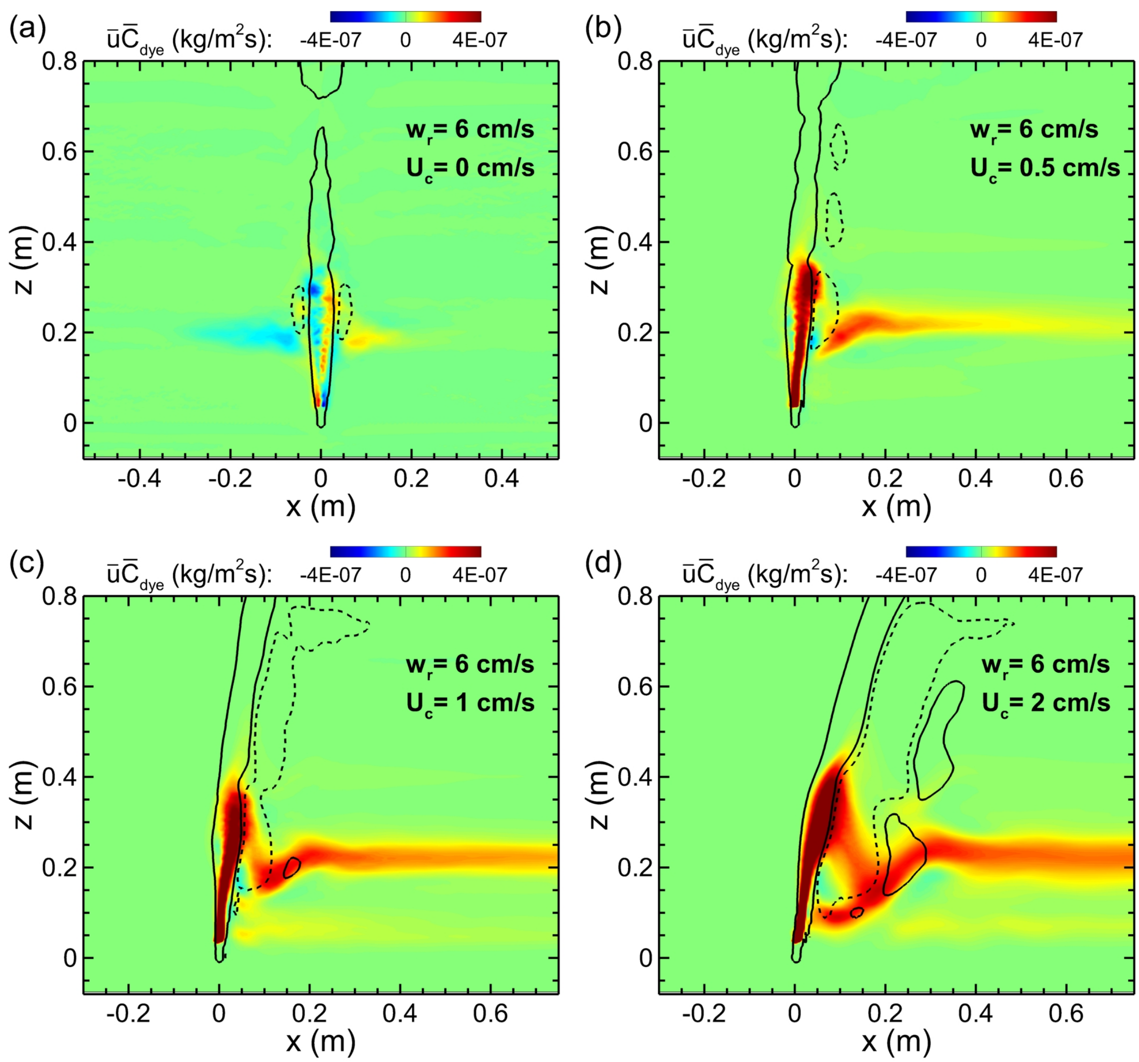


Figure 2.13: Time-averaged streamwise dye flux by mean flow $\overline{u}\overline{C}_{dye}$ (i.e., the color contours) on the $(x, z)$-plane across the source for the cases with $w_r = 6$ cm: (a) Wr6-Uc0; (b) Wr6-Uc05; (c) Wr6-Uc1; (d) Wr6-Uc2.

respectively. For case Wr6-Uc0 (i.e., no crossflow), strong horizontal turbulent fluxes of dye concentration appear within the stem region of the rising plume (i.e., at $z$0.2 m) [Figs. 2.12(a)], which cause the radial expansion of the dye concentration field as the plume rises through the water. At 0.2$z$0.3 m, the rising plume (i.e., the region enclosed by the iso-line of $\overline{w} = 1\,\mathrm{cm/s}$) interacts with the falling plume (indicated by the iso-lines of $\overline{w} = -1\,\mathrm{cm/s}$), resulting in strong turbulent entrainment flux of dye across the interface of the two counter-flowing plume regions [Fig. 2.12(a)]. At 0.3$z$0.4 m, strong horizontal turbulent flux of dye also occurs due to the turbulence in the plume peeling process [Fig. 2.12(a)]. After the dye is detrained from the rising plume, it is carried by the falling plume to the neutral buoyancy level and further transported into the horizontal intrusion layer by the relatively weak radial direction mean flow, as shown by the mean horizontal flux in Fig. 2.13(a).

With the presence of crossflow, the peeling process forms the falling plume on the downstream side of the rising plume, causing the turbulent entrainment process to also bias towards the downstream side [Fig. 2.12(b–d)]. For case Wr6-Uc05 with the weak crossflow of $U_c = 0.5\,\mathrm{cm/s}$, the turbulent flux $\overline{u'C'_{dye}}$ plays a dominant role for transporting the dye from the rising plume into the falling plume through the primary peeling flow as well as across the rising/falling plume interface via turbulent entrainment [Fig. 2.12(b)]. After the dye is carried to the neutral buoyancy level by the falling plume, the streamwise flux $\overline{u}\overline{C}_{dye}$ due to the mean flow becomes dominant and continues to transport the dye into the horizontal intrusion layer at around $z = 0.2\,\mathrm{m}$ [Fig. 2.13(b)]. As the crossflow speed further increases to $U_c = 1\,\mathrm{cm/s}$ (i.e., case Wr6-Uc1), while the turbulent flux $\overline{u'C'_{dye}}$ is still significant in the peeling flow region [Fig. 2.12(c)], the mean flow flux $\overline{u}\overline{C}_{dye}$ also makes a considerable contribution for transporting the dye from the rising plume into the falling plume near the peeling region [Fig. 2.13(c)]. Noticeable mean flux is also observed at a lower elevation to transport the dye into the secondary intrusion layer at around $z = 0.08\,\mathrm{m}$. As the crossflow further increases to $U_c = 2\,\mathrm{cm/s}$ in case Wr6-Uc2, the inclined rising plume generates a more steady peeling flow at around $z = 0.4\,\mathrm{m}$, resulting in weaker turbulent flux $\overline{u'C'_{dye}}$ [Fig. 2.12(d)] and more significant mean flux [Fig. 2.13(d)] from the rising plume into the falling plume near the peeling region. Further downstream from the plume, the dye is transported into both the primary and secondary intrusion layers by the mean streamwise velocity, with more significant mean flux into the primary intrusion layer [Fig. 2.13(d)].

Figures 2.14 and 2.15 show the contours of $\overline{u'C'_{dye}}$ and $\overline{u}\overline{C}_{dye}$, respectively, on the $(x,z)$-plane across the plume source for the four different bubble rise velocities under the same crossflow condition of $U_c = 2\,\mathrm{cm/s}$. Note that similar to Figs. 2.12 and 2.13, the contour range plotted in Fig. 2.14 is four times the range plotted in Fig. 2.15. The analysis result shows that the turbulent and mean dye fluxes for cases Wr3-Uc2 and Wr6-Uc2 are similar in general, exhibiting a strong peeling process near $z = 0.4\,\mathrm{m}$ with considerable turbulent and mean dye fluxes from the rising plume into the falling plume [Figs. 2.14(a,b) and 2.15(a,b)]. For case Wr12-Uc2 with a larger bubble rise velocity of $w_r = 12\,\mathrm{cm/s}$ [Figs. 2.14(c) and 2.15(c)], the rising plume is narrower and more straight, and the main peeling process occurs at a lower elevation of around $z = 0.3\,\mathrm{m}$, with considerable contributions due to both the turbulent and mean dye fluxes from the rising plume into the falling plume. The mean dye flux into the secondary intrusion layer in case Wr12-Uc2 is also larger than those in cases Wr3-Uc2 and Wr6-Uc2. Differently, case Wr20-Uc2 does not exhibit a strong and distinct primary peeling process, as shown by the vertically distributed weak turbulent dye flux from the rising plume into the falling plume within 0.1$z$0.4 m [Fig. 2.14(d)]. On the other hand, the mean dye flux is significant along the downstream side of the rising plume in case Wr20-Uc2 [Fig. 2.15(d)]. The combined effect of the turbulent and mean fluxes of dye results in the vertically extended intrusion region in case Wr20-Uc2 shown in Figs. 2.9(d) and 2.11(d).

Further downstream away from the rising and falling plumes, the dye is transported mainly by the mean streamwise flow. Based on the time-averaged flow field, the mean streamwise flux of the dye concentration can be quantified to help understand the spatial distribution of mean intrusion from the plume into the water in the far field. In particular, the total mean streamwise flux of dye across the $(y,z)$-plane at the streamwise location $x_0$ can be calculated as

$$\Phi_x = \int_{z_{bot}}^{z_{top}} \int_{-L_y/2}^{L_y/2} \overline{C}_{dye}(x_0,y,z)\overline{u}(x_0,y,z)\,\mathrm{d}y\,\mathrm{d}z, \tag{2.14}$$

where the domain dimension parameters $z_{bot}$, $z_{top}$ and $L_y$ are specified in Sec. 2.3. The normalized vertical distribution of the mean streamwise dye flux is defined as

$$\phi_x(z) = \frac{1}{\Phi_x} \int_{-L_y/2}^{L_y/2} \overline{C}_{dye}(x_0,y,z)\overline{u}(x_0,y,z)\,\mathrm{d}y, \tag{2.15}$$

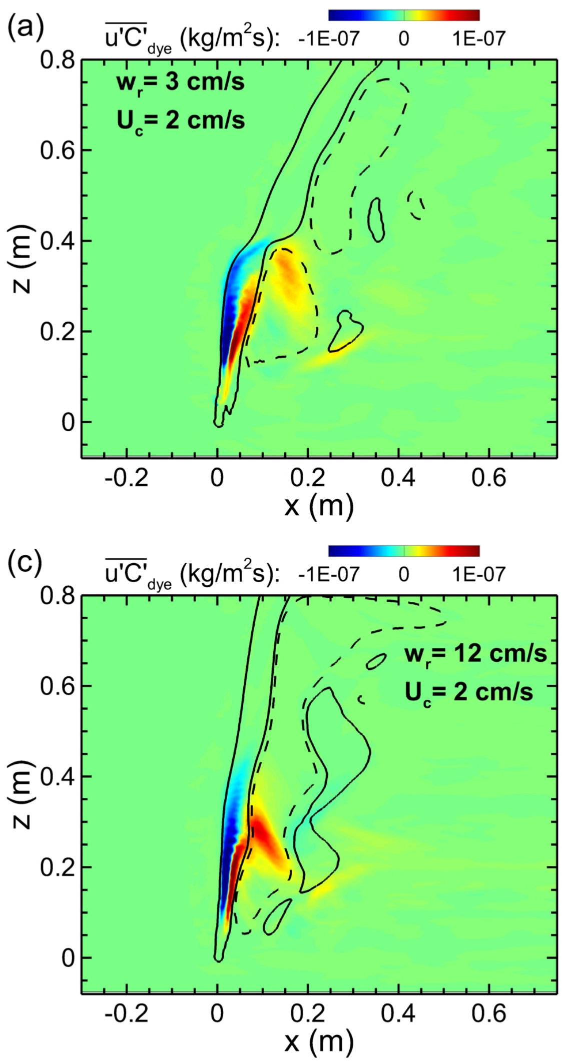


Figure 2.14: Time-averaged streamwise dye entrainment flux $\overline{u'C'_{dye}}$ (i.e., the color contours) on the $(x, z)$-plane across the source for the cases with $U_c = 2\,\text{cm}$: (a) Wr3-Uc2; (b) Wr6-Uc2; (c) Wr12-Uc2; (d) Wr20-Uc2.

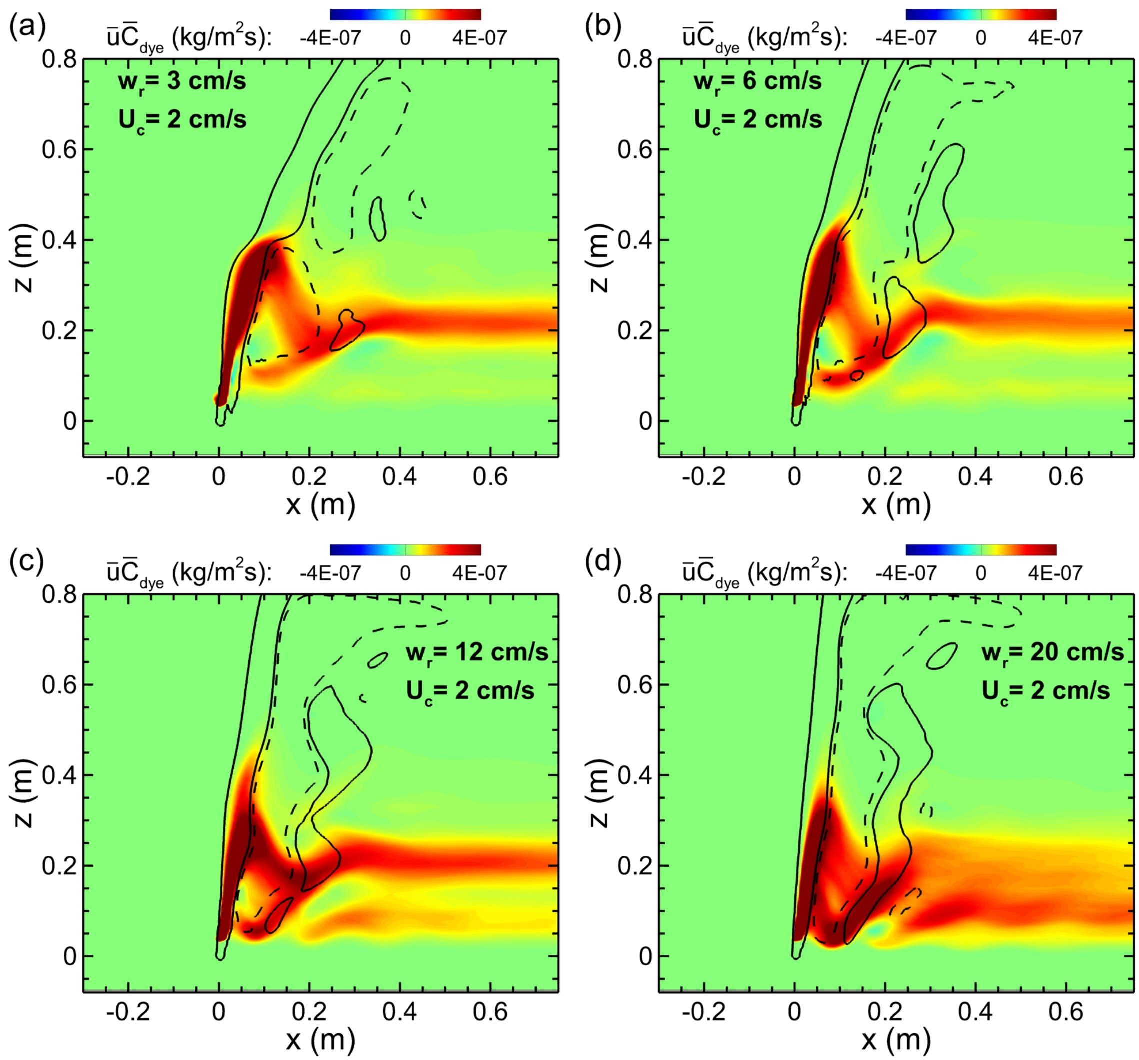


Figure 2.15: Time-averaged streamwise dye flux by mean flow $\overline{u}\overline{C}_{dye}$ (i.e., the color contours) on the $(x, z)$-plane across the source for the cases with $U_c = 2\,\mathrm{cm}$: (a) Wr3-Uc2; (b) Wr6-Uc2; (c) Wr12-Uc2; (d) Wr20-Uc2.

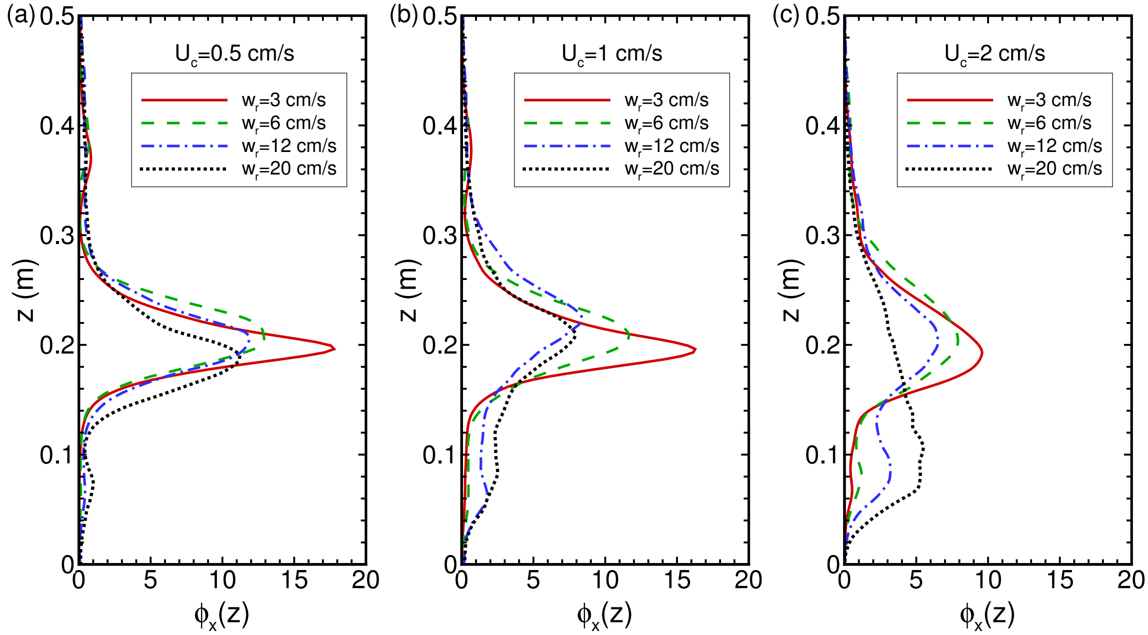


Figure 2.16: Normalized vertical distributions of mean streamwise dye flux $\phi_x(z)$ at $x_0 = 0.5\,\mathrm{m}$: (a) cases with $U_c = 0.5\,\mathrm{m/s}$; (b) cases with $U_c = 1\,\mathrm{m/s}$; (c) cases with $U_c = 2\,\mathrm{m/s}$.

and the normalized spanwise distribution of the mean streamwise dye flux is

$$\psi_x(y) = \frac{1}{\Phi_x} \int_{z_{bot}}^{z_{top}} \overline{C}_{dye}(x_0, y, z)\overline{u}(x_0, y, z)\,\mathrm{d}z. \tag{2.16}$$

For the analysis reported below, the streamwise location for quantifying the mean flux distributions is set to be $x_0 = 0.5\,\mathrm{m}$.

Figures 2.16 and 2.17 show the profiles of $\phi_x(z)$ and $\psi_x(y)$, respectively, for the LES cases with the four different bubble rise velocities and three different crossflow speeds. Several general trends observed from the instantaneous and time-averaged plume fields can be seen clearly here from these mean dye flux profiles. On the one hand, for a fixed $U_c$, increasing $w_r$ causes the primary intrusion region to spread more in the vertical direction and less in the spanwise direction. On the other hand, for a fixed $w_r$, increasing the crossflow speed $U_c$ results in the intrusion region being spread more vertically and less spanwise. Large $w_r$ (e.g., 12 and 20 cm/s) also results in noticeable secondary intrusion below $z = 0.1\,\mathrm{m}$, which becomes more significant when combined with the effect of fast crossflows (e.g., $U_c = 1$ and $2\,\mathrm{cm/s}$). For case Wr20-Uc2, the profile $\phi_x$ [i.e., the dotted

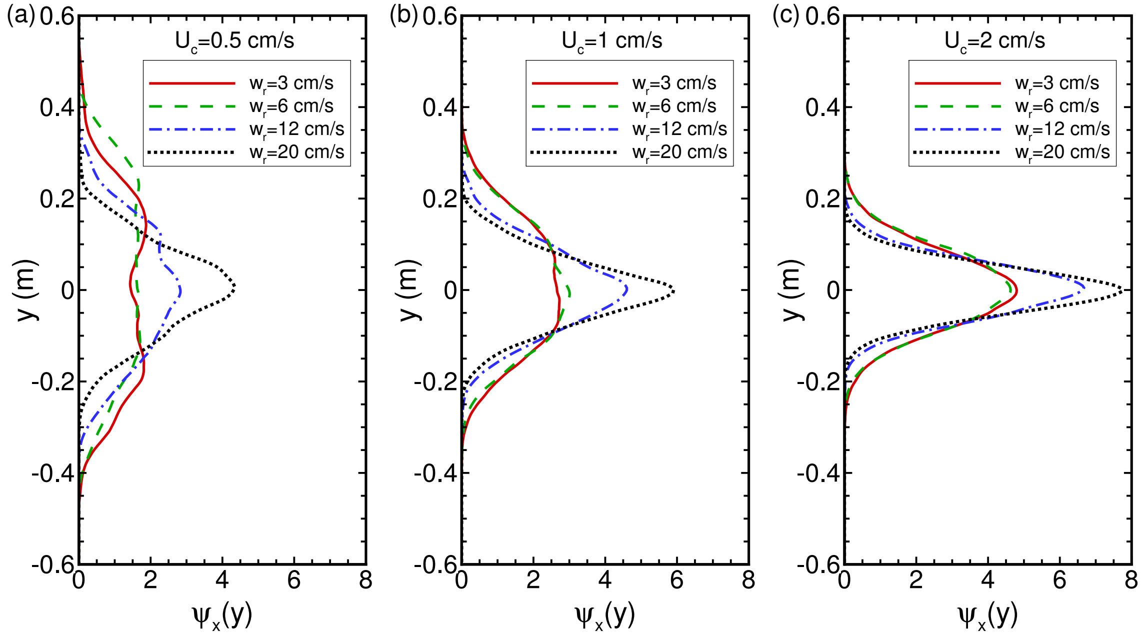


Figure 2.17: Normalized spanwise distributions of mean streamwise dye flux $\psi_x(y)$ at $x_0 = 0.5\,\mathrm{m}$: (a) cases with $U_c = 0.5\,\mathrm{m/s}$; (b) cases with $U_c = 1\,\mathrm{m/s}$; (c) cases with $U_c = 2\,\mathrm{m/s}$.

line in Fig. 2.16(c)] exhibits a wide vertical distribution of the mean streamwise dye flux within $0 < z < 0.4\,\mathrm{m}$, with the peak near $z = 0.1\,\mathrm{m}$ that is much lower than the primary peak elevation of $\phi_x$ in other cases (i.e., near $z = 0.2\,\mathrm{m}$).

## 2.5 Conclusions

In this chapter, LES modeling is applied to investigate the effects of crossflow on the characteristics of laboratory-scale bubble-driven plumes in a stably stratified water environment. A series of LES runs have been performed to cover a range of plume and crossflow conditions, including four different bubble rise velocities (i.e., $w_r = 3$, 6, 12 and $20\,\mathrm{cm/s}$) and three different crossflow speeds (i.e., $U_c = 0.5$, 1 and $2\,\mathrm{cm/s}$). Comparisons of the instantaneous and time-averaged plumes for the different simulation cases show that the crossflow can significant affect the plume characteristics and the subsequent dye transport from the plume into the water environment.

In the reference case without crossflow, the bubbles drive the plume to rise vertically upwards and interact with the water stratification, resulting in an annular plume of detrained high-density water to fall along the outside of the rising plume. The overall plume structure and dynamic processes are axisymmetric without crossflow. The presence of crossflow breaks the axisymmetry of the plume structure, and causes the falling plume to form on the downstream side of the rising plume. This asymmetry results in less contact area between the rising and falling plumes, causing the falling plume to be more significant than that in the reference case without crossflow.

The bubble rise velocity (which varies according to the bubble diameter) determines how strong the bubble column in the rising plume can resist the forcing from the crossflow as well as the turbulence in and around the plume. A plume with larger bubble rise velocity exhibits less tilting by the crossflow and less horizontal expansion by turbulence than a plume with smaller bubble rise velocity. For all the plumes with the four different bubble rise velocities, the presence of crossflow induces considerable effect on the transport of dye from the rising plume into the falling plume, and subsequently into the surrounding water environment. In particular, the presence of 2 cm/s crossflow enhances the mean flow from the rising plume into the falling plume at the peel height, significantly enhancing the mean flux of dye from the plume into the surrounding water environment. The crossflow also causes considerable dye transport from the stem region of the rising plume directly into the surrounding water to form a secondary dye intrusion layer below the primary intrusion layer generated by the main peeling process. The enhancement of dye transport becomes more significant in case Wr20-Uc2 when the large bubble rise velocity results in a narrow bubble column and an unstable peeling process along the entire downstream side of the rising plume, which causes the dye to flow continuously from the rising plume into the surrounding water to form a vertically extended intrusion region with less spanwise expansion.

It should be noted that this study considers the laboratory-scale condition with relatively simple water stratification and crossflow conditions. Therefore, caution should be taken when applying the conclusion from this study to the case of a field-scale plume. Further investigations are desired for understanding the crossflow effect on a large-scale bubble-driven plume in the deep-water environment, with additional effects to be taken into consideration (e.g., the depth-dependent variation of the crossflow velocity, the nonlinear stratification of water density, the effects of gas bubble expansion and dissolution when rising through the large water depth, etc.). Nevertheless, the simulation and statistical analysis results reported in this study still provide some useful insights for understanding some of the key effects of the crossflow on the plume dynamics and material transport.

# Chapter 3

# Effect of oil plumes on upper-ocean radiative transfer

## 3.1 Introduction

Crude oil, as indicated by its dark color, is a strong absorber of light when spilled into the upper ocean [104]. In the aftermath of a large-scale offshore oil spill, such as the 2010 *Deepwater Horizon* accident, spilled crude oil can spread over a large horizontal area in the upper ocean and last for long time before being restored or biodegraded, inducing significant impact on the ocean ecosystem [8, 20, 56]. Surface oil slicks and suspended oil droplets in the euphotic zone can block light from penetrating into subsurface region where phytoplankton live [65], threatening the ocean ecosystem from the origin of its food chain by significantly reducing the rate of photosynthesis. On the other hand, ultraviolet light can alter (degrade) oil in the process of photo-degradation, which can produce some byproducts that can be more toxic than the source oil [9, 64, 116, 117]. Improved knowledge on the light penetration in oil-contaminated seawater can help obtain a more accurate estimation of the photo-degradation rate than using the normal light penetration profiles obtained based on the natural ocean condition. Recent report by [76] based on the field measurement data obtained during the *Deepwater Horizon* oil spill incident has confirmed the noticeable effect of spilled crude oil on the vertical variation of incident ultraviolet radiation and extinction coefficients in the northern Gulf of Mexico. Thus understanding the oil-induced effects on the oceanic radiative transfer is crucial for accurately modeling the ocean ecosystem evolution in the wake of a large offshore oil spill.

Suspended crude oil droplets affect the local seawater's inherent optical properties (IOPs) (i.e., the light absorption and scattering coefficients), which depend on the local droplet number density, droplet size, and oil type [68, 104, 105, 122]. The dispersion of oil droplets and other buoyant particles in the euphotic zone is actively driven by various physical processes induced by atmospheric forcing, e.g., shear-induced turbulence, sea-surface waves, Langmuir circulations, Ekman transport, thermal convection, etc. [34, 42, 69, 107, 149]. These effects continuously mix the very upper tens of meters of the ocean to form the ocean mixed layer (OML), which can also cause considerable dilution of the oil droplet plume by horizontal and vertical mixing [see e.g., 91, 169]. On the other hand, the buoyancy of the oil droplets acts as a resistant force to the mixing effects generated by the oceanic flows and can cause inhibition of oil plume dilution under certain conditions [168].

In recent years, the continuous growth of computer power has made high-fidelity computational models feasible for tackling the complex ocean processes. Particularly, large-eddy simulation (LES) based on the Craik–Leibovich (CL) equation [78] has proven to be a useful tool for providing insights of fine-scale oceanic flows and transport phenomena [52, 54, 71, 81, 82, 92, 103, 127]. Using the LES method, several recent studies have been able to shed light on the detailed three-dimensional dispersion processes of oil plumes in the OML under various conditions ([29, 30, 168, 169]). In particular, under wind and wave dominant conditions, plumes of oil droplets are found to be strongly affected by Langmuir circulations and shear-induced turbulence, and exhibit various types of surface patterns with different dilution levels, ranging from highly intermittent surface streaks for large oil droplets to smoothly diffused plumes for small oil droplets [168, 169]. Under convection dominant conditions, buoyant materials show strong preferential concentration in surface convergence regions generated by convective cells; in addition, highly buoyant particles (e.g., large oil droplets) can also be affected by a secondary effect induced by some persistent surface vortices in the turbulent flow field that collect and cluster these particles into vorticity-dominant surface regions [30].

Due to the considerable spatial variation of oil droplet concentration caused by these aforementioned flow-induced transport phenomena in the OML, the IOPs of the oil-contaminated seawater can also exhibit complex spatial variations that can strongly affect the variation of light intensity in the euphotic zone, which is a crucial information for modeling the light variation due to oil spill but has not been well understood up to date. Simple one-dimensional downward irriadiance models [e.g., 77, 162, 163] require the information about the diffuse attenuation coefficient, which is an apparent optical property of the water body and is not available from the literature for the ocean contaminated by oil plumes with complex spatial variations. This directly motivates this study. With the detailed three-dimensional flow field information in hand, the oceanic light field can be efficiently modeled by solving the radiative transfer equation using the Monte Carlo simulation (MCS) method ([50, 66, 67]). Simulations based on the MCS method can capture the three-dimensional radiative transfer in dynamic ocean covered by wind-generated sea-surface waves [167, 180]. The combination of LES and MCS methods has been demonstrated to provide valuable insights for understanding the complex effects of ocean turbulence on its optical properties [165]. The effects of particles on the radiative transfer can also be included in the MCS method using the Mie theory [e.g., 114, 156].

In this chapter, we utilize these recent advancements in computational models to establish a numerical modeling framework for simulating the radiative transfer in the ocean euphotic zone contaminated by plumes of suspended crude oil droplets. We perform two sets of numerical experiments corresponding to two representative OML flow conditions: (1) wind/wave dominant condition with shear-generated turbulence and wave-induced Langmuir circulations, and (2) convection dominant condition with thermal convective cells. Because the oil droplet size plays a crucial role in determining both the dynamic response of the oil plume to the OML flows [168, 169] and the light absorption/scattering [97, 104, 105], for each OML condition we consider three different oil droplet diameters. All together, these simulation cases allow us to cover a variety of oil plume patterns with different levels of horizontal and vertical dilutions, from which the effect of oil contamination on oceanic radiative transfer is studied. Figure 3.1 illustrates the problem configuration and some representative results for the effect of flow and oil field on the radiative transfer.

This chapter is organized as follows. Details of the computational models used in this work are reported in Section 3.2. Section 3.3 shows the simulation and statistical analysis results. Finally, conclusions are given in Section 3.4.

## 3.2 Numerical Models

### 3.2.1 Highlight of modeling strategy

Radiative transfer in natural seawater is affected by the sea-surface geometry and seawater properties underneath the surface (e.g., temperature, salinity, suspended particulate matter, colored dissolved organic matter, etc.) [65, 98]. In the case of an offshore oil spill incident, the presence of suspended oil droplets further complicates the radiative transfer process and causes considerable variation to the subsurface light field.

Note that the essential physical processes that affect the light field (i.e., wave oscillation, turbulence mixing and transport, and photon propagation) occur at very different time scales. For example, the ocean waves oscillate at the periods of $O(0.1) \sim O(10)$ seconds depending on the wavelength. The surface oil plumes evolve at the time scale of minutes for small-scale features and hours for large-scale patterns. A photon's lifetime when propagating in the upper ocean is on the order of $O(0.001) \sim O(0.1)$ microseconds depending on the penetration depth. The considerable time-scale separation and significant differences in the details of the physical processes impose great challenges. In this study we adopted a suite of numerical models that are designed for capturing different aspects of this complex physical problem, and combined their strengths to tackle the problem. The overall modeling strategy is highlighted below:

(i) The instantaneous sea-surface wave field is simulated using a high-order spectral (HOS) method [38], which provides the geometry of the air–water interface for modeling the light refraction at the sea surface based on Snell's law and Fresnel's equations [167, 180]. (See details in Section 3.2.2 and A.1.)

(ii) Underneath the sea surface, the OML flow field is simulated using a LES model [168], which models the oceanic flow structures (e.g., shear turbulence, Langmuir circulations, convective cells, etc.) generated by sea-surface wind shear stress, surface heat flux, and wave-induced Stokes drift. This LES model is based on the widely used Craik–Leibovich equation, in which the accumulated effect of sea-surface waves on the turbulence and material transport is modeled based on the wave-induced Stokes drift current [78]. (See details in Section 2.2.)

(iii) In the ocean column, the transport of crude oil droplets is modeled using an Eulerian–Eulerian LES method [168, 169], in which the evolution of the concentration field of the oil droplets is simulated by a finite-volume LES model and is coupled with the LES model for oceanic flow described in (ii). (See details in Section 2.2.)

(iv) Based on the instantaneous sea-surface wave geometry obtained from (i) and the instantaneous oil droplet concentration obtained from (iii), the seawater IOPs are modeled and the radiative transfer in the euphotic zone is simulated by a MCS model. This model can capture the effects of suspended oil droplets on the absorption and scattering of photons as they propagate through the mixture of seawater and oil droplets. (See details in Section 3.2.4 and A.2.)

Each of these above models have proven track record for modeling their corresponding physical processes in various applications, and their details are presented in the next several subsections. Figure 3.1 shows a representative example of the simulation results obtained by this set of numerical models, where the oil plume is visualized using the iso-surfaces (in brown color) of oil droplet concentration. Contours of the downward irradiance are shown on the vertical plane cutting through the oil plume as well as on the bottom plane of the plotted simulation domain..

Because the physical processes involved in the current problem are complicated and occur over a wide range of time and length scales, it is impractical to perform the simulations with each of the above models fully coupled in a two-way dynamic coupling manner. Instead, in this study the hydrodynamic models (i)–(iii) are used as precursor simulators to provide the required flow field data for the MCS model (iv) to simulate the radiative transfer in the oil-contaminated seawater. Among the three hydrodynamic models (i)–(iii), the two LES models (ii) and (iii) are dynamically coupled to simulate the oil plume dispersion in the upper ocean in a wave-averaged but turbulence-resolved manner. As explained below in Section 2.2, the coupled LES models account for the accumulated effect of sea-surface waves on the oil transport, but do not model the instantaneous waves explicitly. The HOS model (i) uses identical wave spectra as in the LES model to provide the corresponding wave surface geometry. The combination of the surface waves and the subsurface oil concentration field provides a synthetic upper-ocean field for modeling the radiative transfer process. Details of each models are discussed below in Sections 3.2.2–3.2.4 as well as in A.1 and A.2.

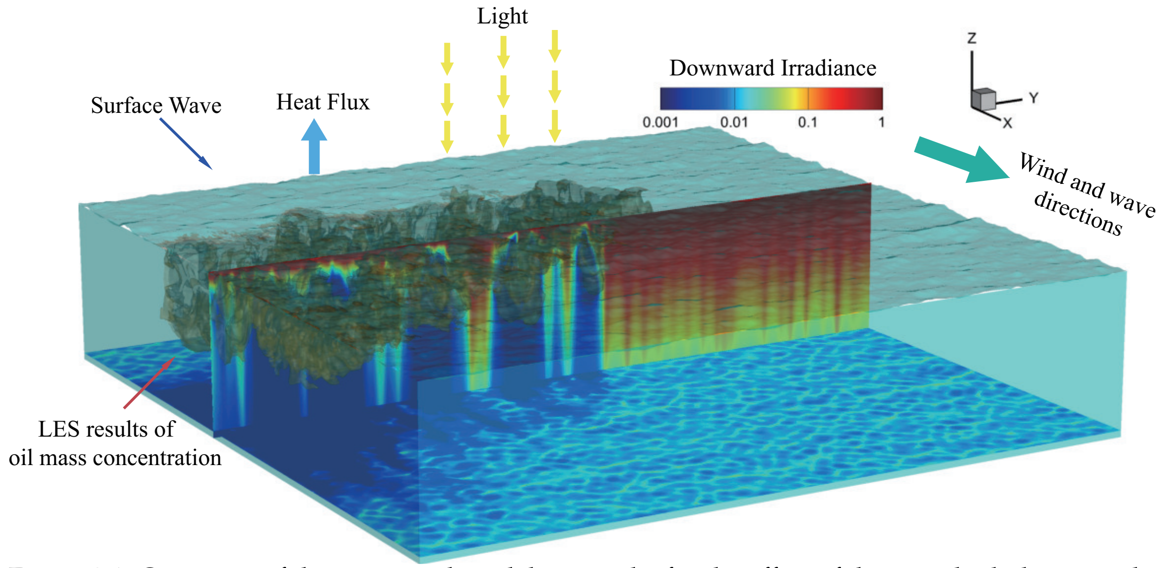


Figure 3.1: Overview of the numerical modeling results for the effect of dispersed oil plume on the upper-ocean radiative transfer.

### 3.2.2 High-order spectral simulation of sea-surface waves

When light strikes on the sea surface, it first interacts with the air–water interface curved due to waves. In this chapter, we adopt the widely used high-order spectral method to simulate instantaneous sea-surface waves. The HOS method models the wave motions based on the potential flow theory, in which the wave orbital velocity satisfies $\mathbf{u} = \nabla\Phi$, where $\Phi$ is the velocity potential. In the water body, the wave-induced flow motions satisfy the continuity equation $\nabla^2\Phi = 0$. On the sea surface, the wave satisfies both the kinematic and dynamic free-surface boundary conditions, which can be defined precisely at the instantaneous wave surface $z = \eta(x, y, t)$ using Zakharov's equations [181],

$$\frac{\partial\eta}{\partial t} + \widehat{\nabla}\eta \cdot \widehat{\nabla}\Phi^s + \left(1 + |\widehat{\nabla}\eta|^2\right) \frac{\partial}{\partial z}\Phi(x, y, \eta, t) = 0 \quad \text{at } z = \eta \tag{3.1}$$

and

$$\frac{\partial\Phi^s}{\partial t} + g\eta + \frac{|\widehat{\nabla}\Phi^s|^2}{2} - \frac{1}{2}\left(1 + |\widehat{\nabla}\eta|^2\right)\left[\frac{\partial}{\partial z}\Phi(x, y, \eta, t)\right]^2 = 0 \quad \text{at } z = \eta. \tag{3.2}$$

Here, $\eta$ is the instantaneous wave surface elevation, $\Phi^s = \Phi|_{z=\eta}$ is the surface potential, and $\widehat{\nabla} = (\partial/\partial x, \partial/\partial y)$ is the horizontal gradient.

For fast numerical simulation, the continuity equation and boundary conditions (3.1) and (3.2) are rewritten into series of discretized modes using perturbation method and eigenfunction expansion following [38] (also see [93]), and are solved numerically using Fourier series based pseudo-spectral method. Additional details of the current HOS model are given in A.1. The HOS method has been successfully applied to a variety of different ocean surface wave problems in recent years (see e.g., [2, 51, 150, 171–173, 176]). Figure 3.2(a) shows a sample result of sea-surface wave field simulated using the current HOS model.

### 3.2.3 Large-eddy simulation of turbulent flows and oil plume transport in ocean mixed layer

To efficiently simulate the Langmuir circulations and shear/convection driven turbulent flows in the ocean mixed layer (OML) and the corresponding oil plume transport, we employ a LES model that consists of a pseudo-spectral/finite-difference flow solver based on the CL equation and a finite-volume oil transport solver. This LES model has been successfully applied to simulate oil and buoyant particle dispersion in OML in several recent studies ([25, 29, 30, 168, 169]). In this model, the OML flows are governed by the filtered continuity equation and CL equation,

$$\nabla \cdot \widetilde{\mathbf{u}} = 0 \tag{3.3}$$

and

$$\frac{\mathrm{D}\widetilde{\mathbf{u}}}{\mathrm{D}t} = -\frac{1}{\rho_0}\nabla\widetilde{p} - f_c\mathbf{e}_3 \times (\widetilde{\mathbf{u}} + \mathbf{u}_s) + \mathbf{u}_s \times \widetilde{\boldsymbol{\omega}} - \nabla\cdot\boldsymbol{\tau} + \left(1 - \frac{\widetilde{\rho}}{\rho_0}\right) g\mathbf{e}_3 \,. \tag{3.4}$$

Here, tilde denotes a resolved variable resolved on the LES grid, $\mathbf{u}$ is the fluid velocity vector, $\mathrm{D}/\mathrm{D}t = (\partial/\partial t + \widetilde{\mathbf{u}}\cdot\nabla)$ is the material derivative, $\rho_0$ is the reference seawater density, $\widetilde{\rho}$ is the resolved local seawater density, $p$ is the modified pressure, $g$ is the gravitational acceleration, $\mathbf{e}_3$ is the unit vector in the vertical direction, $f_c$ is the Coriolis frequency, $\mathbf{u}_s$ is the wave-induced Stokes drift velocity, $\boldsymbol{\omega} = \nabla \times \mathbf{u}$ is the vorticity, and $\boldsymbol{\tau} = (\widetilde{\mathbf{u}\mathbf{u}} - \widetilde{\mathbf{u}}\widetilde{\mathbf{u}})$ is the subgrid-scale (SGS) stress tensor. The first four terms on the right-hand side of Eq. (3.4) are pressure gradient force, Coriolis force, the vortex force due to Stokes drift representing the phase-averaged effects of surface gravity waves

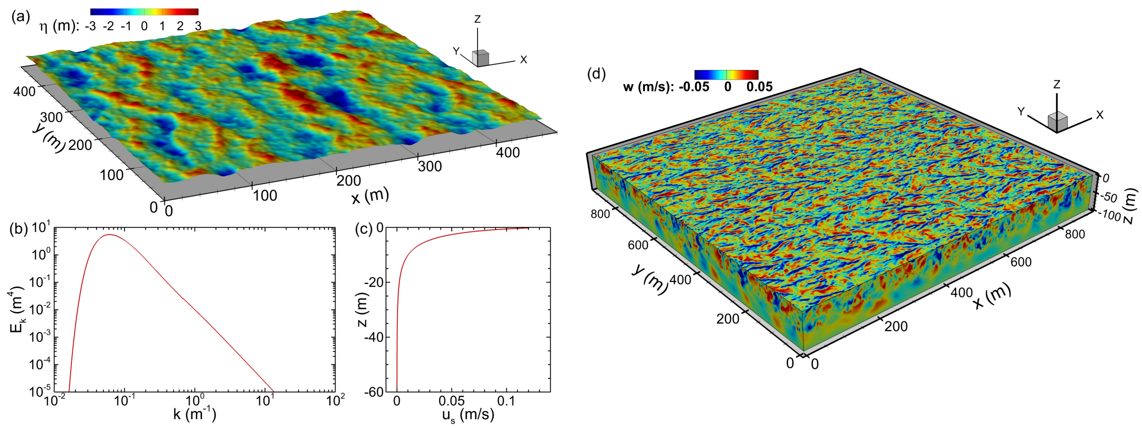
Figure 3.2: Sample results for a broadband wave field under 10 m/s wind.

on the mean flow and turbulence, and the SGS term representing the effect of unresolved fluid motions below LES grid scale. Details of the Stokes drift current $\mathbf{u}_s(z)$ are given further below.

The last term in Eq. (3.4) is the buoyancy force due to density variation, which are formed based on the Boussinesq approximation [e.g., 92, 108]. The buoyancy force induced by the oil droplets is neglected due to the low released rate considered in this study and the low local oil concentration after turbulence-induced dilution. Following previous LES studies [e.g., 70, 92, 115, 168, 169], we assume the seawater density satisfies a linear equation of state, i.e., $\widetilde{\rho} = \rho_0 \left[1 - \alpha_t(\widetilde{\Theta} - \Theta_0)\right]$, where $\alpha_t = 2 \times 10^{-4}\,\mathrm{K}^{-1}$ is the thermal expansion coefficient, $\widetilde{\Theta}$ is the resolved potential temperature, and $\Theta_0$ is the reference temperature corresponding to $\rho_0$. The variation of the temperature field is computed by solving a filtered convection-diffusion equation

$$\frac{\mathrm{D}\widetilde{\Theta}}{\mathrm{D}t} = -\mathbf{u}_s \cdot \nabla\widetilde{\Theta} - \nabla \cdot \boldsymbol{\pi}_t \, , \tag{3.5}$$

where $\boldsymbol{\pi}_t = (\widetilde{\mathbf{u}\Theta} - \widetilde{\mathbf{u}}\widetilde{\Theta})$ is the SGS heat flux. The transport of oil plumes in OML flows is simulated using an Eulerian approach. Oil droplets of the same diameter $d$ are considered as one species, and their instantaneous distribution is represented by a continuous Eulerian mass concentration field $C(\mathbf{x}, t)$. The evolution of $C$ is governed by the filtered transport equation

$$\frac{\partial \widetilde{C}}{\partial t} + \nabla \cdot \left(\widetilde{\mathbf{v}}\widetilde{C}\right) = -\nabla \cdot \boldsymbol{\pi}_c + Q_s \, , \tag{3.6}$$

where $\boldsymbol{\pi}_c = (\widetilde{\mathbf{u}C} - \widetilde{\mathbf{u}}\widetilde{C})$ is the SGS oil concentration flux, $Q_s$ is a source term for subsurface release of the oil droplets, and $\widetilde{\mathbf{v}}$ is the resolved Lagrangian transport velocity of the oil droplets, which is modeled as [25, 45, 168, 169]

$$\widetilde{\mathbf{v}} = \widetilde{\mathbf{u}} + \mathbf{u}_s + w_r \mathbf{e}_3 + (R-1) T_d \left( \frac{\mathrm{D}\widetilde{\mathbf{u}}}{\mathrm{D}t} + \nabla \cdot \boldsymbol{\tau} \right) + \mathcal{O}(T_d^{3/2}) \ . \tag{3.7}$$

Here, $w_r$ is the droplet rise velocity (relative to the surrounding fluid) due to the balance of buoyancy, gravity and Stokes drag, which is modeled as [10, 170]

$$w_r = \begin{cases} w_{r,S} & \mathrm{Re}_d < 0.2, \\ w_{r,S}\left(1 + 0.15\mathrm{Re}_d^{0.687}\right)^{-1}, & 0.2 < \mathrm{Re}_d < 750, \end{cases} \tag{3.8}$$

where $w_{r,S} = (\rho_0 - \rho_d) g d^2 / (18\mu)$ is the droplet rise velocity given by Stokes' law, $\rho_d$ is the oil density, $\mathrm{Re}_d = \rho_0 w_r d / \mu$ is the particle Reynolds number, and $\mu$ is the dynamic viscosity of the seawater. The first three terms on the right-hand side of Eq. (3.7) represent the dominant effects acting on buoyant particles in OML flows. The fourth term on the right-hand side of Eq. (3.7) represents the additional effects due to added mass and SGS fluid stress force, where $R = 3\rho_0 / (2\rho_d + \rho_0)$ is the density ratio parameter and $T_d = w_r / [(R-1)g]$ is the droplet response time scale [169, 170].

In order to solve Eqs.(3.4), (3.5) and (3.6), proper turbulence closures are required for the SGS terms $\boldsymbol{\tau}$, $\boldsymbol{\pi}_t$ and $\boldsymbol{\pi}_c$. In the current model, the SGS stress tensor $\boldsymbol{\tau}$ is parameterized using the Lilly-Smagorinsky eddy-viscosity model [86, 128], i.e., $\boldsymbol{\tau} = -2\nu_\tau \widetilde{\mathbf{S}} = -2(c_s\Delta)^2 |\widetilde{\mathbf{S}}| \widetilde{\mathbf{S}}$, where $\widetilde{\mathbf{S}} = [\nabla\widetilde{\mathbf{u}} + (\nabla\widetilde{\mathbf{u}})^T]/2$ is the resolved strain rate tensor, $\nu_\tau$ is the SGS eddy viscosity, $\Delta$ is the LES grid (filter) scale, and $c_s$ is the Smagorinsky coefficient. The instantaneous and local value of $c_s$ is determined dynamically during the simulation using the Lagrangian-averaging scale-dependent dynamics (LASD) model [14]. With the SGS eddy viscosity modeled as $\nu_\tau = (c_s\Delta)^2|\widetilde{\mathbf{S}}|$, the SGS heat flux $\boldsymbol{\pi}_t$ and oil mass flux $\boldsymbol{\pi}_c$ are then parameterized as $\boldsymbol{\pi}_t = (\nu_\tau/\mathrm{Pr}_\tau)\nabla\widetilde{\Theta}$ and $\boldsymbol{\pi}_c = (\nu_\tau/\mathrm{Sc}_\tau)\nabla\widetilde{C}$ based on constant turbulent Prandtl number $\mathrm{Pr}_\tau = 0.4$ and Schmidt number $\mathrm{Sc}_\tau = 0.4$ [6, 24, 72, 88, 99, 147, 168, 169]. Note that for the simplification of the model, the temperature changes of the seawater and oil droplets due to light absorption are not considered in this study. The oil droplets and the surrounding seawater are assumed to be in thermal equilibrium state, so that the heat exchange between them is also omitted Eq. (3.5).

In this study, we consider the typical open-sea condition such that the sea surface is covered by a broadband wind-generated surface wave field with a directional spectrum $S(k, \alpha)$, where $k = 2\pi/\lambda$ is the wavenumber, $\lambda$ is the wavelength, $\alpha$ is the inclination angle between the wave propagation direction and the mean wind direction. Note that because the CL equation (3.4) models the accumulated effect of surface waves on the shear-driven turbulence in a wave phase-averaged context, the instantaneous sea-surface motions are not included in the simulation. Consistent with the CL modeling framework, the top boundary of the LES domain is modeled as a rigid surface with an imposed mean shear stress in the downwind direction (i.e., the $x$-direction in this chapter), and the fluctuating components of the horizontal velocity components satisfy the free-slip condition at this top boundary. The averaged wave effect is taken into account via the Stokes drift current. Following [90] [also see e.g., 54, 82, 158], the leading-order approximation of the corresponding Stokes drift of such broadband sea-surface wave field can be calculated as

$$\mathbf{u}_s(z) = 2\sqrt{g}\int_0^\infty \int_{-\pi}^{\pi} (\cos\alpha\ \mathbf{e}_1 + \sin\alpha\ \mathbf{e}_2)\, k^{2.5} S(k,\alpha) \exp\left(2kz\right)\ \mathrm{d}\alpha\, \mathrm{d}k, \tag{3.9}$$

where $\mathbf{e}_1$ and $\mathbf{e}_2$ are the unit vectors in the $x$ and $y$ directions, respectively. In the simulations, the wave spectrum $S(k, \alpha)$ is prescribed based on the widely used empirical spectrum obtained by [40] based on field measurement data, and the Stokes drift $\mathbf{u}_s$ calculated by Eq. (3.9) is used in the LES model equations (3.4), (3.5) and (3.7) to simulate the OML flows. Figure 3.2 shows some sample OML flow results obtained by this LES model, where the color contours in (a) indicate the instantaneous wave elevation on the sea surface. Here, in this figure, (a) instantaneous surface waves obtained by the HOS model; (b) empirical wave spectrum from [40]; (c) Stokes drift current profile calculated based on the integral Eq. (3.9); (d) sample result of Langmuir circulations obtained using the LES model based on the Stokes drift in (c). The contours in (d) indicate the instantaneous vertical velocity, and the horizontal plane shown in the figure is chosen at the depth of 5 m beneath the mean sea surface level..

### 3.2.4 Monte Carlo simulation for radiative transfer

The light transport in the ocean euphotic zone is governed by the radiative transfer equation (RTE) [98, 166], which can be simulated efficiently by the Monte Carlo simulation method ([66,

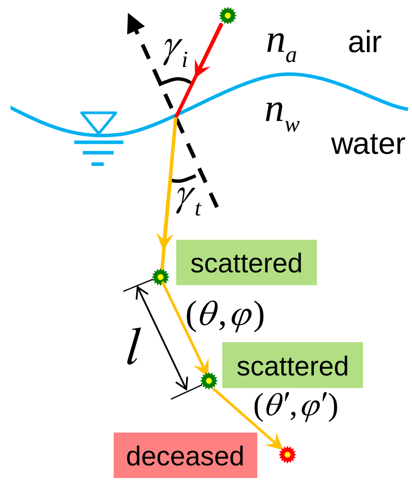


Figure 3.3: Sketch of Monte Carlo simulation for radiative transfer.

67]). As illustrated in Fig. 3.3, MCS method models the scattering and absorption events of photons as they travel in the seawater (i.e.,, a physical representation for the Neumann series of the RTE), which are controlled by the absorption coefficient $a$, scattering coefficient $b$, beam attenuation coefficient $c = a + b$, and scattering phase function $B$. By tracing and calculating the summation of the scatterings and absorptions of many photons, the oceanic light field can be modeled. MCS method has been widely used for studying oceanic radiative transfer (see e.g.,[50, 66, 67, 165–167]).

A general guidance of the MCS method can be found in [77]. Additional details of the current MCS model are given in A.2. Details on modeling $a$, $b$ and $B$ for oil-contaminated seawater are also given in A.2. For simplification, in the current MCS model a “black sky" approximation is made such that the light absorption and scattering caused by the atmosphere are neglected. Consequently, a photon packet can be initialized right above the sea surface. Here, we summarize the key procedure of the MCS method used in this study as illustrated in Fig. 3.3:

(1) A photon packet with initial energy $E_i$ is launched at a random location in the air right above the ocean surface, and travel towards the surface with an incident angle $\gamma_i$.

(2) The photon packet passes through the air–water interface with a transmitted angle $\gamma_t$ and energy $E_t$ based on the Fresnel equations and the refraction indices of air ($n_a$) and water ($n_w$).

(3) When a photon packet travels through the oil-contaminated seawater, it experience a medium with spatial variation of IOPs. To determine the optical pathlength $l$ of the photon packet in this

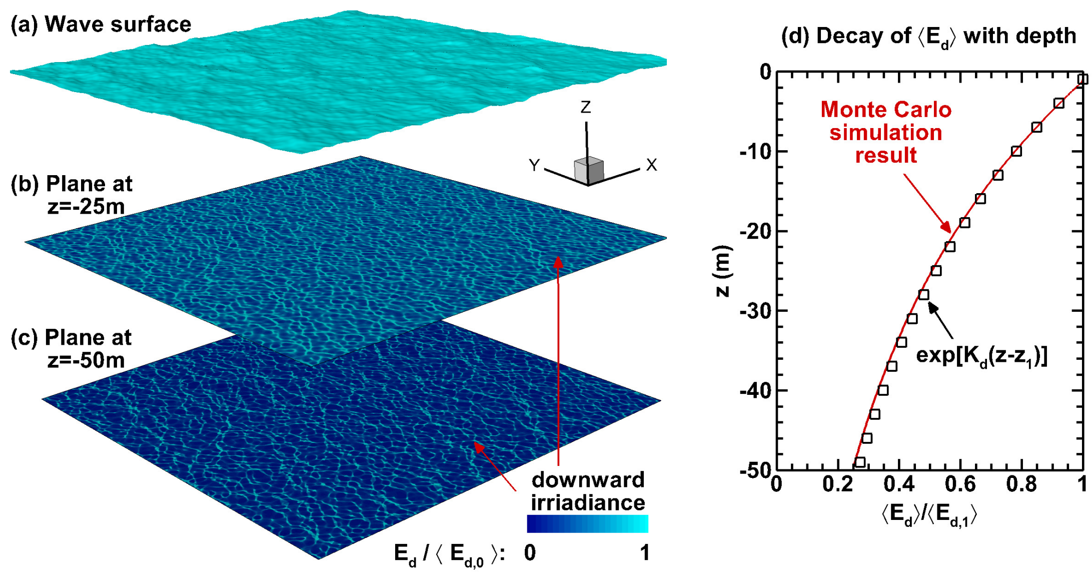


Figure 3.4: Sample result for MCS of 500 nm wavelength light transfer in clean seawater.

highly nonhomogeneous medium, the multi-stepped approach used by [155] is adopted in the current MCS. In particular, the total pathlength is given by $l = \sum l_i$ with the sub-step pathlength $l_i$ being determined by the equation $\sum l_i c_i = -\ln q_1$, where $c_i$ is the local LES cell-averaged beam attenuation coefficient for the $i$-th sub-step and $q_1$ is a random number within $[0, 1]$. In the simulation, the photon packet travels over the optical pathlength $l$ with spatially varying $c$ along its current travel direction described by $(\theta, \varphi)$, where $\theta$ and $\varphi$ are the polar angle and azimuthal angle of the path, respectively.

(4) After traveling over $l$, a random number $q_2 \in [0, 1]$ is generated and compared with the single-scattering albedo $\omega_0 = b/c$. If $q_2 \leq \omega_0$, the photon packet changes the traveling direction due to scattering, and a new set of angles $(\theta', \varphi')$ are determined based on the scattering phase function $B$, and steps (3) and (4) are repeated; otherwise, the photon packet is deceased due to absorption, and a new photon packet is initialized and traced in the simulation by repeating steps (1)–(4).

Figure 3.4 shows a sample result for the radiative transfer of 500 nm wavelength light in clean seawater underneath a surface wave field obtained from the current MCS model. Here, The left panel shows the downward irradiance $E_d$ underneath a sea-surface wave field. The values are normalized by the averaged downward irradiance $\langle E_{d,0} \rangle$ of the incident light at the sea surface. The right panel shows vertical decay of plane-averaged downward irradiance $\langle E_d \rangle(z)$. The profile is normalized by its value at 1 m depth, $\langle E_{d,1} \rangle$. In this sample case, the inherent optical properties of the seawater are $(a, b) = (0.0257, 0.0029)\,\mathrm{m}^{-1}$ and diffuse attenuation coefficient is $K_d = 0.0271\,\mathrm{m}^{-1}$ [129]. The incident light is directed vertically. The horizontal domain size is $512\,\mathrm{m} \times 512\,\mathrm{m}$, and the vertical distances between the three planes in (a)–(c) are artificially increased to avoid blocking the view of the results. In this MCS test case, the inherent optical properties of the seawater for the 500 nm light are set to be $a = 0.0257\,\mathrm{m}^{-1}$, $b = 0.0029\,\mathrm{m}^{-1}$, and $c = a + b = 0.0286\,\mathrm{m}^{-1}$ [129]. There were totally $5 \times 10^{10}$ photon packets launched and tracked. As shown in the figure, the typical "swimming pool" effect associated with wave-induced light focusing is clearly visualized from the contours of the downward irradiance $E_d$ at two representative depths (Fig. 3.4(b) and 3.4(c)). The local downward irradiance is calculated as [165]

$$E_d(x, y, z) = \int_0^{2\pi} \int_0^{\pi/2} I(x, y, z; \theta, \varphi) |\cos\theta| \sin\theta \mathrm{d}\theta \mathrm{d}\varphi, \tag{3.10}$$

where $I(x, y, z; \theta, \varphi)$ is the local radiance obtained from the MCS model. The MCS result also captures the depth-dependent decay of the horizontally averaged downward irradiance $\langle E_d \rangle$. Note that the vertical attenuation of the downward irradiance can be expressed in the form of an exponential decay $\langle E_d \rangle = \langle E_{d,1} \rangle \exp[K_d(z - z_1)]$, where $\langle E_{d,1} \rangle$ is the average downward irradiance at the reference level $z_1 = -1\,\mathrm{m}$ and $K_d$ is the diffuse attenuation coefficient [65]. For this test case, $K_d = 0.0271\,\mathrm{m}^{-1}$ [129]. Figure 3.4(d) shows good agreement between the MCS result and the exponential decay profile. Additional validations for the MCS model can be found in A.2.

## 3.3 Results

### 3.3.1 Problem Setup

The upper-ocean boundary layer is a highly dynamic system, and it is nearly impossible to include all effects in a single modeling framework. To capture the detailed spatial variation of the light field, we choose to focus on small-scale effects (relative to submesoscale ocean eddies). As shown in Fig. 3.1, we consider the oil dispersion in the OML and the resulted light field variation under the influences of shear-induced turbulence, Langmuir circulations, sea-surface waves, and thermal convections. We consider two different sea-surface forcing conditions corresponding to shear-dominant and convection-dominant conditions. In the shear-dominant case, a constant wind shear stress $\tau_w = 0.168\,\mathrm{N\,m^{-2}}$ is applied in the $x$-direction, which corresponds to a wind speed $U_{10} = 10\,\mathrm{m/s}$ (measured at 10 m height) and a friction velocity $u_* = 1.28\,\mathrm{cm/s}$ in water based on empirical parameterization [39]. A weak heat flux of $Q = -15.5\,\mathrm{Wm^{-2}}$ (out of the ocean) is imposed at the surface to help spin-up the flow [92, 168, 169]. Under this condition, the OML flow is dominated by the three-dimensional turbulence generated by the wind-induced shear and the coherent Langmuir circulation cells generated by wave–turbulence interaction (the wave condition is discussed further below). In the rest of this chapter, we refer to this flow condition as LC. In the convection-dominant case we apply a weaker wind stress $\tau_w = 0.036\,\mathrm{N\,m^{-2}}$ (corresponding to wind speed $U_{10} = 5\,\mathrm{m/s}$ and friction velocity $u_* = 0.59\,\mathrm{cm/s}$ in water) and a stronger surface heat flux of $Q = -207.0\,\mathrm{Wm^{-2}}$. Under this condition, the convective cells generated by the thermal convection are the dominant flow structures, and hereinafter we refer to this condition as CC. For both flow conditions, we set the Coriolis frequency to be $f_c = 7 \times 10^{-5}\,\mathrm{s^{-1}}$, corresponding to a latitude of 28.7°N. Note that the surface heat flux imposed in the LES represents the combined effect of various surface heat transfer processes (e.g., convection, radiation and evaporation) [42], which are typically not modeled explicitly in the LES model based on the CL equation. Nevertheless, the surface wind stress and heat flux conditions considered in this study fall in the range of the parameters considered in previous LES studies of OML flows [e.g., 29, 54, 92, 95, 169].

For both flow conditions, we assume the sea-surface wave field is in equilibrium with the wind forcing. We adopt a widely used empirical broadband wave spectrum parameterization [40]. The wavelengths at the spectrum peak are $\lambda_p = 92.2\,\mathrm{m}$ for LC and 23.1 m for CC, and the corresponding wave periods are $T_p = 7.69\,\mathrm{s}$ and 3.85 s, respectively. Based on these empirical spectra, for each flow condition a three-dimensional broadband wave field is constructed and used as the initial condition for the HOSM to simulate the instantaneous sea-surface waves. Underneath the sea surface, we use a computational domain of 922 m long and wide and 100 m deep to simulate the oil dispersion in OML using LES with $384 \times 384 \times 256$ computational grid points. The flow field is well mixed in the top half of the domain corresponding to an OML depth $z_i = 50\,\mathrm{m}$, and stably stratified further below with a temperature gradient $\mathrm{d}\Theta/\mathrm{d}z = 0.01\,\mathrm{K\,m^{-1}}$. For the broadband wave conditions considered in this study, the corresponding Stokes drift currents are calculated by integrating the wave spectra [54, 82, 90, 158]. The corresponding turbulent number number is about the same for both the LC and CC conditions, $La_t = \sqrt{u_*/u_{s,0}} = 0.3$, where $u_*$ is friction velocity caused by wind shear and $u_{s,0}$ is the magnitude of the wave-induced Stokes drift velocity at the mean water surface level [92].

Following recent LES studies on oil plume dispersion in OML [e.g., 168, 169], we use the reference seawater density $\rho_0 = 1031.0\,\mathrm{kg/m^3}$ and viscosity $\mu_f = 1.08\times10^{-3}\,\mathrm{kg/(m\,s)}$, and the oil density $\rho_d = 859.9\,\mathrm{kg/m^3}$. For each flow condition, we consider three different cases differentiated by the droplet diameter, i.e., $d = 0.27$, 0.42 and 0.70 mm. These droplet diameters fall into the small size range (i.e., typically $d \leq 1$ mm) so that the droplets can be assumed to have spherical shape [32, 188], and are within the range of possible droplet size distributions reported for offshore oil spills [85]. For each case, a monodisperse oil plume with the same droplet size is released from a localized source at the 75 m depth with a low mass release rate of $Q_s = 10\,\mathrm{kg/s}$. In this way, the oil plume in each case models a near-surface sub-plume of oil droplets with similar size originated from a deep-water release (note that the sub-plumes with different droplet sizes would rise along different paths in the OML due to the differences in their rise velocities) [169]. The resulting oil concentration in the surface plume is found to be within the range of the concentration levels obtained from simulations based on the realistic scale blowout rate from the wellhead [26]. The local oil concentrations obtained from the LES runs are also found to be at a level that induce negligible buoyancy effect to the two OML flow conditions considered in this study.

In the MCS, the IOPs induced by naturally existing substances in the seawater, such as water molecules, suspended particulate matter, and colored dissolved organic matter, are prescribed based on empirical parameterizations [65, 98, 162]. The effects of oil droplets on the IOPs are modeled based on the simulated oil concentration using Mie theory [13] (see more details in A.2). We note that the radiative transfer in the upper ocean is also strongly affected by the wavelength of the light, as shown in A.2. In particular, the light absorption reaches the lowest order of $O(0.01)\,\mathrm{m^{-1}}$ in pure seawater around the light wavelength of 450 nm, and increases gradually to the order of $O(1)\,\mathrm{m^{-1}}$ towards both the ultraviolet and infrared ends of the light spectrum; the light scattering coefficient of pure seawater decreases monotonically as the light wavelength increases [98]. On the other hand, both the light absorption and scattering effects induced by suspended crude oil droplets decrease monotonically as the light wavelength increases [104]. Therefore, a large set of simulations for a range of representative wavelengths in the full light spectrum would need to be performed in order to obtain the complete picture for the effects of the oil plumes on the upper-ocean light field. However, to avoid further complicating the simulation and data analysis, in this study we only consider the radiative transfer of the 450 nm wavelength light, which is in the spectrum range for oceanic photosynthesis. Overall, in this study we conduct simulations and data analyses for 6 cases covering two different flow conditions with three different oil droplet sizes for each. Moreover, for comparison purpose, we also conduct two benchmark cases without oil plume for both the LC and CC flow conditions.

### 3.3.2 Simulation results and statistical analysis

As shown in Fig. 3.5(a), for the LC condition the interaction between wave-induced Stokes drift and shear-induced turbulence is able to generate Langmuir circulations [81, 92], as indicated by the streaky structures in the vertical velocity contours (i.e., the windrows); for the CC condition, the large surface heat flux causes strong thermal instability that dominates over the weaker Craik–Leibovich second type instability caused by wave–turbulence interaction [33], and the thermal convection cells become the main flow structures as shown in Fig. 3.5(b). Note that the vertical velocity field in the LC case fluctuates more energetically than that in the CC case due to the effect of the Langmuir circulations, as indicated by the vertical velocity contours shown in Fig. 3.5. The flow field features for the wind/wave dominant LC case and the the convection-dominant CC case are consistent with those reported in the literature [e.g., 92, 95]. In response to the flow-induced transport, the surface oil plume forms different patterns due to the different characteristics of the flow conditions.

In the LC condition the oil converges into narrow downwind bands (namely the surface windrows generated by contour-rotating Langmuir cells) [92, 168, 169], while in the CC condition the oil concentrates into surface patches (corresponding to convergence regions between convective cells) [30]. Moreover, as shown in Fig. 3.6, for the same flow condition the oil plume pattern is also strongly affected by the buoyancy of the oil droplet, which can be quantified by the floatability

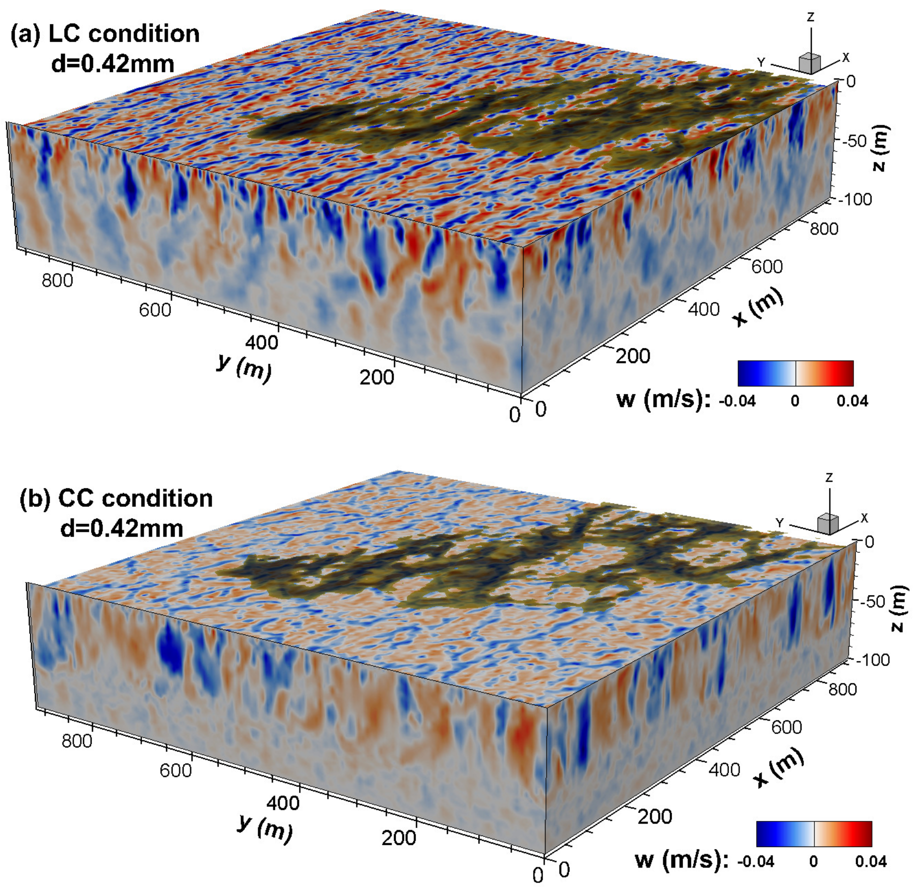


Figure 3.5: Sample LES results of velocity field and surface oil plumes for (a) LC and (b) CC conditions. The color contours denote the instantaneous vertical velocity $w$. The iso-surfaces of the oil concentration for $d = 0.42\,\mathrm{mm}$ are also plotted, indicated by darker color.

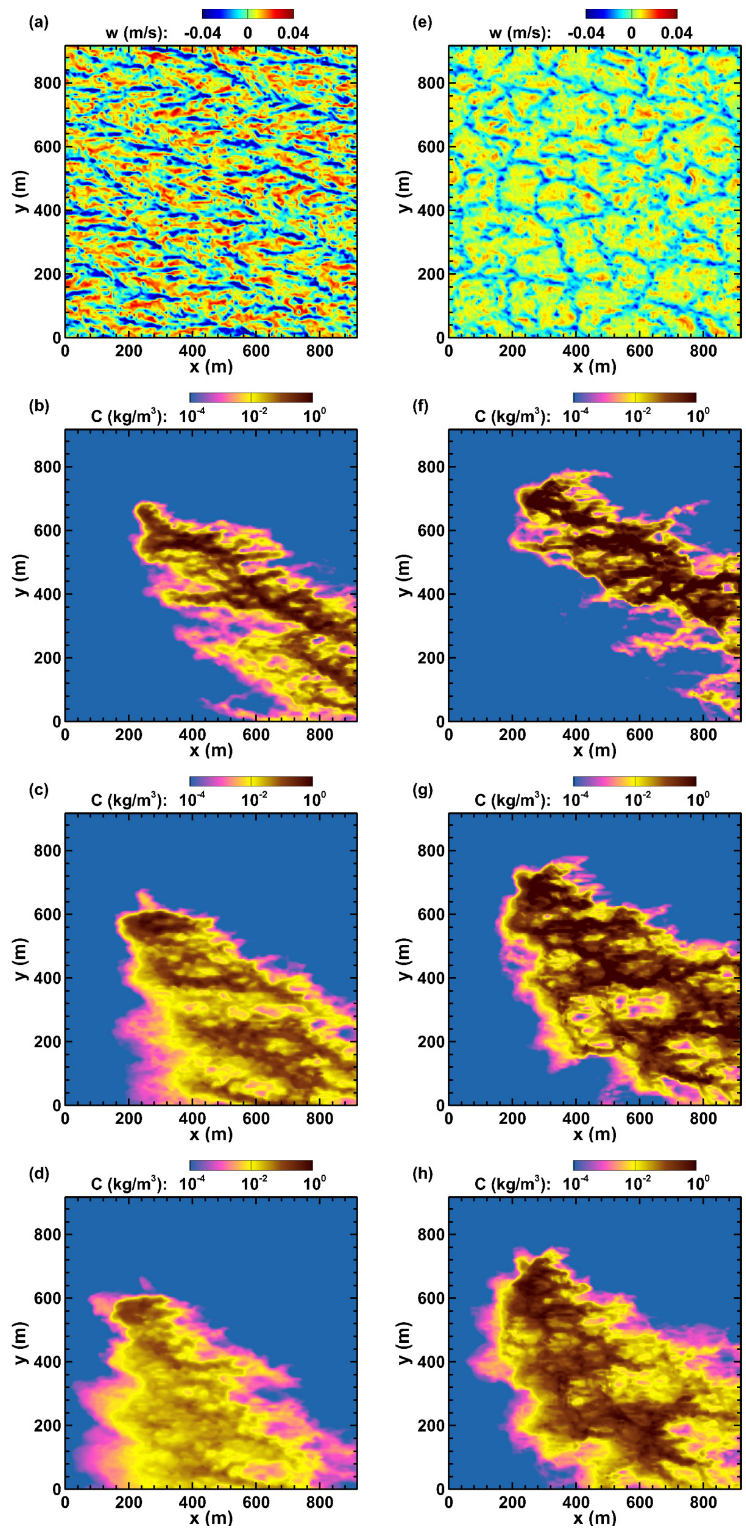


Figure 3.6: Instantaneous flow and oil plume fields for LC condition (a–d) and CC condition (e–h).

parameter $\beta = w_r/W$, where $w_r$ is the droplet rise velocity due to buoyancy and $W$ is a velocity scale representing the level of mixing induced by OML flows. Here, the panels show the contours of: (a, e) vertical velocity $w$ on the horizontal plane at $z = -9$ m depth; and oil mass concentration $C$ on the ocean surface ($z = 0$, m) for cases with droplet diameters of (b, f) $d = 0.70$ mm, (c, g) $d = 0.42$ mm, and (d, h) $d = 0.27$ mm. For the LC condition, $W$ can be set to be the surface Stokes drift velocity $u_{s,0}$ and $\beta = w_r/u_{s,0} = Db^{-1}$, where $Db$ is the drift-to-buoyancy ratio proposed by [168]. As shown in Fig. 3.6(b–d), the oil plume exhibits highly intermittent surface pattern with high local concentration in windrows when $\beta$ is large and volumetrically diffused smooth pattern when $\beta$ is small [168, 169]. For the CC condition, $W$ can be set to be the Deardorff convective velocity $w_* = (g\alpha_t \langle w'\Theta' \rangle_s z_i)^{1/3}$, where $g$ is the gravitational acceleration, $\alpha_t$ is the thermal expansion coefficient, $w'$ is the vertical velocity fluctuation, $\Theta'$ is the temperature fluctuation, $z_i$ is the OML depth, and $\langle \cdot \rangle_s$ denotes a Reynolds average at the surface (in practice, it is computed at the first LES grid below the mean sea surface level) [30]. It is worth mentioning that very recently, a more general form for the turbulence velocity scale $W$ has been proposed to account for various levels of wind shear, Stokes drift, and buoyancy flux [29].

Because the oil transport in the OML and the resulted light field variation are highly three dimensional (Fig. 3.1), this requires us to analyze both the horizontal and the vertical distributions of the oil concentration and their effects on the light field. Figure 3.7 shows several representative instantaneous snapshots of oil concentration on the surface and the corresponding sub-surface light field at 10 m depth, where (a) LC condition with oil droplet diameter $d = 0.70$ mm; (b) LC condition with oil droplet diameter $d = 0.27$ mm; (c) CC condition with oil droplet diameter $d = 0.70$ mm; (d) CC condition with oil droplet diameter $d = 0.27$ mm. The vertical variations on the oil and light fields are illustrated by the vertical profiles of horizontal average statistics shown in Figs. 3.8 and 3.9, where (a) oil-contaminated area $A$ (normalized by the total horizontal area $A_0$); (b) oil mass concentration $\langle C \rangle_A$; (c) beam attenuation coefficient $\langle c \rangle_A$; and (d) normalized deficit of downward irradiance $\langle E_{d,r} - E_d \rangle_A / \langle E_{d,0} \rangle_A$, where $E_d$ is the downward irradiance in oil-contaminated seawater, $E_{d,r}$ is the reference downward irradiance obtained from simulation based on natural seawater, and $E_{d,0}$ is the downward irradiance of the incident light above the sea surface imposed in MCS. The results for simulation cases with different oil droplet diameters are denoted by different line

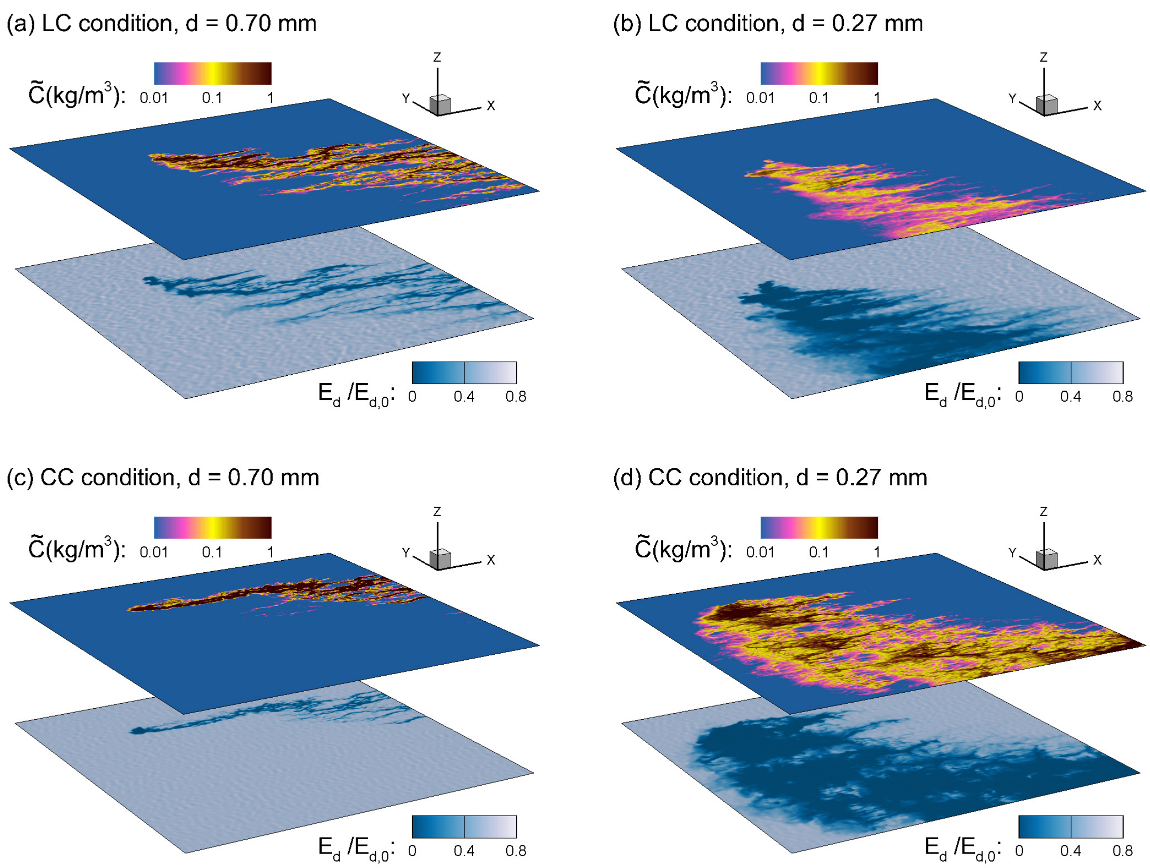


Figure 3.7: Surface oil concentration (shown on the upper plane in each panel) and subsurface downward irradiance at 10 m depth (shown on the lower plane in each panel).

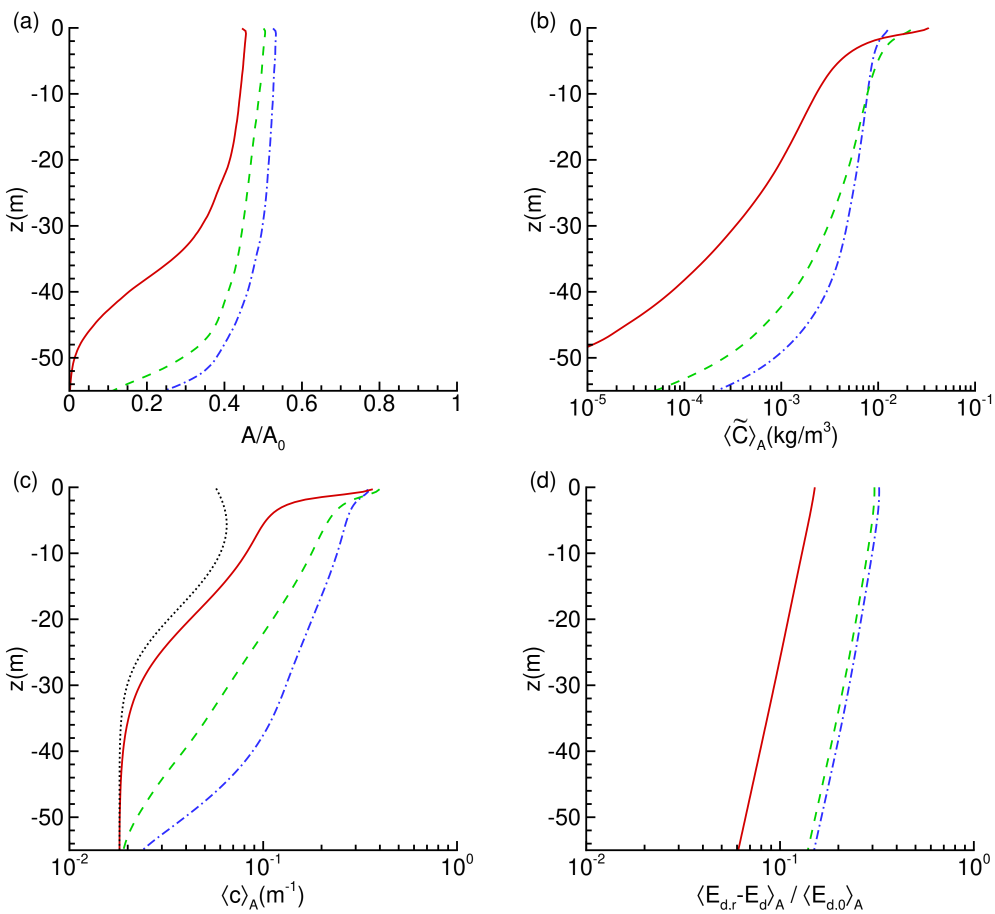


Figure 3.8: Vertical profiles of horizontal average statistics for cases under the LC flow condition.

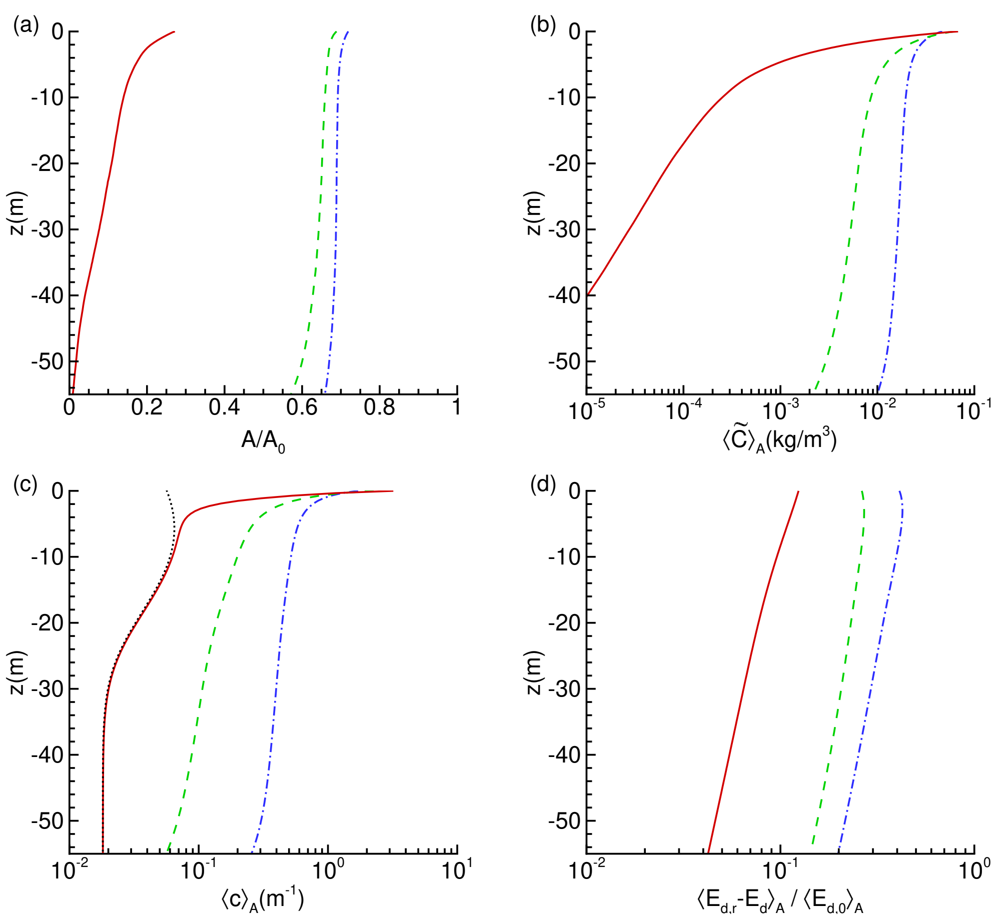


Figure 3.9: Vertical profiles of horizontal average statistics for cases under the CC flow condition. The panel arrangement and line legend have the same format as in Fig. 3.8.

patterns: solid line for $d = 0.70$ mm; dashed line for $d = 0.42$ mm; dash-dot line for $d = 0.27$ mm. In (c), the black dotted line shows the reference beam attenuation coefficient $c$ for natural seawater We analyze the effect of the oil on the sub-surface light field by quantifying the beam attenuation coefficient $c$ and the downward irradiance $E_d$ [98, 165].

When calculating horizontal average, we focus on the flow regions contaminated by the dispersed oil plume, which can be determined statistically based on the time average of the vertically integrated oil concentration [26]. Previous study has shown that the averaged oil plumes are smooth and continuous even when the instantaneous oil field is highly intermittent [169]. As shown in Figs. 3.8(a) and 3.9(a), the horizontal area $A$ of the average oil-contaminated region increases as the droplet floatability decreases. Plumes of large oil droplets possess strong floatability to overcome the downwelling motion induced by Langmuir circulations and thermal convection, forming high-concentration surface plumes that cover relatively small regions near the surface; plumes of small oil droplets have weak floatability and can be dispersed widely by OML flows over large horizontal and vertical extensions, which also dilute the local oil droplet concentration to relatively low level ([29, 30, 168]).

The statistics of the oil plume and light field can be obtained by performing horizontal average within $A$, which is denoted as $\langle \cdot \rangle_A$. As shown in Figs. 3.8(b) and 3.9(b), plumes of larger droplets tend to have higher average concentration near the surface with rapidly decreased concentration towards deeper depth, while plumes of smaller droplets have more smooth vertical distribution of oil concentration. As a result, the oil plumes with $d = 0.70$ mm cause significant increase of light attenuation coefficient near the surface, but this effect decreases quickly with depth due to the decrease of oil concentration (Figs. 3.8(b) and 3.9(b)). For the cases with $d = 0.42$ mm and $d = 0.27$ mm, although the increase of light attenuation coefficient near the surface is less significant than that in the case with $d = 0.70$ mm, this effect persists over much deeper depth due to the much smoother distribution of oil droplets over the seawater column (Figs. 3.8(c) and 3.9(c)). Combining the effects of the vertical oil distribution, horizontal intermittency level of the oil plume and difference in local oil concentration (Fig. 3.6), the oil plumes with smaller droplets result in more significant deficit for the downward irradiance than the plumes with larger droplets, even though the latter have higher local oil concentration near the surface (Figs. 3.8(d) and 3.9(d)).

It should be pointed out that this study focuses on modeling the effects of monodispersed surface oil plumes on upper-ocean radiative transfer with idealized oceanic and oil release conditions. Separating oil plumes with different droplet sizes into different simulation cases allows us to connect the droplet size, oil plume dilution pattern and the radiative transfer. With the recent advancements on modeling oil droplet size distribution in subsea blowouts [85, 132, 184, 185], LES of polydispersed oil plumes can be performed to obtain in-situ modeling of more realistic surface plume with the mixture of various droplet sizes, which will be a subject of future study. As the initial attempt, in this study we limit to the idealized setup considering the high level of complexity and computational cost involved in applying several high-fidelity numerical models.

## 3.4 Conclusion and Discussion

This study combines the strengths of several high-fidelity numerical models for simulating various physical processes (i.e., wave mechanics, oil plume dispersion by OML turbulent flows, and radiative transfer through the complex oil/seawater mixture medium) to help improve our understanding on the impact of offshore oil spills on ocean light field. Due to the high complexity of the physical processes, by no mean this study is meant to capture all the relevant physics in this problem. Nevertheless, the simulation results presented here show that plumes of oil droplets can significantly reduce the downward irradiance of the light in the ocean euphotic zone, and this effect is strongly affected by the dynamic interaction between oil and OML flows governed by the oil droplet floatability. While in general the presence of oil plume can cause considerable reduction to the downward irradiance, this effect appears to be more significant for plumes of smaller oil droplet sizes because these plumes are dispersed more widely by the OML flows. This finding suggests that additional effect to the ocean ecosystem caused by the variation of ocean light field may need to be taken into consideration when applying dispersant for oil spill remediation and response, as dispersant can significantly reduce the oil droplet size. Moreover, it is worth mentioning that the numerical models used in this study can also be applied to simulate the backscattered light signal of surface oil plumes, which can provide useful insights to help link the remote sensing signals to the surface and subsurface characteristics of the oil plumes to support the decision making process for future oil spill response and remediation. Moreover, even though the reduced downward irradiance obtained from this study can be used to estimate the potential impact of oil plumes on the phytoplankton photosynthesis rate, the direct calculation of the phytoplankton population evolution and photosynthesis rate are not included in the current model. With the continuous advancement in computer power and numerical model capability, these additional features may be included into the current modeling framework. These are the subjects for future research.

# Chapter 4

# Large-eddy simulation-based study of effect of swell-induced pitch motion on wake-flow statistics and power extraction of offshore wind turbines

## 4.1 Introduction

Continuous growth of global energy consumption has imposed great challenges to the energy supply. In recent years, wind energy has been playing a vital role in providing clean and renewable energy to fulfill the demand without generating major adverse impact on the environment as other conventional energy sources based on fossil fuels [161]. As available and suitable land spaces for building onshore wind farm are limited, offshore wind power is becoming an emerging direction for future wind energy research [160, 182]. Without resistance caused by ground obstacles like in the onshore environments, offshore wind in the marine atmospheric boundary layer (ABL) usually possesses higher wind speed than its onshore counterpart, offering higher wind power density for energy harvesting. On the other hand, the marine ABL turbulence also exhibits complex flow phenomena in its lower portion where the wind and sea-surface waves interact extensively, imposing considerable challenges to the design of individual offshore wind turbines as well as large offshore wind farms.

The characteristics of offshore wind are highly affected by the dynamic interactions between wind turbulence and progressive sea-surface waves in the marine ABL [42, 149]. For wind energy application, local wind-generated broadband sea-surface waves (often called the wind-sea) can be regarded as moving surface roughness elements, which affect the lower portion of the ABL through the effective surface friction [148, 168]. In addition, long-wavelength swell waves generated by remote storm events can maintain their long-crest shapes after propagating over long distance and impact local flow field in offshore environments [146, 173]. Due to the their well-organized wave forms and large surface orbital velocities (associated with their long wavelength of $\lambda_{sw} \sim O(100)\,\mathrm{m}$ and fast phase speed of $c_{sw} \sim O(10)\,\mathrm{m/s}$), swell waves can induce strong distortions to the near-surface wind field that can extend up to the height of $\sim O(\lambda_{sw})$ [146]. Considering the wind–wave coupled dynamics is crucial for understanding the offshore wind power resource and predicting the performance of offshore wind turbines.

In addition to modulating the offshore wind field, the energetic swell waves can also cause considerable oscillating motions for floating turbine platforms, which further complicates the dynamics of offshore wind energy systems and affects their performance. Recently, [118, 119] performed laboratory experiments using a wind turbine model installed on a gimbal support to study the effect of turbine pitch motion on the wake flow statistics. Using the particle image velocimetry technique, they measured and quantified the turbulence statistics in the turbine wake. Although the effects of water waves on wind were not included in their experiment, the experimental data showed considerable effects of the turbine pitch motion on the wake flow statistics. Using the free vortex method, [159] studied the power extraction of a single floating turbine and found considerable influence of the platform pitch motion on the floating turbine's power performance. Despite of the improved understanding of the pitch motion effects on the performance and structure dynamics of a single wind turbine, the effects of turbine pitch motion on the flow structures and turbine performance in an offshore wind farm environment are still not well understood.

In recent years, large-eddy simulation (LES) method combined with actuator-disk model (ADM) of wind turbine has become a valuable tool for studying the flow physics in the turbulent flow behind a single turbine [139] or within large wind farms [140]. For example, [18, 19] performed pioneering studies using LES and ADM to simulate the complex turbulent flow physics, vertical kinetic energy entrainments and scalar transport in fully developed wind turbine array boundary layer. [138] [138] performed a set of LES runs to quantify the effects of turbine alignment and wind farm length on the turbine performance within a large wind farm. [141] investigated the temporal fluctuations of wind power extraction rate based on LES data of extended wind farms. [151] performed extensive statistical analyses of LES data for wind farms using three-dimensional proper orthogonal decomposition approaching and identified various large coherent flow structures at the wind turbine array scale that are associated with vertical kinetic energy entrainments to supply wind energy into the wind turbine arrays in the middle of very large wind farms. [177] simulated infinite aligned wind farms with various turbine spacings to quantify the effects of turbine packing density on the wind energy harvest. [178] studied the effect of staggered turbine layouts on the wind power extraction of large wind farm. [183] explored the potential benefit of using vertically staggered turbine layouts to enhance wind power production of a turbine array. [168] [168, 173] coupled LES with wave simulation based on high-order spectral method (HOSM) and studied the effect of wind-sea as well as swell waves on the flow structures and turbulence in offshore wind farms with fixed turbines. [87] further extended the model of [168, 173] by also adding the actuator line model and actuator disk model with rotational effect for the turbines.

In this chapter, we use the LES–HOSM model of [168, 173] to study the effect of swell-induced pitch motion on the turbulence statistics and wind power extraction rate in an array of floating wind turbines. We consider long swell waves that propagate in the downwind direction. The simulations of wind and swell waves are coupled in order to capture the strong swell-induced disturbances on the near-surface wind field and their effects on the wind energy extraction. Similar to previous LES studies [18, 19], we consider an array of wind turbines in horizontally and vertically aligned layout. With periodic boundary condition applied in the horizontal directions, the simulation models the interaction of ABL wind with an "infinite" turbine array, which represents the flow physics in the fully developed region within a very large wind farm [18, 140]. We simulate the floating turbines with prescribed periodic pitch motion under the influence of wind and swell wave forcing, and compare the simulation results to a reference case with identical condition but fixed turbines. The LES data are analyzed using phase average approach by sampling flow field snapshots at specific phases with respect to the swell wave form, which allows us to educe the swell-correlated turbulence statistics from this complex flow problem. Time series of the wind power extraction rate are also quantified to reveal the impact of swell-induced wind speed variation and turbine pitch motion on wind energy harvesting.

This chapter is organized as follows. Section 4.2 discusses the model equations and numerical schemes used in LES and HOSM. Section 4.3 shows the data analysis results for the statistics of the wind turbulence in the turbine array boundary layer and the wind power extraction rate. Finally, conclusions are given in section 4.4.

## 4.2 Problem Description and Numerical Methods

### 4.2.1 Large-Eddy Simulation Model for Wind Field

In the LES model, the wind flow motions in a neutral atmospheric boundary layer are simulated by solving the filtered Navier–Stokes equations [18, 138, 168, 173, 178]

$$\widetilde{\mathbf{u}}t + \widetilde{\mathbf{u}} \cdot \nabla \widetilde{\mathbf{u}} = -\frac{1}{\rho_a} \nabla \widetilde{P} - \nabla \cdot \boldsymbol{\tau}^d - \frac{1}{\rho_a} \frac{\mathrm{d}p_\infty}{\mathrm{d}x} \mathbf{e}_x + \mathbf{f}_t \tag{4.1}$$

and

$$\nabla \cdot \widetilde{\mathbf{u}} = 0 \; . \tag{4.2}$$

The model equations are defined based on regular Cartesian coordinate system $\mathbf{x} = (x, y, z)$, where $x$ and $y$ are the horizontal coordinates and $z$ is the vertical coordinate. The origin of the $z$ coordinate is set to be at the mean water level near the instantaneous bottom boundary. In Eqs. (4.1) and (4.2), $\mathbf{u} = (u, v, w)$ is the velocity vector with $u$, $v$ and $w$ being the corresponding velocity components in the $x$-, $y$-, and $z$-directions, respectively; the tilde denotes a variable resolved by the LES grid scale; $\rho_a$ is the density of air; $\boldsymbol{\tau} = (\widetilde{\mathbf{u}\mathbf{u}} - \widetilde{\mathbf{u}}\widetilde{\mathbf{u}})$ is the subgrid-scale (SGS) stress tensor with $\mathrm{tr}(\boldsymbol{\tau})$ being its trace and $\boldsymbol{\tau}^d = \boldsymbol{\tau} - [\mathrm{tr}(\boldsymbol{\tau})/3]\mathbf{I}$ being its deviatoric part, where $\mathbf{I}$ is the identity tensor; $\widetilde{P} = \widetilde{p} + \rho_a \mathrm{tr}(\boldsymbol{\tau})/3 + \rho_a |\widetilde{\mathbf{u}}|^2/2$ is the pseudo pressure with $p$ being the dynamic pressure; $\mathrm{d}p_\infty/\mathrm{d}x$ is the imposed pressure gradient to model the effect of geostrophic wind forcing [18, 19]; $f_t$ is the turbine-induced force on the wind field; and $\mathbf{e}_x$ is the unit vector in the $x$-direction. In Eq. (4.1), the effect of molecular viscosity is neglected because the Reynolds numbers for ABL flows in wind energy applications are typically quite high so that the effects of unresolved SGS terms dominate over the molecular viscous terms [18]. We note that for large wind farms, the thermal stability conditions of the ABL can also affect the dynamic interactions between wind farms and the ABL flows [e.g., 4, 41]. For the sake of simplicity and to allow us focus on studying the effect of sea-surface waves on the offshore wind farm flows, in this study we limit our analysis to the neutral ABL condition similar to many prior LES studies of wind farms.

In the current LES model, the effect of turbine rotor on the wind velocity field is modeled using the actuator-disk model [59, 60, 96, 102]. Following [96], the turbine-induced force $f_t$ (per unit mass of air) is modeled as

$$\mathbf{f}_t(x_i, y_j, z_k) = -\frac{1}{2}\frac{C_t}{(1-a)^2}\langle u_T\rangle_d^2 \frac{\gamma_{i,j,k}}{\Delta x}(\cos\beta\,\mathbf{e}_x - \sin\beta\,\mathbf{e}_z)\ . \tag{4.3}$$

Here, $(x_i, y_j, z_k)$ denotes the coordinates of the discretized LES grid point with index $(i, j, k)$; $C_t = 3/4$ is the thrust coefficient and $a = 1/4$ is the induction factor [18, 59]; $\langle u_T\rangle_d$ is the local reference wind velocity evaluated by spatial averaging the relative wind-to-rotor velocity (by including the effect caused by the pitch motion of the floating turbine platform and taking the component perpendicular to the rotor disk plane) over all grid points within the turbine disk [18, 96]; $\gamma_{i,j,k}$ is the fraction of area overlap between the grid cell area around point $(i, j, k)$ and the turbine rotor circle, combined with the bilinear interpolation coefficient when the turbine rotor disk plane is not overlapping with the index-$i$ grid plane if the turbine platform has pitch motion; $\Delta x$ is the grid size in the $x$-direction; $\beta$ is the pitch angle of the rotor disk plane with respect to the vertical plane (defined to be positive towards downwind direction); and $\mathbf{e}_z$ is the unit vector in the $z$-direction. The last term in Eq. (4.3) is included to project the turbine disk force into the streamwise and vertical directions based on the pitch angle $\beta$.

In Eq. (4.1), the SGS stress tensor $\boldsymbol{\tau}^d$ is parameterized using the Lilly–Smagorinsky eddy-viscosity type model [86, 128], $\boldsymbol{\tau}^d = -2\nu_\tau\widetilde{\mathbf{S}} = -2(c_s\Delta)^2|\widetilde{\mathbf{S}}|\widetilde{\mathbf{S}}$, where $\widetilde{\mathbf{S}} = (\nabla\widetilde{\mathbf{u}} + \nabla\widetilde{\mathbf{u}}^{\mathrm{T}})/2$ is the resolved strain rate tensor with the superscript 'T' standing for the transpose of tensor, $\nu_\tau$ is the SGS eddy viscosity, and $\Delta$ is the LES grid (filter) scale. The Smagorinsky coefficient $c_s$ is determined dynamically using the Lagrangian-averaged scale-dependent (LASD) dynamic SGS model, which is chosen because of its feasibility for modeling turbulent flows with strong spatial inhomogeneity [15]. The LASD model has been successfully applied in several prior LES studies of turbulent flows in wind turbine arrays boundary layers [e.g., 18, 19, 138, 141, 168, 173].

For LES of high Reynolds number wind turbulence, it is impractical to directly resolve the viscous boundary layer near the water surface. In this chapter, a wall-layer model is used to model the proper surface SGS stress for the wind velocity to satisfy the no-slip condition, which is given by [15, 146, 153]

$$\tau^d_{xz}\Big|_{z=\tilde{\eta}} = -\left[\frac{\kappa}{\ln\left(d_2/z_0\right)}\right]^2 \widehat{\widetilde{U}}_r \left(\widehat{\widetilde{u}}_r \cos\alpha_x + \widehat{\widetilde{w}}_r \sin\alpha_x\right) , \tag{4.4}$$

and

$$\tau^d_{yz}\Big|_{z=\tilde{\eta}} = -\left[\frac{\kappa}{\ln\left(d_2/z_0\right)}\right]^2 \widehat{\widetilde{U}}_r \left(\widehat{\widetilde{v}}_r \cos\alpha_y + \widehat{\widetilde{w}}_r \sin\alpha_y\right) , \tag{4.5}$$

where

$$\cos\alpha_x = (1+\tilde{\eta}_x^2)^{-1/2}, \tag{4.6}$$

$$\sin\alpha_x = \tilde{\eta}_x(1+\tilde{\eta}_x^2)^{-1/2} , \tag{4.7}$$

$$\cos\alpha_y = (1+\tilde{\eta}_y^2)^{-1/2}, \tag{4.8}$$

and

$$\sin\alpha_y = \tilde{\eta}_y(1+\tilde{\eta}_y^2)^{-1/2} . \tag{4.9}$$

Here, $\tilde{\eta}(x,y,t)$ is the instantaneous wave surface elevation filtered by the LES grid scale $\Delta$; $\kappa = 0.4$ is the von Kármán constant; $(\widehat{\widetilde{...}})$ denotes variables filtered at the test-filter scale $2\Delta$; $z_0$ is the sea-surface roughness associated with unresolved short waves; $(\widehat{\widetilde{u}}_r, \widehat{\widetilde{v}}_r, \widehat{\widetilde{w}}_r)$ are the filtered wind velocities relative to the water surface at the first off-surface grid point (note that in the current LES the actual $z$-coordinate value of this grid point varies in time and space due to the wave motions, and $d_2$ denotes its instantaneous vertical distance to the local wave surface),

$$\widehat{\widetilde{u}}_{r,i}(x,y,t) = \widehat{\widetilde{u}}_i(x,y,d_2,t) - \widehat{\widetilde{u}}_{s,i}(x,y,t) , \quad i = 1,2,3 , \tag{4.10}$$

$\mathbf{u}_s = (u_s, v_s, w_s)$ is the instantaneous sea-surface wave orbital velocity; and

$$\widehat{\widetilde{U}}_r(x,y,t) = \sqrt{\left[\widehat{\widetilde{u}}_r(x,y,t)\cos\alpha_x + \widehat{\widetilde{w}}_r(x,y,t)\sin\alpha_x\right]^2 + \left[\widehat{\widetilde{v}}_r(x,y,t)\cos\alpha_y + \widehat{\widetilde{w}}_r(x,y,t)\sin\alpha_y\right]^2}\,. \tag{4.11}$$

Note that the logarithmic similarity law-of-the-wall is expected to be obeyed by the flow in the averaged context. Here to apply it locally in LES, the velocities used in Eqs. (4.4) and (4.5) need to be filtered at the scale $2\Delta$ to suppress unphysical velocity fluctuation near the boundary (see more details in Ref. [15]). Similar filtering treatment has been applied in several prior LES studies of ABL flows [5, 18, 19, 74, 138].

The LES model is coupled with a high-order spectral wave model to obtain the instantaneous sea-surface wave elevation $\eta$ and surface orbital velocities $\mathbf{u}_s = (u_s, v_s, w_s)$ required for getting the proper bottom boundary condition for LES [171]. More details of the HOSM wave model is given in the next subsection. To simulate the wind field near the wave surface, the LES model uses a time-dependent boundary-fitted computational grid to follow the instantaneous wave surface geometry. The simulation domain with complex bottom boundary deformation in the physical space $(t, x, y, z)$ is transformed to a right rectangular prism in the computational space $(t', x', y', z')$ using algebraic mapping [171, 174, 175]: $t' = t$, $x' = x$, $y' = y$, $z' = (z - \widetilde{\eta})/(\overline{H} - \widetilde{\eta})$, where $\overline{H}$ is the average domain height.

In this chapter, we consider the scenario of a very large wind farm in an open-sea environment. In the streamwise and spanwise directions, we use periodic boundary conditions and the equations are discretized using a Fourier-series-based pseudo-spectral method on a collocated grid. In the vertical direction, a free-slip condition is applied at the top boundary and the law-of-the-wall Eqs. (4.4) and (4.5) are applied at the bottom boundary. The equations are discretized using a second-order central finite-difference scheme on staggered grid points in the vertical direction. The Navier–Stokes equations are advanced in time using a prediction–correction fractional-step method, in which the momentum equation is integrated in time using a second-order Adams–Bashforth scheme to get a prediction of the velocity at the new timestep and then a Poisson equation is constructed and solved to obtain the pressure field to correct the predicted velocity field to satisfy the divergence free condition [171].

### 4.2.2 High-Order Spectral Simulation of Sea-Surface Waves

The instantaneous sea-surface waves can be efficiently simulated using the high-order spectral method [2, 38, 93]. In this method, the wave motions are described in physical space based on the potential flow theory in which the viscous effect is neglected when modeling the wave dynamics. The wave orbital velocity satisfies $\mathbf{u}_w = \nabla\Phi$, where $\Phi(x, y, z, t)$ is the velocity potential. The mass conservation in the wave flow field yields the continuity equation $\nabla^2\Phi = 0$. On the sea surface, the wave satisfies both the kinematic and dynamic free-surface boundary conditions defined at the instantaneous wave surface $z = \eta(x, y, t)$ using Zakharov's equations [181],

$$\frac{\partial\eta}{\partial t} + \nabla_{xy}\eta \cdot \nabla_{xy}\Phi^s + \left(1 + |\nabla_{xy}\eta|^2\right) \left.\frac{\partial\Phi}{\partial z}\right|_{z=\eta} = 0 \tag{4.12}$$

and

$$\frac{\partial\Phi^s}{\partial t} + g\eta + \frac{|\nabla_{xy}\Phi^s|^2}{2} + \frac{p_a}{\rho_w} - \frac{1}{2}\left(1 + |\nabla_{xy}\eta|^2\right)\left(\left.\frac{\partial\Phi}{\partial z}\right|_{z=\eta}\right)^2 = 0\,, \tag{4.13}$$

where $\Phi^s = \Phi|_{z=\eta}$ is the surface potential, $\nabla_{xy} = (\partial/\partial x, \partial/\partial y)$ is the horizontal gradient, $g$ is the gravitational acceleration, and $\rho_w$ is the water density. The pressure term $p_a$ accounts for the contributions from both the LES-resolved air dynamic pressure $\widetilde{p}$ and the trace of the SGS stress tensor $\boldsymbol{\tau}$, i.e., $p_a = \widetilde{p} + \rho\,\mathrm{tr}(\boldsymbol{\tau})/3 = \widetilde{P} - \rho|\widetilde{\mathbf{u}}|^2/2$, where the pseudo-pressure $\widetilde{P}$ and LES-resolved velocity $\widetilde{\mathbf{u}}$ are obtained by solving the LES equations (4.1) and (4.2).

In the HOSM, the velocity potential $\Phi$ is rewritten into a series of perturbation modes $\Phi^{(m)}$ with respect to the wave steepness, and the surface potential $\Phi^s$ is related to these perturbation modes using Taylor series expansion with respect to the mean surface level at $z = 0$. For open-sea condition, the wave field is assumed to satisfy periodic boundary conditions in the horizontal directions. Thus, $\Phi^{(m)}$ is further decomposed using eigenfunction expansion with Fourier modes in the horizontal directions, and its vertical variation with depth is written directly based on classical wave theories. Full details of the HOSM model equations and theoretical basis can be in Refs. [38] and [93]. To simulate the complex wave field efficiently, Eqs. (4.12) and (4.13) in the perturbation format are discretized in the horizontal direction using the Fourier series based pseudo-spectral method, and integrated in time using a fourth-order Runge–Kutta scheme. At each timestep after the values of $\eta$, $\Phi$ and $\Phi^s$ are computed, the wave orbital velocities at the sea surface are obtained

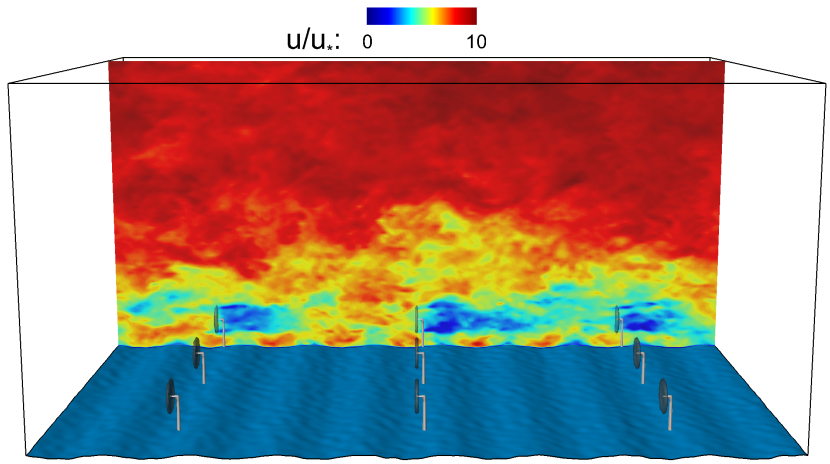


Figure 4.1: Illustration of 3D instantaneous wind and swell wave fields in a fully developed offshore wind turbine array boundary layer. Contours of instantaneous streamwise wind velocity are plotted on the vertical plane across the center of 3th column of turbines.

as [38]

$$u_s(x,y,t) = \Phi^s x - \eta x \; \Phi z|_{z=\eta} \,, \tag{4.14}$$

$$v_s(x,y,t) = \Phi^s y - \eta y \; \Phi z|_{z=\eta} \,, \tag{4.15}$$

and

$$w_s(x,y,t) = \Phi z|_{z=\eta} \,, \tag{4.16}$$

which are used in the bottom boundary condition equations (4.4)–(4.11) for the LES model.

### 4.2.3 Problem setup

In Fig. 4.1, the turbine rotor disks are illustrated by the black circular disks representing where actuator-disk model forces are applied. The turbine towers and nacelles (shown in gray color) are also plotted for illustration purpose only, and their effects are not considered in the simulations. Here, we use a computational domain of $(L_x, L_y, \overline{H}) = (2100, 1500, 1000)$ m. Within this domain, we model a $N_r \times N_c = 3 \times 3$ array of turbines with hub height $H_{hub} = 100$ m and rotor diameter $D = 100$ m, where $N_r$ and $N_c$ are the number of turbine rows and columns included in the simulation domain. This corresponds to a streamwise turbine spacing parameter $s_x = (L_x/N_r)/D = 7$

and spanwise spacing parameter $s_y = (L_y/N_c)/D = 5$ similar to prior LES studies [18, 19]. The ratio $\overline{H}/H_{hub} = 10$ has been found to be sufficient for avoiding artificial effect from the top boundary to the fluid dynamics in the turbine layer [18, 19, 96, 177]. In the LES, the wind flow is driven by an imposed streamwise pressure gradient $\mathrm{d}p_\infty/\mathrm{d}x$ as in Eq. (4.1), which is related to the wind friction velocity for the unperturbed (i.e., without wind turbine array) ABL flow as $u_* = \sqrt{-(\mathrm{d}p_\infty/\mathrm{d}x)\overline{H}/\rho_a}$. In this study, we consider a representative wind friction velocity of $u_* = 0.45\,\mathrm{m/s}$ [18].

The sea-surface wave field considered in this study consists of two parts, one corresponding to the background three-dimensional wind-waves following the JONSWAP broadband wave spectrum [55] with the peak wavelength $\lambda_p = 60\,\mathrm{m}$, and the other representing a two-dimensional swell wave train with wavelength $\lambda_{sw} = 233.3\,\mathrm{m}$ and steepness $2\pi a_{sw}/\lambda_{sw} = 0.1$, where $a_{sw}$ is the amplitude of the swell. The corresponding swell wave phase speed is $c_{sw} = 19.1$ m/s and swell period is $T_{sw} = 12.2\,\mathrm{s}$. We consider the swells propagating in the downwind direction (i.e., the $x$-direction). This setup includes 9 swell waves within the streamwise simulation domain, so that each turbine is located at the same swell wave phase for the convenience of statistical analysis using phase average method (details given in section 4.3.1). In addition, a SGS roughness length scale $z_0 = 2 \times 10^{-4}\,\mathrm{m}$ is imposed at the wave surface in the LES to represent the effect of unresolved short waves on the wind field [146, 168]. We consider two different turbine platform conditions, one with fixed turbine (corresponding to fixed platforms or floating platforms with limited oscillations) [120, 157], and the other with a prescribed swell-induced pitch motion (corresponding to floating platforms that exhibit more oscillations under strong wave forcing, e.g., the NREL shallow drafted barge platform concept) [62]. We note that accurately modeling the motions of the floating turbine platform is a very rich and challenging research topic by itself [e.g., 83, 84, 126], especially under high sea state conditions [e.g., 11]. For simplification, we consider only the dominant pitch motion of the turbine with a steady pitch angle of 4 degrees plus a periodic oscillation mode with an amplitude of 5 degrees and a phase angle of $-81.9$ degrees relative to the phase of the swells. Figure 4.2 illustrates the relation between the turbine pitch motion and the sea-surface swell waves. Note that the prescribed pitch motion is estimated without considering the complex interactions between wind, waves and turbine platform. A more accurate representation of the

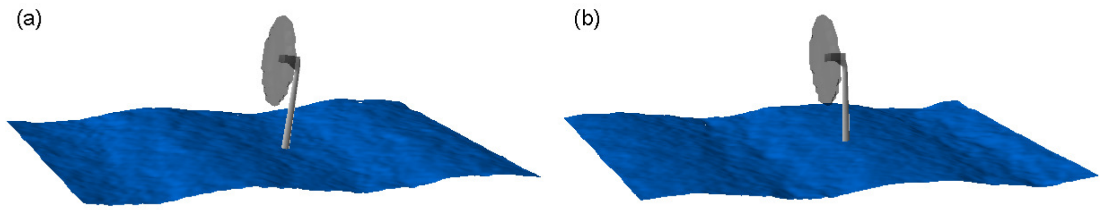


Figure 4.2: Illustration of the turbine pitch motion caused by swell waves: (a) turbine at its maximum downwind pitch position when swell's forward slope arrives; and (b) turbine at its maximum upwind pitch position when swell's backward slope arrives.

turbine motion may be obtained by coupled wind–wave–turbine simulations, which is challenging and computationally expensive and is a comprehensive research topic by itself. For simplicity, in this study we limit our analysis to the idealized condition by keeping in mind of its limitation on direct application to practical offshore turbine operations. We focus on studying the effect of the prescribed turbine pitch motion on the wake flow statistics and wind power extraction rate to get useful insights for potential impact of platform pitch motion on turbine performance.

We note that in the current simulation setup, all the turbines modeled in the simulation domain experiences the same swell phase at the same time. This configuration is chosen on purpose for the convenience of calculating the swell phase average statistics as will be discussed in next section. As can be found in the statistical results shown in next section, the sufficient streamwise turbine spacing ensures that the pitch-correlated variations in the wind turbulence are only significant in the near-wake region, and are dissipated by the wind turbulence before the wake reaches the next turbine. So although the choice of domain size and turbine spacing causes each turbine to be located at identical swell phase during the simulation, the flow statistical around each turbine presented in the next section are still expected to be representative. Nevertheless, cautions should still be taken in case if one need to obtain statistics of the overall performance of the entire wind turbine array when the current artificial "phase synchronization" configuration is used for the simulations.

## 4.3 Results

### 4.3.1 Phase Average Statistics of the Wind Turbulence

Because swell waves have well-organized long-crest shape and can induce strong distortion to the wind field near the wave surface, in this study we apply the phase average method to quantify the statistics of the turbulent flows and identify their correlation with the swell wave phase. For an instantaneous physical quantity resolved by LES, $\widetilde{f}$, its ensemble average at swell phase $\theta_l$ is obtained as

$$\langle f \rangle_0(x, y, z; \theta_l) = \frac{1}{N_t} \sum_{n=1}^{N_t} \widetilde{f}(x, y, z, t_n; \theta_l) \ , \tag{4.17}$$

where $t_n$ is the $n$-th sampling time and $N_t$ is the total number of sampled snapshots of the flow field for phase averaging. In Eq. (4.17) each sample is taken at an instant time $t_n$ when the swell reaches the wind turbine at its wave phase $\theta_l$. Because we configure the simulations to have an equal spacing of 3 swell wavelengths between each turbine row, we can further average the ensemble average $\langle f \rangle_0$ among each turbine to get the final phase averaged quantity

$$\langle f \rangle(x, y, z; \theta_l) = \frac{1}{N_r N_c} \sum_{n_r=0}^{N_r-1} \sum_{n_c=0}^{N_c-1} \langle f \rangle_0(x + n_r L_x / N_r, y + n_c L_y / N_c, z; \theta_l) \ , \tag{4.18}$$

where $N_r$, $N_c$, $L_x$ and $L_y$ are defined at the beginning of section 4.2.3. The corresponding instantaneous swell-phase dependent fluctuation of $\widetilde{f}$ is obtained as

$$f'(x, y, z, t; \theta_l) = \widetilde{f}(x, y, z, t; \theta_l) - \langle f \rangle(x, y, z; \theta_l) \ . \tag{4.19}$$

When analyzing the current simulation results, the swell phase angle $\theta_l$ (ranging from 0 to $2\pi$ for one swell period) is obtained by performing Fourier transformation for the wave surface elevation $\eta$ from the HOSM and then taking the phase angle from the Fourier mode that corresponds to the 9 swell wave periods in the $x$-direction of the simulation domain as considered in this chapter. Hereinafter in this chapter, we refer to the phase when the swell trough reaches the turbine as the Phase-1, the forward slope as the Phase-2, the crest as Phase-3 and the backward slope as Phase-4. As the swell waves propagate in the downwind direction, these four wave phases reaches the

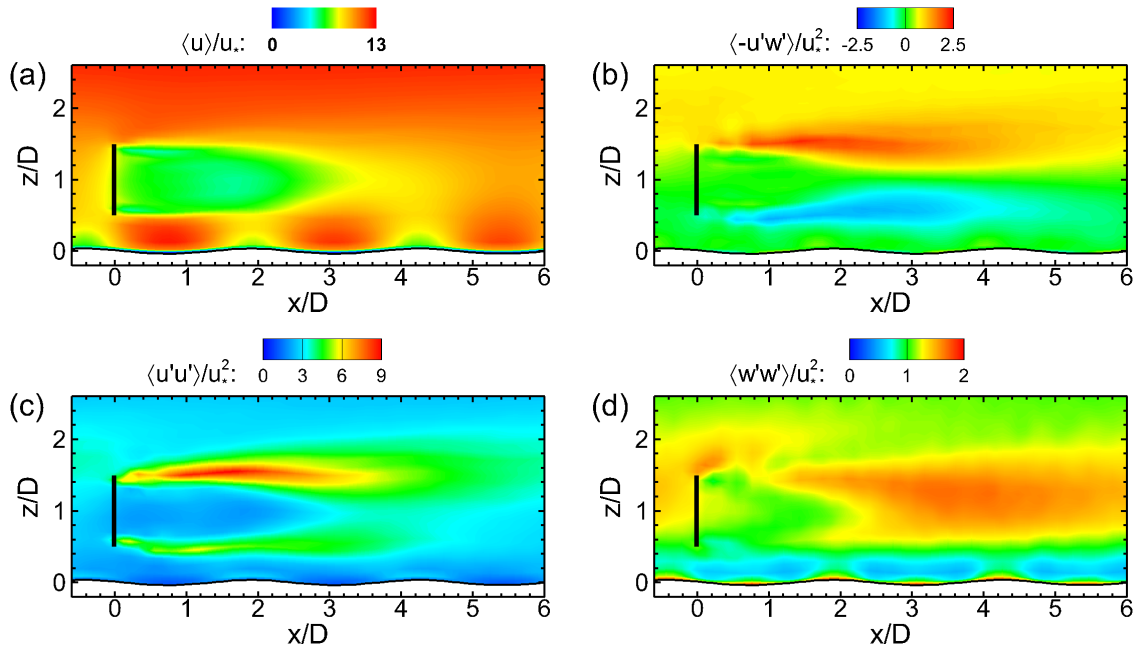


Figure 4.3: Statistics of turbulent wind flows for the fixed turbine case. The statistics for Phase-2 are plotted: (a) streamwise velocity $\langle u \rangle$; (b) Reynolds stress $\langle -u'w' \rangle$; (c) streamwise velocity variance $\langle u'u' \rangle$; and (d) vertical velocity variance $\langle w'w' \rangle$.

turbine consecutively. In this chapter, we present the statistical results obtained from the swell-phase average by showing these four representative phases.

Figure 4.3 shows the phase-averaged turbulent flow statistics at Phase-2 for the fixed wind turbine case, where the statistics are obtained using swell-phase average approach. The statistics for Phase-2 (when the forward slope of the swell reaches the turbine) are plotted there. The statistical quantities are normalized using the wind friction velocity $u_*$. The location of the turbine rotor disk is indicated by the thick black line. For this fixed turbine case, the turbulence statistics at the other three phases (not shown due to space limit) are similar, except that the wave-correlated high wind speed and low vertical velocity variance regions above the swell trough (Fig. 4.3a and 4.3d) shift according to the swell phase. A noticeable swell effect is the high wind speed above the swell wave trough [146], which can cause periodic oscillation of the wind power [173].

Figures 4.4–4.7 show the phase average statistics of the wind turbulence in the floating turbine case. Due to the pitch motion of the turbine associated with the strong swell waves, the turbine rotor disk plane flaps back and forth periodically. The turbine rotor thus experiences considerable

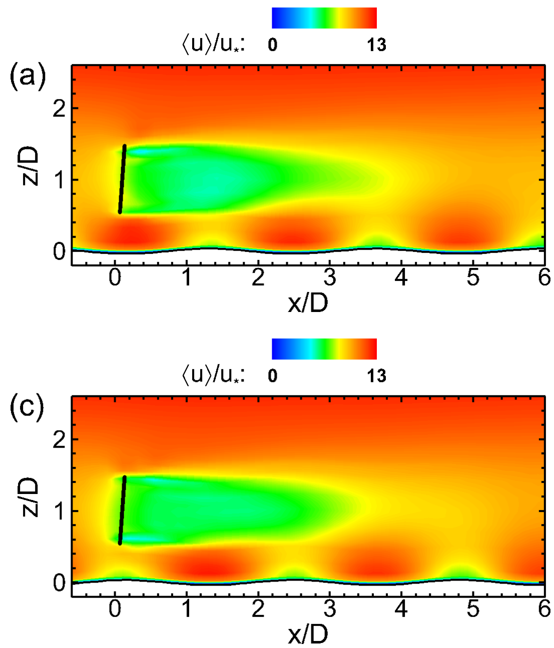


Figure 4.4: Swell-phase averaged streamwise wind velocity $\langle u \rangle$ at representative swell phases for pitching turbine case: (a) trough (Phase-1); (b) forward slope (Phase-2); (c) crest (Phase-3); and (d) backward slope (Phase-4). Turbine rotor disk is indicated by thick black line.

pitch-induced variation in the relative wind velocity with respect to the rotor disk in addition to the swell-induced wind velocity variation near the wave surface as also observed in the fixed turbine case (Fig. 4.4). For the vertical velocity field (Fig. 4.5), swell waves induce strong disturbance to the wind field near the wave surface, causing upward wind motion on the forward slope of the swell crest and downward wind motion on the backward slope. The pitch motion of the turbine generates periodic oscillation of the vertical wind velocity around the upper edge of the rotor disk.

The turbine pitch motion not only causes oscillation in the mean velocity field, but also affects the statistics of the turbulence fluctuations. Figures 4.6 and 4.7 show the streamwise velocity variance $\langle u'u' \rangle$ and vertical velocity variance $\langle w'w' \rangle$, respectively. In the statistical analysis, these quatities are calculated by first calculating the phase averages $\langle u \rangle$ and $\langle w \rangle$ at the desired swell phase according to Eq. (4.17), then obtaining the fluctuations $u'$ and $w'$ according to Eq. (4.19), and finally applying phase average to $u'u'$ and $w'w'$. The streamwise variance $\langle u'u' \rangle$ in Fig. 4.6 exhibits some variations near the upper edge of the turbine rotor that are correlated with the turbine pitch motion, but overall the magnitude and spatial distributution of $\langle u'u' \rangle$ appear to be similar to the

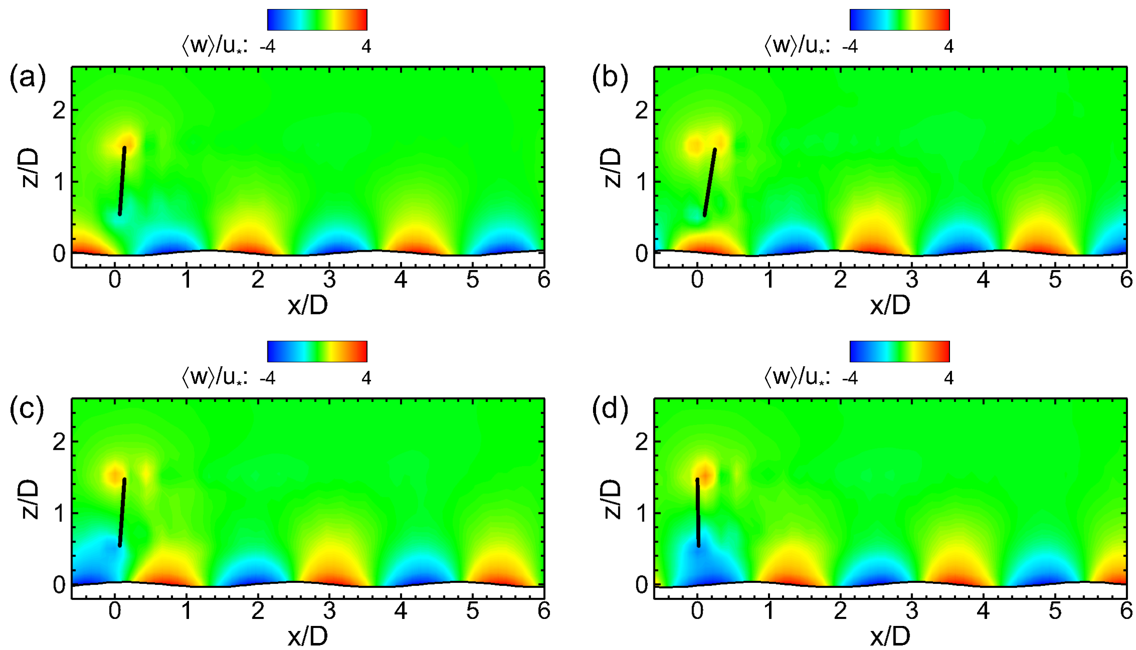


Figure 4.5: Swell-phase averaged vertical wind velocity $\langle w \rangle$ at representative swell phases for pitching turbine case: (a) trough (Phase-1); (b) forward slope (Phase-2); (c) crest (Phase-3); and (d) backward slope (Phase-4). Turbine rotor disk is indicated by thick black line.

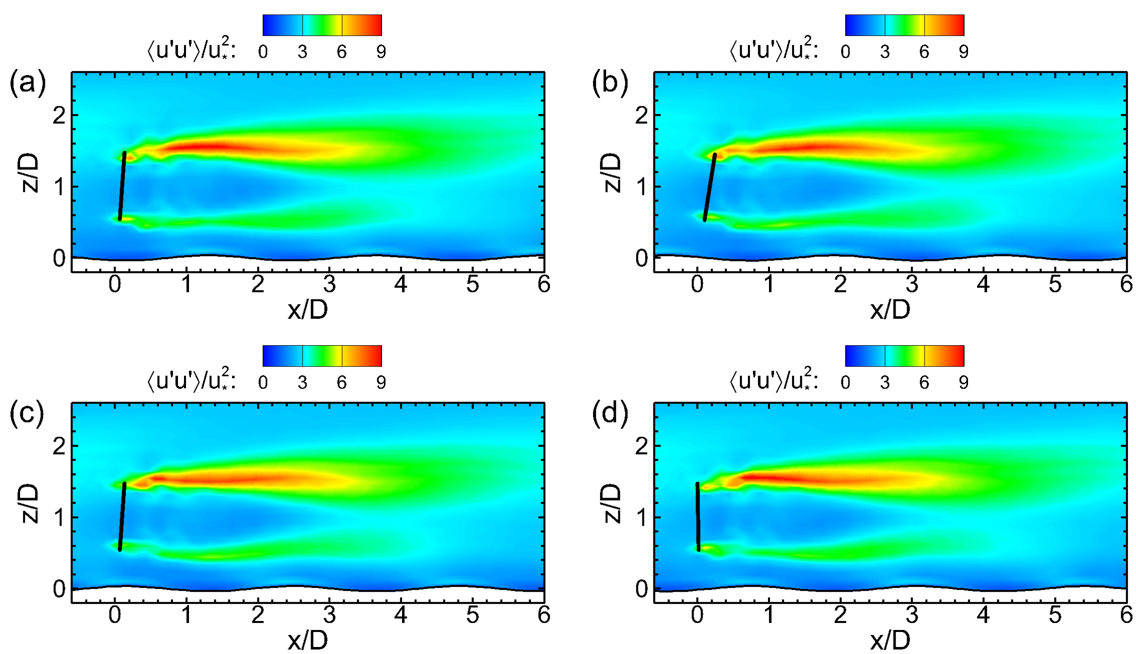


Figure 4.6: Swell-phase averaged streamwise wind velocity variance $\langle u'u' \rangle$ at representative swell phases for pitching turbine case: (a) trough (Phase-1); (b) forward slope (Phase-2); (c) crest (Phase-3); and (d) backward slope (Phase-4).

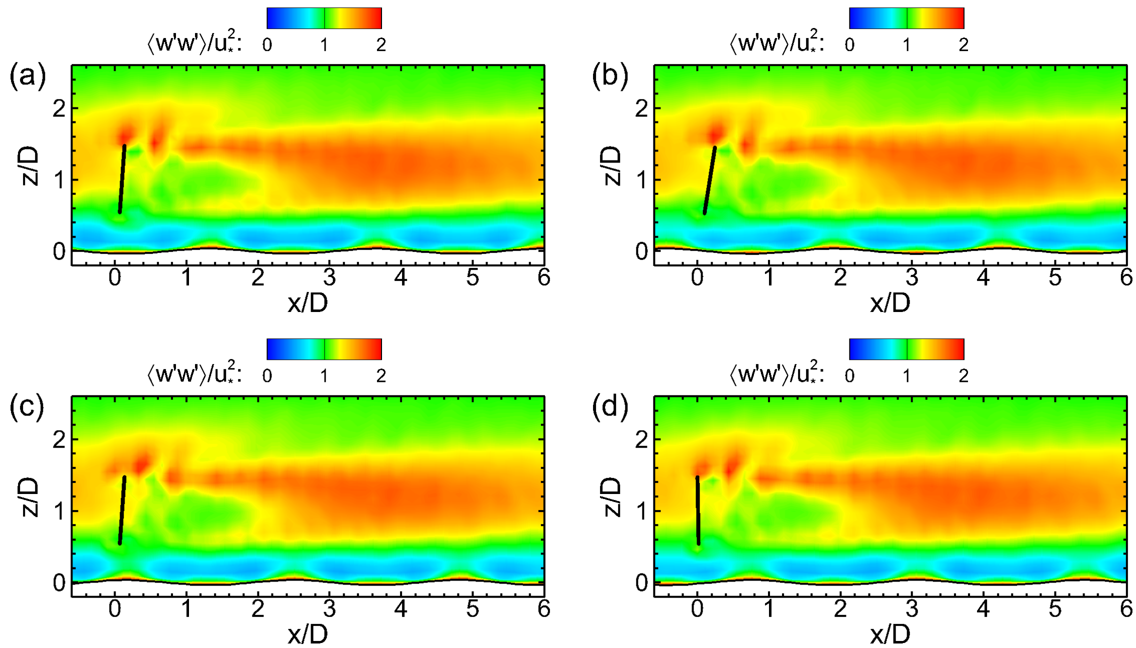


Figure 4.7: Swell-phase averaged vertical wind velocity variance $\langle w'w' \rangle$ at representative swell phases for pitching turbine case: (a) trough (Phase-1); (b) forward slope (Phase-2); (c) crest (Phase-3); and (d) backward slope (Phase-4).

result for the fixed turbine case (Fig. 4.3c). On the other hand, the vertical velocity variance $\langle w'w' \rangle$ (Fig. 4.7) and the Reynolds stress $\langle -u'w' \rangle$ (Fig. 4.8) exhibit more obvious effects caused by the turbine pitch motion. They both show apparent phase-correlated variations around and in the near wake of the upper edge of the turbine rotor disk. The comparison between Fig. 4.7 and Fig. 4.3(d) also indicates that the swell-induced turbine pitch motion increases the magnitude of $\langle w'w' \rangle$ by $\sim 15\%$ near the rotor disk and by $\sim 5\%$ in the wake flow further downstream.

### 4.3.2 Wind power extraction rate

Based on the actuator disk model, the total thrust force induced by a wind turbine can be written as [18]

$$F_t = -\frac{1}{2}\rho_a \frac{C_T}{(1-a)^2} \langle u_T \rangle_d^2 \frac{\pi}{4} D^2 \,, \tag{4.20}$$

where $\langle u_T \rangle_d$ is the disk averaged reference wind velocity that includes the contribution from both the incoming wind and the pitch motion of the turbine rotor. Following [18], the wind power

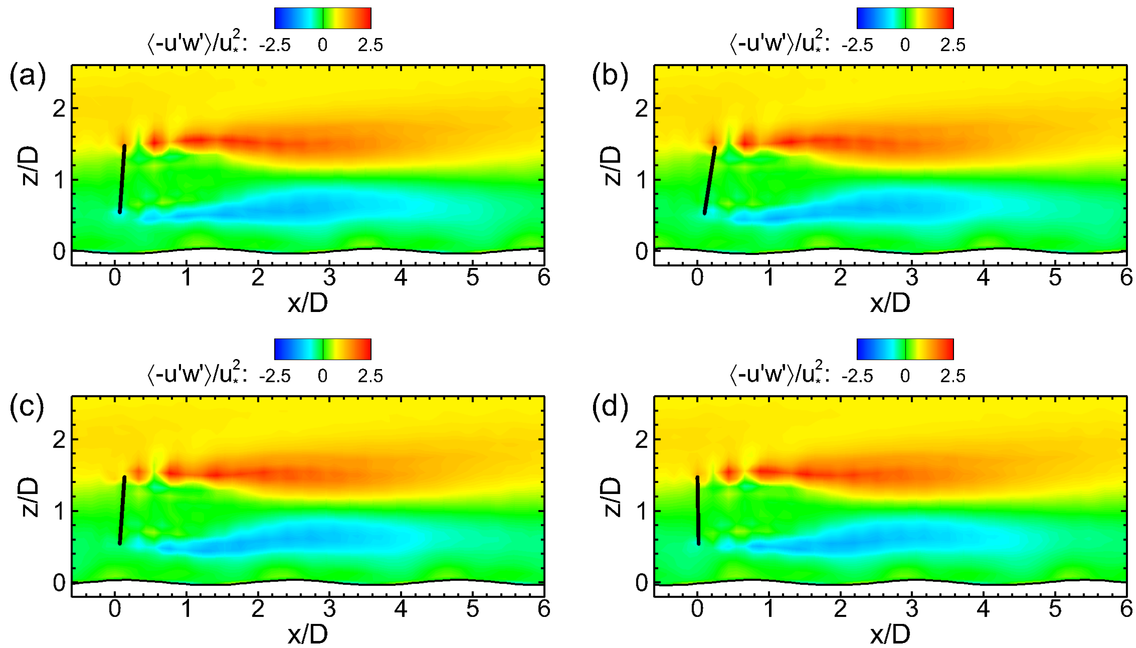


Figure 4.8: Swell-phase averaged Reynolds stress $\langle -u'w' \rangle$ at representative swell phases for the pitching turbine case: (a) trough (Phase-1); (b) forward slope (Phase-2); (c) crest (Phase-3); and (d) backward slope (Phase-4). Turbine rotor disk is indicated by thick black line.

density extracted by an individual wind turbine can then be obtained based on

$$P_{m,n} = -\frac{(F_t \langle u_T \rangle_d)_{m,n}}{\rho_a s_x s_y D^2} = \frac{1}{s_x s_y} \left( \frac{\pi C_T \langle u_T \rangle_d^3}{8(1-a)^2} \right)_{m,n} , \tag{4.21}$$

where the subscript '$(m, n)$' refers to the turbine located at the $m$-th row and $n$-th column. Because the turbines simulated in this study experience the same swell phase due to the simulation setup explained in section 4.2.3, we further average the extracted wind power density among different turbines without losing the swell phase dependence, which gives

$$P_T = \frac{1}{N_\mathrm{r} N_\mathrm{c}} \sum_{m=1}^{N_\mathrm{r}} \sum_{n=1}^{N_\mathrm{c}} P_{m,n} . \tag{4.22}$$

Figure 4.9 shows the time series of $P_T$ for the fixed and floating turbine cases by sampling $P_T$ with a time interval of $T_{sw}/10$. Here, The power density is normalized by the wind friction velocity $u_*$ and the time $t$ is normalized by the swell wave period $T_\mathrm{sw}$. The solid line is for $P_T$ and the dashed line is used to indicate the phase of the swell. For illustration purpose, the amplitude of

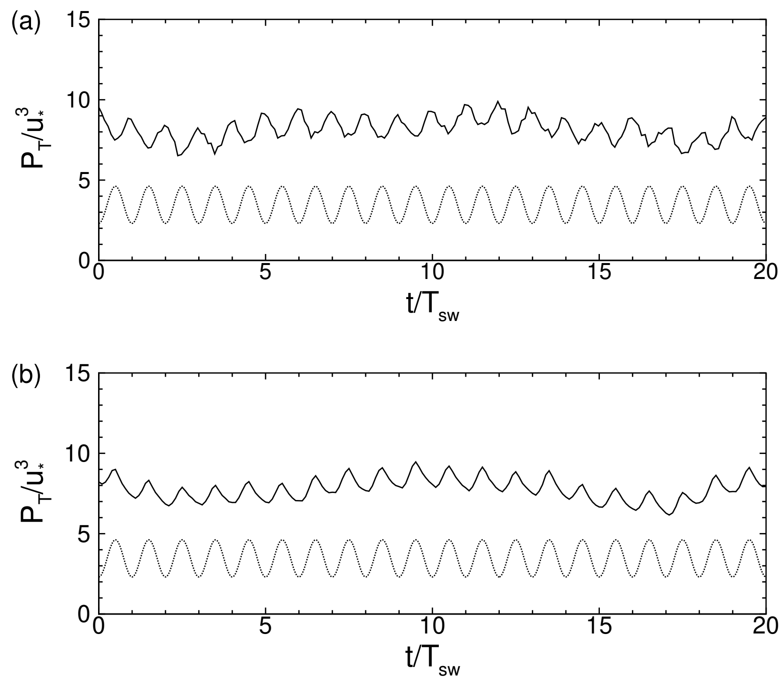


Figure 4.9: Time series of the averaged extracted power density $P_T$ of the offshore wind farm for (a) fixed turbine and (b) floating turbine in swell wave condition.

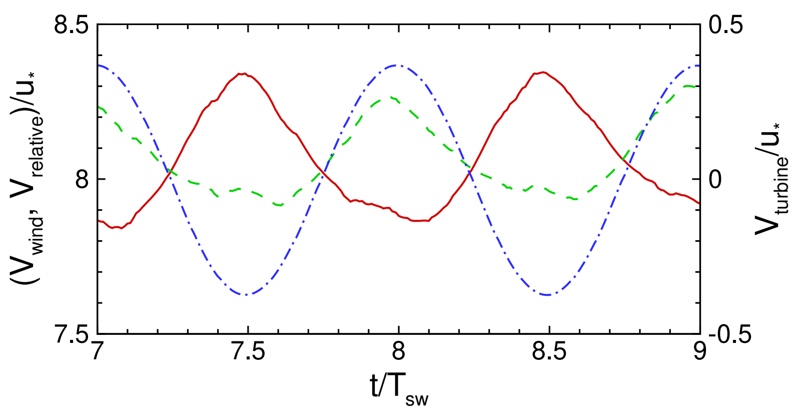


Figure 4.10: Time series of the turbine rotor disk averaged velocity components for the floating turbine case.

the swell is not plotted to scale. In both cases, $P_T$ exhibits considerable oscillation correlated with the swell wave phase. In the fixed turbine case (Fig. 4.9a), the oscillation of $P_T$ is mainly due to the low-level jet (i.e., high-speed wind near the wave surface) in the streamwise wind velocity above the swell wave trough (Fig. 4.3a) [173]. Due to the phase of this low-level jet, in the fixed turbine case $P_T$ oscillates to its maximum when the swell trough arrives and reaches its minimum when the crest arrives (Fig. 4.9a). When swell-induced turbine pitch motion is included, $P_T$ still exhibits clear swell phase dependent oscillation, but the phase angle is shifted by nearly 180 degrees. As show in Fig. 4.9(b), in the floating turbine case $P_T$ reaches maximum when the swell crest arrives and reaches minimum when the trough arrives, which is opposite to that in the fixed turbine case.

To help understand the change of the phase in the oscillating mode of $P_T$, we decompose the disk averaged reference wind velocity $\langle u_T \rangle_d = \langle u_{wind} \rangle_d - \langle u_{turbine} \rangle_d$, where $\langle u_{wind} \rangle_d$ is the disk averaged incoming wind velocity and $\langle u_{turbine} \rangle_d$ is the disk averaged velocity of the turbine pitch motion, where $\langle u_{turbine} \rangle_d > 0$ when the turbine disk flaps toward the downwind direction (e.g., from Phase-4 in Fig. 4.4(d) to Phase-1 in Fig. 4.4(a), and then to Phase-2 in Fig. 4.4(b)). Figure 4.3.2 shows the time series of these three velocities, where $V_{\text{wind}}$ is the averaged incoming wind velocity (dashed line), $V_{\text{turbine}}$ is the turbine rotor velocity caused by the swell-induced pitch motion (dash-dot line), and $V_{\text{relative}} = V_{\text{wind}} - V_{\text{turbine}}$ (solid line). The values for $V_{\text{relative}}$ and $V_{\text{wind}}$ are shown on the vertical axis plotted on the left side (ranging from 7.5 to 8.5, and the values for $V_{\text{turbine}}$ are shown on the vertical axis plotted on the right side (ranging from $-0.5$ to 0.5). . While $\langle u_{wind} \rangle_d$ is maximum above the trough (e.g., at $t/T_{sw} = 8$ in Fig. 4.3.2), the turbine rotor disk also flaps toward the downwind direction at its maximum speed. The combined effect results in a reversed phase in $\langle u_T \rangle_d$ with respect to $\langle u_{wind} \rangle_d$ for the pitch motion magnitude considered in this chapter. We note that for other types of floating platforms that have different phase dependence for their floating motions with respect to the swell waves, the resultant oscillation of the turbine power extraction rate may have swell-correlated oscillation with different magnitude and phase dependence compared to the case considered in this chapter. Nevertheless, the results reported in this study illustrate a possible scenario for which the turbine pitch motion induces noticeable effect to the power extraction rate. Because $P_T$ is directly related to the turbine force $F_t$, the results shown in this study also suggest that it may be important to take into account the swell-phase correlated wind load oscillation together with the swell-induced pitch motion when performing structure analysis and applying control algorithm for offshore floating wind turbines [e.g., 63, 80].

## 4.4 Conclusions

Offshore wind turbines deployed in deep-water region are usually designed to be installed on floating platforms. Under strong wave and wind forcing conditions, the platform can exhibit considerable oscillating motions that can affect the wind turbine performance and structure dynamics. In this chapter, we performed numerical experiments and statistical analysis to study the effect of swell wave-induced turbine pitch motion on the statistics of the wind turbulence around the turbine and the wind power extraction rate. We considered a sea-surface wave field consisting of a background broadband wind-wave field and a strong swell wave train with $O(200)$ m wavelength and 0.1 steepness propagating in the downwind direction. To study the effects of turbine pitch motion on the wake turbulence statistics and the wind power extraction, we considered a reference case with fixed wind turbines and a floating turbine case in which the swell-induced turbine pitch motion is considered. Because the motions of the turbine platform can be affected by many factors such as wind, waves, tides, ocean currents, platform geometry and mooring system, the actual turbine motions in real offshore operational environments are highly complicated. Modeling the turbine platform dynamics with all these factors considered is a comprehensive research topic by itself. For the sake of simplicity for both simulation and data analysis, in this study we have only considered the dominant pitch motion mode consisting of a mean pitch angle of 4 degrees due to mean wind forcing and a swell-correlated pitch with a magnitude of 5 degrees and a phase of $-81.9$ degree relative to the swell wave phase. The turbine pitch motion is prescribed in the simulation.

To capture the effect of surface waves and turbine pitch motion on the wind–turbine interaction, we employed a hybrid numerical model that couples LES of wind turbulence with HOSM of sea-surface waves. We focused on using the swell phase averaging approach to obtain flow statistics that revealed strong swell phase correlation in turbulence statistics and extracted power density by the wind turbines. For both the fixed and floating turbine cases considered in this chapter, the strong swell waves generate apparent swell-correlated variation in the turbulence statistics such as the phase-averaged wind velocities, velocity variance and Reynolds stress. Comparison between the fixed and floating turbine cases shows that the swell-induced turbine pitch motion causes noticeable oscillations of vertical velocity variance and Reynolds stress, as well as an increase in magnitude for the vertical velocity variance around the upper edge of the turbine rotor by $\sim 15\%$. The periodically occurring high-speed wind above the swell troughs results in swell-correlated oscillation in the extracted power density $P_T$ in the fixed turbine case. With the turbine pitch motion modeled in this chapter, the phase dependence of $P_T$ on the swell waves is shifted by nearly 180 degrees due to the combined effects of swell-induced wind velocity oscillation and turbine rotor disk velocity due to pitch motion.

# Bibliography


1. Aiyer, A. K., Yang, D., Chamecki, M. & Meneveau, C. "A population balance model for large eddy simulation of polydisperse droplet evolution." *J. Fluid Mech.* **878,** 700–739 (2019).
2. Alam, M. R., Liu, Y. & Yue, D. K. P. "Oblique sub- and super-harmonic Bragg resonance of surface waves by bottom ripples." *J. Fluid Mech.* **643,** 437–447 (2010).
3. Albertson, J. D. & Parlange, M. B. "Surface length scales and shear stress: Implications for land–atmosphere interaction over complex terrain." *Water Resour. Res.* **35,** 2121–2132 (1999).
4. Allaerts, D. & Meyers, J. "Boundary-layer development and gravity waves in conventionally neutral wind farms." *J. Fluid Mech.* **814,** 95–130 (2017).
5. Anderson, W. & Meneveau, C. "Dynamic roughness model for large-eddy simulation of turbulent flow over multiscale, fractal-like rough surfaces." *J. Fluid Mech.* **679,** 288–314 (2011).
6. Antonopoulos-Domis, M. "Large-eddy simulation of a passive scalar in isotropic turbulence." *J. Fluid Mech.* **104,** 55–79 (1981).
7. Asaeda, T. & Imberger, J. "Structure of bubble plumes in linearly stratified environments." *J. Fluid Mech.* **249,** 35–57 (1993).
8. Atlas, R. M. & Hazen, T. C. "Oil biodegradation and bioremediation: a tale of the two worst spills in US history." *Environ. Sci. Technol.* **45,** 6709–6715 (2011).
9. Bacosa, H. P., Erdner, D. L. & Liu, Z. "Differentiating the roles of photooxidation and biodegradation in the weathering of Light Louisiana Sweet crude oil in surface water from the Deepwater Horizon site." *Mar. Pollut. Bull.* **95(1),** 265–272 (2015).
10. Balachandar, S. & Eaton, J. K. "Turbulent dispersed multiphase flow." *Annu. Rev. Fluid Mech.* **42,** 111–133 (2010).

11. Barrera, C., Losada, I. J., Guanche, R. & Johanning, L. "The influence of wave parameter definition over floating wind platform mooring systems under severe sea states." *Ocean Eng.* **172,** 105–126 (2019).

12. Bertolotti, F. P., Herbert, T. & Spalart, P. R. "Linear and nonlinear stability of the Blasius boundary layer." *J. Fluid Mech.* **242,** 441–474 (1992).

13. Bohren, C. F. & Huffman, D. R. *Absorption and scattering of light by small particles* (John Wiley and Sons Ltd., Weinheim, 2008).

14. Bou-Zeid, E., Meneveau, C. & Parlang, M. B. "A scale-dependent Lagrangian dynamic model for large eddy simulation of complex turbulent flows." *Phys. Fluids* **17,** 025105 (2005).

15. Bou-Zeid, E., Meneveau, C. & Parlange, M. B. "A scale-dependent Lagrangian dynamic model for large eddy simulation of complex turbulent flows." *Phys. Fluids* **17,** 025105 (2005).

16. Bricaud, A., Morel, A., Babin, M., K., A. & Claustre, H. "Variations of light absorption by suspended particles with chlorophyll a concentration in oceanic (case 1) waters: Analysis and implications for bio-optical models. *J. Geophys. Res.* **103,** 31,033–31,044 (1998).

17. Bricaud, A., Morel, A. & Prieur, L. "Absorption by dissolved organic matter of the sea (yellow substance) in the UV and visible domains. *Limnol. Oceanogr.* **26,** 43–53 (1981).

18. Calaf, M., Meneveau, C. & Meyers, J. "Large eddy simulation study of fully developed wind-turbine array boundary layers." *Phys. Fluids* **22,** 015110 (2010).

19. Calaf, M., Parlange, M. & Meneveau, C. "Large eddy simulation study of scalar transport in fully developed wind-turbine array boundary layers." *Phys. Fluids* **23,** 126603 (2011).

20. Camilli, R., Reddy, C. M., Yoerger, D. R., Van Mooy, B. A. S., Jakuba, M. V., Kinsey, J. C., Mclntyre, C. P., Sylva, S. P. & Maloney, J. V. "Tracking hydrocarbon plume transport and biodegradation at Deepwater Horizon." *Science* **330,** 201–204 (2010).

21. Carder, K. L., Stewart, R. G., Harvey, G. R. & Ortner, P. B. "Marine humic and fulvic acids: their effects on remote sensing of ocean chlorophyll." *Limnol. Oceanogr.* **34,** 68–81 (1989).

22. Chamecki, M. & Meneveau, C. "Particle boundary layer above and downstream of an area source: scaling, simulations, and pollen transport." *J. Fluid Mech.* **683,** 1–26 (2011).

23. Chamecki, M., Meneveau, C. & Parlange, M. B. "A hybrid spectral/finite-volume algorithm for large-eddy simulation of scalars in the atmospheric boundary layer." *Boundary-Layer Meteor.* **128,** 473–484 (2008).

24. Chamecki, M., Meneveau, C. & Parlange, M. B. "Large eddy simulation of pollen transport in the atmospheric boundary layer." *J. Aerosol Sci.* **40,** 241–255 (2009).

25. Chen, B., Yang, D., Meneveau, C. & Chamecki, M. "Effects of swell on transport and dispersion of oil plumes within the ocean mixed layer." *J. Geophys. Res. Oceans* **121,** 3564–3578 (2016).

26. Chen, B., Yang, D., Meneveau, C. & Chamecki, M. "Numerical study of the effects of chemical dispersant on oil transport from an idealized underwater blowout." *Phys. Rev. Fluids* **3,** 064501 (2018).

27. Chester, S. & Meneveau, C. "Renormalized numerical simulation of flow over planar and non-planar fractal trees." *Environ. Fluid Mech.* **7,** 289–301 (2007).

28. Chester, S., Meneveau, C. & Parlange, M. B. "Modeling turbulent flow over fractal trees with renormalized numerical simulation." *J. Comput. Phys.* **225,** 427–448 (2007).

29. Chor, T., Yang, D., Meneveau, C. & Chamecki, M. "A turbulence velocity scale for predicting the fate of buoyant materials in the oceanic mixed layer." *Geophys. Res. Lett.* **45,** 11,817–11,826 (2018).

30. Chor, T., Yang, D., Meneveau, C. & Chamecki, M. "Preferential concentration of noninertial buoyant particles in the ocean mixed layer under free convection." *Phys. Rev. Fluids* **3,** 064501 (2018).

31. Chu, S. & Prosperetti, A. "Bubble plumes in a stratified environment: Source parameters, scaling, intrusion height, and neutral height." *Phys. Rev. Fluids* **2** (2017).

32. Clift, R., Grace, J. & Weber, M. E. *Bubbles, Drops, and Particles* (Dover, New York, 1978).

33. Craik, A. D. D. & Leibovich, S. "A rational model for Langmuir circulations." *J. Fluid Mech.* **73,** 401–426 (1976).

34. D'Asaro, E. A. "Turbulence in the upper-ocean mixed layer." *Annu. Rev. Mar. Sci.* **6,** 101–115 (2014).

35. Deen, N. G., Solberg, T. & Hjertager, B. H. "Large eddy simulation of the gas–liquid flow in a square cross-sectioned bubble column." *Chem. Eng. Sci.* **56,** 6341–6349 (2001).

36. Dhotre, M. T., Deen, N. G., Niceno, B., Khan, Z. & Joshi, J. B. "Large Eddy simulation for dispersed bubbly flows: a review." *Int. J. Chem. Eng.* **2013,** 343276 (2013).

37. Dissanayake, A. L., Gros, J. & Socolofsky, S. A. "Integral models for bubble, droplet, and multiphase plume dynamics in stratification and crossflow." *Environ. Fluid Mech.* **18,** 1167–1202 (2018).

38. Dommermuth, D. G. & Yue, D. K. P. "A high-order spectral method for the study of nonlinear gravity waves." *J. Fluid Mech.* **184,** 267–288 (1987).

39. Donelan, M. A. in *Proceedings of the First International Conference on Meteorology and Air Sea Interaction of the Coastal Zone* 381–387 (American Meteorological Society, Boston, MA, 1982).

40. Donelan, M. A. & Pierson, W. J. "Radar scattering and equilibrium ranges in wind-generated waves with application to scatterometry." *J. Geophys. Res. Oceans* **92,** 4971–5029 (1987).

41. Dörenkämper, M., Witha, B., Steinfeld, G., Heinemann, D. & Kühn, M. "The impact of stable atmospheric boundary layers on wind-turbine wakes within offshore wind farms." *J. Wind Eng. Ind. Aerod.* **144,** 146–153 (2015).

42. Edson, J., Crawford, T., Crescenti, J., Farrar, T., Frew, N., Gerbi, G., Helmis, C., Hristov, T., Khelif, D., Jessup, A., Jonsson, H., Li, M., Mahrt, L., McGillis, W., Plueddemann, A., Shen, L., Skyllingstad, E., Stanton, T., Sullivan, P., Sun, J., Trowbridge, J., Vickers, D., Wang, S., Wang, Q., Weller, R., Wilkin, J., III, A. J. W., Yue, D. K. P. & Zappa, C. "The coupled boundary layers and air-sea transfer experiment in low winds." *Bull. Amer. Meteor. Soc.* **88,** 341–356 (2007).

43. Fabregat, A., Dewar, W. K., Özgökmen, T. M., Poje, A. C. & Wienders, N. "Numerical simulations of turbulent thermal, bubble and hybrid plumes." *Ocean Model.* **90,** 16–28 (2015).

44. Fabregat Tomàs, A., Poje, A. C., Özgökmen, T. M. & Dewar, W. K. "Dynamics of multiphase turbulent plumes with hybrid buoyancy sources in stratified environments." *Phys. Fluids* **28,** 095109 (2016).

45. Ferry, J. & Balachandar, S. "A fast Eulerian method for disperse two-phase flow." *Int. J. Multiphase Flow* **27,** 1199–1226 (2001).

46. Fraga, B. & Stoesser, T. "Influence of bubble size, diffuser width, and flow rate on the integral behavior of bubble plumes." *J. Geophys. Res. Oceans* **121,** 3887–3904 (2016).

47. Fraga, B., Stoesser, T., Lai, C. C. K. & Socolofsky, S. A. "A LES-based Eulerian–Lagrangian approach to predict the dynamics of bubble plumes." *Ocean Model.* **97,** 27–36 (2016).

48. Fu, Q. & Sun, W. "Mie theory for light scattering by a spherical particle in an absorbing medium." *Appl. Opt.* **40,** 1354–1361 (2001).

49. Gaskell, P. H. & Lau, A. K. C. "Curvature-compensated convective transport: SMART, a new boundedness-preservin transport algorithm." *Int. J. Numer. Methods Fluids* **8,** 617–641 (1988).

50. Gordon, H. R. "Ship perturbation of irradiance measurements at sea. 1. Monte-Carlo simulations." *Appl. Opt.* **24,** 4172–4182 (1985).

51. Goullet, A. & Choi, W. "A numerical and experimental study on the nonlinear evolution of long-crested irregular waves." *Phys. Fluids* **23,** 016601 (2011).

52. Grant, A. L. M. & Belcher, S. "Characteristics of Langmuir turbulence in the ocean mixed layer." *J. Phys. Oceanogr.* **39,** 1871–1887 (2009).

53. Haltrin, V. I. "Chlorophyll-based model of seawater optical properties." *Appl. Opt.* **38,** 6826–6832 (1999).

54. Harcourt, R. R. & D'Asaro, E. A. "Large-eddy simulation of Langmuir turbulence in pure wind seas." *J. Phys. Oceanogr.* **38,** 1542–1562 (2008).

55. Hasselmann, K., Barnett, T. P., Bouws, E., Carlson, H., Cartwright, D. E., Enke, K., Ewing, J. A., Gienapp, H., Hasselmann, D. E., Kruseman, P., Meerburg, A., Müller, P., Olbers, D. J., Richter, K., Sell, W. & Walden, H. "Measurements of wind-wave growth and swell decay during the Joint North Sea Wave Project (JONSWAP)." *Dtsch. Hydrogr. Z. Suppl.* **8,** N12 (1973).

56. Hazen, T. C., Dubinsky, E. A., DeSantis, T. Z., Andersen, G. L., Piceno, Y. M., Singh, N., Jansson, J. K., Probst, A., Borglin, S. E., Fortney, J. L., Stringfellow, W. T., Bill, M., Conrad, M. E., Tom, L. M., Chavarria, K. L., Alusi, T. R., Lamendella, R., Joyner, D. C., Spier, C., Baelum, J., Auer, M., Zemla, M. L., Chakraborty, R., Sonnenthal, E. L., Dhaeseleer, P., Holman, H. Y. N., Osman, S., Lu, Z., Nostrand, J. D. V., Deng, Y., Zhou, J. & Mason, O. U. "Deep-sea oil plume enriches indigenous oil-degrading bacteria." *Science* **330,** 204–208 (2010).

57. Hergert, W. & eds., T. W. The Mie Theory: Basics and Applications (Springer, 2012).

58. Hu, G. & Celik, I. "Eulerian–Lagrangian based large-eddy simulation of a partially aerated flat bubble column." *Chem. Eng. Sci.* **63,** 253–271 (2008).

59. Jimenez, A., Crespo, A., Migoya, E. & Garcia, J. "Advances in large-eddy simulation of a wind turbine wake." *J. Phys. Conf. Ser.* **75,** 012041 (2007).

60. Jimenez, A., Crespo, A., Migoya, E. & Garcia, J. "Large-eddy simulation of spectral coherence in a wind turbine wake." *Environ. Res. Lett.* **3,** 015004 (2008).

61. Jonasz, M. & Fournier, G. R. *Light Scattering by Particles in Water: Theoretical and Experimental Foundations* (Elsevier, 2007).

62. Jonkman, J. & Matha, D. *"A Quantitative Comparison of the Responses of Three Floating Platforms."* tech. rep. NREL/CP-500-46726 (National Renewable Energy Laboratory: Golden, CO, USA, 2010).

63. Kim, K., Kim, H., Lee, J., Kim, S. & Paek, I. "Design and performance analysis of control algorithm for a floating wind turbine on a large semi-submersible platform." *J. Phys. Conf. Ser.* **753,** 092017 (2016).

64. King, S. M., Leaf, P. A., Olson, A. C., Ray, P. Z. & Tarr, M. A. "Photolytic and photocatalytic degradation of surface oil from the Deepwater Horizon spill." *Chemosphere* **95,** 415–422 (2014).

65. Kirk, J. T. *Light and Photosynthesis in Aquatic Ecosystems, 3rd Edition* (Cambridge university press, 2011).

66. Kirk, J. T. O. "Monte Carlo procedure for simulating the penetration of light into natural waters." *Theor. Appl. Genet.* **60,** 197–214 (1981a).

67. Kirk, J. T. O. "Monte Carlo study of the nature of the underwater light field in, and the relationships between optical-properties of, turbid yellow waters." *Aust. J. Mar. Fresh Res.* **32,** 517–532 (1981b).

68. Król, T., Stelmaszewski, A. & Freda, W. "Variability in the optical properties of a crude oil–seawater emulsion." *Oceanologia* **48,** 203–211 (2006).

69. Kukulka, T., Law, K. L. & Proskurowski, G. "Evidence for the influence of surface heat fluxes on turbulent mixing of microplastic marine debris." *J. Phys. Oceanogr.* **46,** 809–815 (2016).

70. Kukulka, T., Plueddemann, A. J., Trowbridge, J. H. & Sullivan, P. P. "Rapid mixed layer deepening by the combination of Langmuir and shear instabilities: a case study." *J. Phys. Oceanogr.* **40,** 2381–2400 (2010).

71. Kukulka, T., Plueddemann, A. J., Trowbridge, J. H. & Sullivan, P. P. "Significance of Langmuir circulation in upper ocean mixing: Comparison of observations and simulations." *Geophys. Res. Lett.* **36,** L10603 (2009).

72. Kumar, V., Kleissl, J., Meneveau, C. & Parlange, M. "Large-eddy simulation of a diurnal cycle in the turbulent atmospheric boundary layer: Atmospheric stability and scaling issue." *Water Resour. Res.* **42,** W06D09 (2006).

73. Kumar, V., Kleissl, J., Meneveau, C. & Parlange, M. B. "Large-eddy simulation of a diurnal cycle of the atmospheric boundary layer: Atmospheric stability and scaling issues." *Water Resour. Res.* **42,** W06D09 (2006).

74. Kumar, V., Svensson, G., Holtslag, A. A. M., Meneveau, C. & Parlange, M. "Impact of surface flux formulations and geostrophic forcing on large-eddy simulations of diurnal atmospheric boundary layer flow." *J. Appl. Meteorol. Climatol.* **49,** 1496–1516 (2010).

75. Lai, C. C. K. & Socolofsky, S. A. "The turbulent kinetic energy budget in a bubble plume." *J. Fluid Mech.* **865,** 993–1041 (2019).

76. Lay, C. R., Morris, J. M., Takeshita, R., Forth, H. P., Travers, C. L., Roberts, A. P., Alloy, M., Garner, T. R. & Bridges, K. *"Incident ultraviolet (UV) radiation and extinction coefficients in the northern Gulf of Mexico during the Deepwater Horizon oil spill."* tech. rep. (TOX_TR.06) (DWH Toxicity NRDA Technical Working Group Report, Boulder, CO., 2015).

77. Leathers, R. A., Downes, T. V., Davis, C. O. & Mobley, C. D. *"Monte Carlo radiative transfer simulations for ocean optics: A practical guide."* tech. rep. Tech. Rep. NRL/MR/5660–04-8819 (Naval Research Laboratory, 2004).

78. Leibovich, S. "The form and dynamics of Langmuir circulation." *Annu. Rev. Fluid Mech.* **15,** 391–427 (1983).

79. Lemckert, C. J. & Imberger, J. "Energetic bubble plumes in arbitrary stratification." *J. Hydraul. Eng.* **119,** 680–703 (1993).

80. Lemmer, F., Schlipf, D. & Cheng, P. "Control design methods for floating wind turbines for optimal disturbance rejection." *J. Phys. Conf. Ser.* **753,** 092006 (2016).

81. Li, M., Garrett, C. & Skyllingstad, E. "A regime diagram for classifying turbulent large eddies in the upper ocean." *Deep-Sea Res.* **I 52,** 259–278 (2005).

82. Li, Q. & Fox-Kemper, B. "Assessing the effects of Langmuir turbulence on the entrainment buoyancy flux in the ocean surface boundary layer." *J. Phys. Oceanogr.* **47,** 2863–2886 (2017).

83. Li, Y., Liu, L., Zhu, Q., Guo, Y., Hu, Z. & Tang, Y. "Influence of vortex induced loads on the motion of SPAR-Type wind turbine: a coupled aero-hydro-vortex-mooring investigation." *J. Offshore Mech. Arct. Eng.* **140,** 051903 (2018).

84. Li, Y., Tang, Y., Zhu, Q. & Liu, L. "Study on dynamic response of floating offshore wind turbine based on stretching-bending-torsion coupled nonlinear mooring loads." *Eng. Mech.* **35,** 229–239 (2018).

85. Li, Z., Spaulding, M., McCay, D. F., Crowley, D. & Payne, J. R. "Development of a unified oil droplet size distribution model with application to surface breaking waves and subsea blowout releases considering dispersant effects." *Mar. Pollut. Bull.* **114,** 247–257 (2017).

86. Lilly, D. K. *"The representation of small-scale turbulence in numerical simulation experiments."* in *Proc IBM Scientific Computing Symposium on Environmental Science* (1967), 195–210.

87. Lyu, P., Park, S. G., Shen, L. & Li, H. in *Proceedings of the ASME 2018 1st International Offshore Wind Technical Conference* IOWTC2018–1046 (San Francisco. CA. USA. November 4-7. 2018, 2018).

88. Mason, P. "Large-eddy simulation of the convective atmospheric boundary layer." *J. Atmos. Sci.* **46,** 1492–1516 (1989).

89. Mason, P. J. "Large-eddy simulation of the convective atmospheric boundary layer." *J. Atmos. Sci.* **46,** 1492–1516 (1989).

90. McWilliams, J. C. & Restrepo, J. M. "The wave-driven ocean circulation." *J. Phys. Oceanogr.* **29,** 2523–2540 (1999).

91. McWilliams, J. C. & Sullivan, P. P. "Vertical mixing by Langmuir circulation." *Spill Sci. Technol. Bull.* **6(3–4),** 225–237 (225–237).

92. McWilliams, J. C., Sullivan, P. P. & Moeng, C.-H. "Langmuir turbulence in the ocean." *J. Fluid Mech.* **334,** 1–30 (1997).

93. Mei, C. C., Stiassnie, M. & Yue, D. K. P. *Theory and Applications of Ocean Surface Waves. Part 2: Nonlinear Aspects* (World Scientific, 2005).

94. Meneveau, C. & Katz, J. "Scale-invariance and turbulence models for large-eddy simulation." *Annu. Rev. Fluid Mech.* **32,** 1–32 (2000).

95. Mensa, J. A., Özgökmen, T. M., Poje, A. C. & Imberger, J. "Material transport in a convective surface mixed layer under weak wind forcing." *Ocean Model.* **96,** 226–242 (2015).

96. Meyers, J. & Meneveau, C. "Large eddy simulation of large wind-turbine arrays in the atmospheric boundary layer." *AIAA,* 2010–827 (2010).

97. Mie, G. "Beiträge zur Optik trüber Medien, speziell kolloidaler Metallüsungen." *Annalen der Physik* **330,** 377–445 (1908).

98. Mobley, C. D. *Light and water: radiative transfer in natural waters* (Academic press, 1994).

99. Moeng, C.-H. "A large-eddy-simulation model for the study of planetary boundary-layer turbulence." *J. Atmos. Sci.* **41,** 2052–2062 (1984).

100. Morel, A. & Maritorena, S. "Bio-optical properties of oceanic waters: a reappraisal." *J. Geophys. Res.* **106,** 7163–7180 (2001).

101. Murphy, D. W., Xue, X., Sampath, K. & Katz, J. "Crude oil jets in crossflow: effects of dispersant concentration on plume behavior." *J. Geophys. Res. Oceans* **121,** 4264–4281 (2016).

102. Naderi, S., Parvanehmasiha, S. & Torabi, F. "Modeling of horizontal axis wind turbine wakes in Horns Rev offshore wind farm using an improved actuator disc model coupled with computational fluid dynamic." *Energy Convers. Manag.* **171,** 953–968 (2018).

103. Noh, Y., Kang, I. S., Herold, M. & Raasch, S. "Large eddy simulation of particle settling in the ocean mixed layer." *Phys. Fluids* **18,** 085109 (2006).

104. Otremba, Z. "Oil droplets as light absorbents in seawate."r. *Optics Express* **15,** 8592–8597 (2007).

105. Otremba, Z. & Król, T. "Modeling of the crude oil suspension impact on inherent optical parameters of coastal seawater." *Pol. J. Environ. Stud.* **11,** 407–411 (2002).

106. Otremba, Z. & Piskozub, J. "Phase functions of oil-in-water emulsions." *Optica Applicata* **XXXIV,** 93–99 (2004).

107. Özgökmen, T. M., Poje, A. C., Fischer, P. F., Childs, H., Krishnan, H., Garth, C., Haza, A. C. & Ryan, E. "On multi-scale dispersion under the influence of surface mixed layer instabilities and deep flows." *Ocean Modell.* **56,** 16–30 (2012).

108. Özgökmen, T. M., Poje, A. C., Fischer, P. F. & Haza, A. C. "Large eddy simulations of mixed layer instabilities and sampling strategies." *Ocean Modell.* **39,** 311–331 (2011).

109. Pan, Y., Chamecki, M. & Isard, S. A. "Dispersion of heavy particles emitted from area sources in the unstable atmospheric boundary layer." *Boundary-Layer Meteor.* **146,** 235–256 (2013).

110. Pan, Y., Chamecki, M. & Isard, S. A. "Large-eddy simulation of turbulence and particle dispersion inside the canopy roughness sublayer." *J. Fluid Mech.* **753,** 499–534 (2014).

111. Pegau, W. S., Gray, D. & Zaneveld, J. R. V. "Absorption and attenuation of visible and near-infrared light in water: dependence on temperature and salinity." *Appl. Opt.* **36,** 6035–6046 (1997).

112. Peng, C., Xiao, S. & Yang, D. "Large-eddy simulation model for the effect of gas bubble dissolution on the dynamics of hydrocarbon plume from deep-water blowout." *J. Geophys. Res. Oceans* **125** (2020).

113. Petzold, T. J. *"Volume scattering functions for selected ocean waters."* tech. rep. Tech. Rep. (Scripps Institution of Oceanography (Naval Air Development Center), 1972).

114. Plass, G. N. & Kattawar, G. W. "Monte Carlo calculations of radiative transfer in the Earth's atmosphere–ocean system: I. Flux in the atmosphere and ocean." *J. Phys. Oceanogr.* **8,** 139–145 (1972).

115. Polton, J. A., Smith, J. A., MacKinnon, J. A. & Tejada-Martinez, A. E. "Rapid generation of high-frequency internal waves beneath a wind and wave forced oceanic surface mixed layer." *Geophys. Res. Lett.* **35,** L13602 (2008).

116. Radović, J. R., Aeppli, C., Nelson, R. K., Jimenez, N., Reddy, C. M., Bayona, J. M. & Albaigés, J. "Assessment of photochemical processes in marine oil spill fingerprinting." *Mar. Pollut. Bull.* **79(1–2),** 268–277 (2014).

117. Ray, P. Z., Chen, H., Podgorski, D. C., McKenna, A. M. & Tarr, M. A. "Sunlight creates oxygenated species in water-soluble fractions of Deepwater Horizon oil." *J. Hazard. Mater.* **280,** 636–643 (2014).

118. Rockel, S., Camp, E., Schmidt, J., Peinke, J., Cal, R. B. & Hölling, M. "Experimental study on influence of pitch motion on the wake of a floating wind turbine model." *Energies* **7,** 1954–1985 (2014).

119. Rockel, S., Peinke, J., Hölling, M. & Cal, R. B. "Wake to wake interaction of floating wind turbine models in free pitch motion: An eddy viscosity and mixing length approach." *Renew. Energ.* **85,** 666–676 (2016).

120. Roddier, D., Cermelli, C., Aubault, A. & Weinstein, A. "WindFloat: A floating foundation for offshore wind turbines." *J. Renew. Sustain. Energy* **2,** 033104 (2010).

121. Römer, M., Sahling, H., Pape, T., Bohrmann, G. & Spiess, V. "Quantification of gas bubble emissions from submarine hydrocarbon seeps at the Makran continental margin (offshore Pakistan)." *J. Geophys. Res.* **117,** C10015 (2012).

122. Rudź, K., Darecki, M. & Toczek, H. "Modelling the influence of oil content on optical properties of seawater in the Baltic Sea." *J. Europ. Opt. Soc. Rap. Public.* **8,** 13063 (2013).

123. Schladow, S. G. "Lake destratification by bubble-plume systems: Design methodology." *J. Hydraul. Eng.* **119,** 350–368 (1993).

124. Schlatter, P., Adams, N. & Kleiser, L. "A windowing method for periodic inflow/outflow boundary treatment of non-periodic flows." *J. Comput. Phys.* **206,** 505–535 (2005).

125. Seol, D.-G., Bryant, D. B. & Socolofsky, S. A. "Measurement of behavioral properties of entrained ambient water in a stratified bubble plume." *J. Hydraul. Eng.* **135,** 983–988 (2009).

126. Shoele, K., Prowell, I., Zhu, Q. & Elgamal, A. "Dynamic and structural modeling of a floating wind turbine." *Int. J. Offshore Polar* **21,** 155–160 (2011).

127. Skyllingstad, E. D. & Denbo, D. W. "An ocean large-eddy simulation of Langmuir circulations and convection in the surface mixed layer." *J. Geophys. Res.* **100,** 8501–8522 (1995).

128. Smagorinsky, J. "General circulation experiments with the primitive equations: I. The basic experiment." *Mon. Weather Rev.* **91,** 99–164 (1963).

129. Smith, R. C. & Baker, K. S. "Optical properties of the clearest natural waters (200–800 nm)." *Appl. Opt.* **20,** 177–184 (1981).

130. Socolofsky, S. A. & Adams, E. E. "Liquid volume fluxes in stratified multiphase plumes." *J. Hydraul. Eng.* **129,** 905–914 (2003).

131. Socolofsky, S. A. & Adams, E. E. "Multi-phase plumes in uniform and stratified crossflow." *J. Hydraul. Res.* **40,** 661–672 (2002).

132. Socolofsky, S. A., Adams, E. E., Boufadel, M. C., Aman, Z. M., Johansen, Ø., Konkel, W. J., Lindo, D., Madsen, M. N., North, E. W., Paris, C. B., Rasmussen, D., Reed, M., Rønningen, P., Sim, L. H., Uhrenholdt, T., Anderson, K. G., Cooper, C. & Nedwed, T. J. "Intercomparison of oil spill prediction models for accidental blowout scenarios with and without subsea chemical dispersant injection." *Mar. Pollut. Bull.* **96,** 110–126 (2015).

133. Socolofsky, S. A., Adams, E. E. & Sherwood, C. R. "Formation dynamics of subsurface hydrocarbon intrusions following the Deepwater Horizon blowout." *Geophys. Res. Lett.* **38,** L09602 (2011).

134. Socolofsky, S. A., Bhaumik, T. & Seol, D.-G. "Double-plume integral models for near-field mixing in multiphase plumes." *J. Hydraul. Eng.* **134,** 772–783 (2008).

135. Socolofsky, S. A., Crounse, B. C. & Adams, E. E. in *Environmental Fluid Mechanics – Theories and Applications* (eds Shen, H., Cheng, A., Wang, K.-H. & Teng, M. H.) 84–125 (ASCE/Fluids Committee, New York, 2002).

136. Socolofsky, S. A. & Adams, E. E. "Role of slip velocity in the behavior of stratified multiphase plumes." *J. Hydraul. Eng.* **131,** 273–282 (2005).

137. Solonenk, M. G. & Mobley, C. D. "Inherent optical properties of Jerlov water types." *Appl. Opt.* **54,** 5392–5401 (2015).

138. Stenvens, R. J. A. M., Gayme, D. F. & Meneveau, C. "Large eddy simulation studies of the effects of alignment and wind farm length." *J. Renew. Sustain. Energy* **6,** 023105 (2014).

139. Stenvens, R. J. A. M., Martínez-Tossas, L. A. & Meneveau, C. "Comparison of wind farm large eddy simulations using actuator disk and actuator line models with wind tunnel experiments." *Renew. Energ.* **116,** 470–478 (2018).

140. Stenvens, R. J. A. M. & Meneveau, C. "Flow structure and turbulence in wind farms." *Annu. Rev. Fluid Mech.* **49,** 311–339 (2017).

141. Stenvens, R. J. A. M. & Meneveau, C. "Temporal structure of aggregate power fluctuations in large-eddy simulations of extended wind-farms." *J. Renew. Sustain. Energy* **6,** 043102 (2014).

142. Stevens, R. J. A. M., Gayme, D. F. & Meneveau, C. "Effects of turbine spacing on the power output of extended wind-farms." *Wind Energy* **19,** 359–370 (2016).

143. Stevens, R. J. A. M., Graham, J. & Meneveau, C. "A concurrent precursor inflow method for large eddy simulations and applications to finite length wind farms." *Renew. Energy* **68,** 46–50 (2014).

144. Stramski, D., Bricaud, A. & Morel, A. "Modeling the inherent optical properties of the ocean based on the detailed composition of the planktonic community." *Appl. Opt.* **40,** 2929–2945 (2001).

145. Stramski, D. & Tegowski, J. "Effects of intermittent entrainment of air bubbles by breaking wind waves on ocean reflectance and underwater light field." *J. Geophys. Res.* **106,** 31,345–31,360 (2001).

146. Sullivan, P. P., Edson, J. B., Hristov, T. & McWilliams, J. C. "Large-eddy simulations and observations of atmospheric marine boundary layers above nonequilibrium surface waves." *J. Atmos. Sci.* **65,** 1225–1245 (2008).

147. Sullivan, P. P., McWilliams, J. C. & Moeng, C.-H. "A subgrid-scale model for large-eddy simulation of planetary boundary-layer flows." *Boundary-Layer Meteor.* **71,** 247–276 (1994).

148. Sullivan, P. P., McWilliams, J. C. & Patton, E. G. "Large-eddy simulation of marine atmospheric boundary layers above a spectrum of moving waves." *J. Atmos. Sci.* **71,** 4001–4027 (2014).

149. Sullivan, P. & McWilliams, J. C. "Dynamics of winds and currents coupled to surface waves." *Annu. Rev. Fluid Mech.* **42,** 19–42 (2010).

150. Tanaka, M. "Verification of Hasselmann's energy transfer among surface gravity waves by direct numerical simulations of primitive equations." *J. Fluid Mech.* **47,** 199–221 (1995).

151. VerHulst, C. & Meneveau, C. "Large eddy simulation study of the kinetic energy entrainment by energetic turbulent flow structures in large wind farms." *Phys. Fluids* **26,** 025113 (2014).

152. Von Deimling, J. S., Linke, P., Schmidt, M. & Rehder, G. "Ongoing methane discharge at well site 22/4b (North Sea) and discovery of a spiral vortex bubble plume motion." *Mar. Pet. Geol.* **68,** 718–730 (2015).

153. Wan, F., Porté-Agel, F. & Stoll, R. "Evaluation of dynamic subgrid-scale models in large-eddy simulations of neutral turbulent flow over a two-dimensional sinusoidal hill." *Atmos. Environ.* **41,** 2719–2728 (2007).

154. Wang, B., Socolofsky, S. A., Breier, J. A. & Seewald, J. S. "Observations of bubbles in natural seep flares at MC 118 and GC 600 using in situ quantitative imaging." *J. Geophys. Res. Oceans* **121,** 2203–2230 (2016).

155. Wang, L., Jacques, S. L. & Zheng, L. "MCML–Monte Carlo modeling of light transport in multi-layered tissues." *Comput. Methods Programs Biomed.* **47,** 131–146 (1995).

156. Wang, X. & Wang, L. V. "Propagation of polarized light in birefringent turbid media: A Monte Carlo study." *J. Biomed. Opt.* **7,** 279–290 (2002).

157. Wayman, E. N., Sclavounos, P. D., Butterfield, S., Jonkman, J. & Musial, W. *"Coupled dynamic modeling of floating wind turbine systems."* tech. rep. NREL/CP-500-39481 (National Renewable Energy Laboratory: Golden. CO. USA, 2006).

158. Webb, A. & Fox-Kemper, B. "Wave spectral moments and Stokes drift estimation." *Ocean Model.* **40,** 273–288 (2011).

159. Wen, B., Dong, X., Tian, X., Peng, Z., Zhang, W. & Wei, K. "The power performance of an offshore floating wind turbine in platform pitching motion." *Energ.* **154,** 508–521 (2018).

160. *"wind energy by 2030: Increasing wind energy's contribution to U.S. electricity supply."* tech. rep. Technical Report (U.S. Department of Energy: Washington. DC. USA, 2008).

161. *"Wind Vision: A New Era for Wind Power in the United States."* tech. rep. Technical Report (U.S. Department of Energy: Washington. DC. USA, 2015).

162. Woźniak, B. & Dera, J. *Light absorption in sea water* (Springer, 2007).

163. Woźniak, B., Dera, J., Ficek, D., Majchrowski, R., Ostrowska, M. & Kaczmarek, S. "Modelling light and photosynthesis in the marine environment." *Oceanologia* **45,** 171–245 (2003).

164. Wüest, A., Brooks, N. H. & Imboden, D. M. "Bubble plume model for lake restoration." *Water Resour. Res.* **28,** 3235–3250 (1992).

165. Xu, Z., Guo, X., Shen, L. & Yue, D. K. P. "Radiative transfer in ocean turbulence and its effect on underwater light field." *J. Geophys. Res.* **117,** C00H18 (2012).

166. Xu, Z. & Yue, D. K. P. "Monte Carlo radiative transfer simulation for the near-ocean-surface high-resolution downwelling irradiance statistics." *Opt. Eng.* **53,** 051408 (2014).

167. Xu, Z., Yue, D. K. P., Shen, L. & Voss, K. J. "Patterns and statistics of in-water polarization under conditions of linear and nonlinear ocean surface waves." *J. Geophys. Res.* **116,** C00H12 (2011).

168. Yang, D., Chamecki, M. & Meneveau, C. "Inhibition of oil plume dilution in Langmuir ocean circulation." *Geophys. Res. Lett.* **41,** 1632–1638 (2014).

169. Yang, D., Chen, B., Chamecki, M. & Meneveau, C. "Oil plumes and dispersion in Langmuir, upper-ocean turbulence: large-eddy simulations and K-profile parameterization." *J. Geophys. Res. Oceans* **120,** 4729–4759 (2015).

170. Yang, D., Chen, B., Socolofsky, S. A., Chamecki, M. & Meneveau, C. "Large-eddy simulation and parameterization of buoyant plume dynamics in stratified flow." *J. Fluid Mech.* **794,** 798–833 (2016).

171. Yang, D., Meneveau, C. & Shen, L. "Dynamic modeling of sea-surface roughness for large-eddy simulation of wind over ocean wavefield." *J. Fluid Mech.* **726,** 62–99 (2013).

172. Yang, D., Meneveau, C. & Shen, L. "Effect of downwind swells on offshore wind energy harvesting – A large-eddy simulation study." *Renewable Energy* **70,** 11–23 (2014).

173. Yang, D., Meneveau, C. & Shen, L. "Large-eddy simulation of offshore wind farm." *Phys. Fluids* **26** (2014).

174. Yang, D. & Shen, L. "Direct-simulation-based study of turbulent flow over various waving boundaries." *J. Fluid Mech.* **650,** 131–180 (2010).

175. Yang, D. & Shen, L. "Simulation of viscous flows with undulatory boundaries. Part I. Basic solver." *J. Comput. Phys.* **230,** 5488–5509 (2011a).

176. Yang, D. & Shen, L. "Simulation of viscous flows with undulatory boundaries. Part II: Coupling with other solvers for two-fluid computations." *J. Comput. Phys.* **230,** 5510–5531 (2011b).

177. Yang, X., Kang, S. & Sotiropoulos, F. "Computational study and modeling of turbine spacing effects in infinite aligned wind farms." *Phys. Fluids* **24,** 115107 (2012).

178. Yang, X. & Sotiropoulos, F. "LES investigation of infinite staggered wind-turbine arrays." *J. Phys. Conf. Ser.* **555,** 012109 (2014).

179. Yapa, P. D. & Li, Z. "Simulation of oil spills from underwater accidents I: Model development." *J. Hydraul. Res.* **35,** 673–688 (1997).

180. You, Y., Zhai, P. W., Kattawar, G. W. & Yang, P. "Polarized radiance fields under a dynamic ocean surface: a three-dimensional radiative transfer solution." *Appl. Opt.* **48,** 3019–3029 (2009).

181. Zakharov, V. E. "Stability of periodic waves of finite amplitude on the surface of a deep fluid." *J. Appl. Mech. Tech. Phys.* **2,** 190–194 (1968).

182. Zervos, A. & Kjaer, C. *"Pure Power: Wind Energy Scenarios up to 2030."* tech. rep. Technical Report (European Wind Energy Association: Brussels. Belgium., 2008).

183. Zhang, M., Arendshorst, M. G. & Stevens, R. "Large eddy simulations of the effect of vertical staggering in large wind farms." *Wind Energ.* **22,** 189–204 (2018).

184. Zhao, L., Boufadel, M. C., Adams, E., Socolofsky, S. A., King, T., Lee, K. & Nedwed, T. "Simulation of scenarios of oil droplet formation from the Deepwater horizon blowout." *Mar. Pollut. Bull.* **101,** 304–319 (2015).

185. Zhao, L., Boufadel, M. C., Socolofsky, S. A., Adams, E., King, T. & Lee, K. "Evolution of droplets in subsea oil and gas blowouts: development and validation of the numerical model VDROP-J." *J. Mar. Pollut. Bull.* **83,** 58–69 (2014).

186. Zhao, L., Gao, F., Boufadel, M. C., King, T., Robinson, B., Lee, K. & Conmy, R. "Oil jet with dispersant: macro-scale hydrodynamics and tip streaming." *AIChE J.* **63,** 5222–5234 (2017).

187. Zheng, L. & Yapa, P. D. "Buoyant velocity of spherical and nonspherical bubbles/droplets." *J. Hydraul. Eng.* **126,** 852–854 (2000).

188. Zheng, L. & Yapa, P. D. "Buoyant velocity of spherical and nonspherical bubbles/droplets." *J. Hydraul. Engng.* **126,** 852–854 (2000).

# Appendix

## Appendix A

### A.1 High-order spectral simulation of sea-surface waves

In current HOS model, the continuity equation and boundary conditions (4.12) and (4.13) are solved together based on the perturbation method and pseudo-spectral method [38]. In particular, $\Phi$ is expanded into a perturbation series with respect to wave steepness to order $M$,

$$\Phi(x,y,z,t) = \sum_{m=1}^{M} \Phi^{(m)}(x,y,z,t) \; . \tag{A.1}$$

The surface potential $\Phi^s$ can then be expressed based on the perturbation modes $\Phi^{(}m)$ using Taylor series expansion about $z = 0$,

$$\Phi^s(x,y,t) = \sum_{m=1}^{M} \sum_{\ell=0}^{M-m} \frac{\eta^\ell}{\ell!} \frac{\partial^\ell}{\partial z^\ell} \Phi^{(m)}(x,y,z,t) \bigg|_{z=0} \; . \tag{A.2}$$

Finally, $\Phi^{(m)}$ is rewritten into an eigenfunction expansion,

$$\Phi^{(m)}(x,y,z,t) = \sum_{n=1}^{N} \Phi_n^{(m)}(t) \Psi_n(x,y,z) \; , \tag{A.3}$$

where the eigenfunction $\Psi_n(x,y,z) = \exp(|\mathbf{k}(n)|z + i\mathbf{k}(n) \cdot \mathbf{x})$ under deep-water condition, $i = \sqrt{-1}$, $\mathbf{x}$ is the horizontal coordinate vector, and $\mathbf{k}(n) = (k_x(n), k_y(n))$ is the two-dimensional wavenumber vector for the $n$-th wave mode, which is related to the scalar wavenumber as $k = |\mathbf{k}| = \sqrt{k_x^2 + k_y^2}$. By substituting Eqs. (A.1)–(A.3) into (4.12) and (4.13), the evolution equations for

$\eta$ and $\Phi^s$ are obtained [38, 93],

$$\frac{\partial \eta}{\partial t} = -\widehat{\nabla}\eta \cdot \widehat{\nabla}\Phi^s + \left(1 + |\widehat{\nabla}\eta|^2\right)\left[\sum_{m=1}^{M}\sum_{\ell=0}^{M-m}\frac{\eta^\ell}{\ell!}\sum_{n=1}^{N}\Phi_n^{(m)}\frac{\partial^{\ell+1}\Psi_n}{\partial z^{\ell+1}}\bigg|_{z=0}\right] \tag{A.4}$$

and

$$\frac{\partial \Phi^s}{\partial t} = -g\eta - \frac{|\widehat{\nabla}\Phi^s|^2}{2} + \frac{1 + |\widehat{\nabla}\eta|^2}{2}\left[\sum_{m=1}^{M}\sum_{\ell=0}^{M-m}\frac{\eta^\ell}{\ell!}\sum_{n=1}^{N}\Phi_n^{(m)}\frac{\partial^{\ell+1}\Psi_n}{\partial z^{\ell+1}}\bigg|_{z=0}\right]^2. \tag{A.5}$$

In the current HOS model, Eqs. (A.4) and (A.5) are discretized using the pseudo-spectral method based on Fourier series, and integrated in time by a fourth-order Runge–Kutta scheme ([171–173, 176]).

The HOS model can capture the nonlinear wave–wave interactions and simulate an unsteady, time-resolved surface wave field. In this chapter, the HOS wave simulation is initialized based on the empirical wave spectra for equilibrium ocean wave conditions from [40] using a random phase method [173, 176]. Under the equilibrium condition, the energy input from the wind to the wave field is weak and the HOS model may be used without the expensive coupling with a wind turbulence solver that was used in [176]. As shown in [171], the current HOS model can maintain the equilibrium wave spectrum well for a considerable period of time without the dynamic coupling with the wind field for energy input. Therefore, in this study the HOS model is used in a stand-alone model to provide unsteady, time-resolved surface wave fields in spatial domain for modeling the effects of surface waves on the light refraction at the air–water interface under equilibrium wind–wave condition. Note that if a non-equilibrium wind–wave condition is to be considered, proper wind forcing should be included in the HOS model in order to capture the evolution of the wave spectrum.

We note that the study reported in this study mainly focuses on the simulations and analysis of the effects of the surface oil plumes on the underwater radiative transfer. The effects of sea-surface waves on the radiative transfer have already been studied extensively in previous studies [e.g., 166, 167], thus are not analyzed in details in this chapter. It is worth mentioning that the surface wave field may also be synthesized by simple linear superposition of Fourier modes based on the empirical wave spectra, which can save the computational cost associated with simulating the wave field. However, cautions should be taken for the potential errors associated with neglecting the wave nonlinearity effects [167]. Note that for the simulation cases reported in this chapter, the total computational cost is mostly associated with the LES modeling the oil plume dispersion in the ocean turbulence as well as the MCS modeling of the underwater radiative transfer, and the impact of the HOS wave modeling on the computational cost is small. Therefore, in this study the HOS model is adopted for providing the surface wave field condition to the MCS considering its high-order accuracy and computational efficiency.

## A.2 Modeling the inherent optical properties of oil contaminated seawater

In natural ocean condition, the seawater inherent optical properties vary with temperature $\Theta$, salinity $S$, chlorophyll concentration $C_{ch}$, optical properties and number density $N_d$ of suspended oil droplets, etc., [65, 98], inducing significant variation to the light field [165]. In the case of oil contaminated seawater, the effects of suspended crude oil droplets dominates the variation of the IOPs. In the reported simulations, the environmental parameters of natural seawater (i.e., $\Theta$, $S$, and $C_{ch}$) are prescribed based on typical ocean environments. The instantaneous local number density of crude oil droplets is given by $N_d = C/(\rho_d \pi d^3/6)$, where $C$ is the oil mass concentration obtained from the LES oil plume model, $\rho_d$ is the density of oil droplet, and $d$ is oil droplet diameter. The specific formulas used for computing the IOPs of oil-contaminated seawater are summarized below.

### A.2.1 Modeling Light Absorption and Scattering in Natural Seawater

The light absorption coefficient $a$ can be modeled as a function of temperature $\Theta$, salinity $S$, chlorophyll concentration $C_{ch}$, light wavelength $\lambda_l$, oil droplet diameter $d$ and number density $N_d$ as [16, 98, 145, 162]

$$\begin{aligned} a(\Theta, S, C_{ch}, d, N_d; \lambda_l) = {} & a_w(\Theta, S; \lambda_l) + a_{SPM}(C_{ch}; \lambda_l) \\ & + a_{CDOM}(C_{ch}; \lambda_l) + a_d(d, N_d; \lambda_l). \end{aligned} \tag{A.6}$$

Here, $a_w$ is the absorption by seawater molecules and is modeled as [61, 111]

$$a_w(\Theta, S; \lambda_l) = a_w(\Theta_r, 0; \lambda_l) + \Psi_\Theta(\Theta - \Theta_r) + \Psi_s S, \tag{A.7}$$

where $\Theta_r$ is a reference temperature, and $\Psi_\Theta$ and $\Psi_s$ are the slope coefficients for $\Theta$ and $S$, respectively. Considering a representative ocean mixed layer condition with $\Theta = 20°C$ and $S = 3.5\%$, in this study we set $a_w = 0.0145\,\mathrm{m}^{-1}$ [98]. The second term $a_{SPM}$ represents the absorption due to suspended particulate matter (SPM) covary with the chlorophyll concentration $C_{ch}$ (measured in $\mathrm{mg/m^3}$), which can be modeled either as [16, 100, 137, 144]

$$a_{SPM}(C_{ch}; \lambda_l) = B(\lambda_l) C_{ch}^{E(\lambda_l)}, \tag{A.8}$$

or as [53, 165]

$$a_{SPM}(C_{ch}; \lambda_l) = a^*_{SPM}(\lambda_l) C_{ch}^{0.602}. \tag{A.9}$$

where $B(\lambda_l)$, $E(\lambda_l)$, and $a^*_{SPM}(\lambda_l)$ are empirical coefficients. The third term $a_{CDOM}$ represents the absorption due to colored dissolved organic matter (CDOM) and can be parameterized as [17]

$$a_{CDOM}(C_{ch}; \lambda_l) = a_{CDOM}(C_{ch}; \lambda_{l,r}) \exp\left[-S_{CDOM}\left(\lambda_l - \lambda_{l,r}\right)\right], \tag{A.10}$$

where $a_{CDOM}(C_{ch}; \lambda_{l,r})$ depends on $C_{ch}$, $\lambda_{l,r}$ is a reference light wavelength, and $S_{CDOM}$ is an empirical constant [65, 137]. Alternatively, $a_{CDOM}$ can also be parameterized based on the concentrations of the first two components in CDOM (i.e., fulvic acid and humic acid) as follows [21, 53, 61, 165],

$$a_{CDOM}(C_{ch}; \lambda_l) = C_f a^*_f \exp\left(-k_f \lambda_l\right) + C_h a^*_h \exp\left(-k_h \lambda_l\right), \tag{A.11}$$

where $C_f = 1.74098 C_{ch} \exp\left(0.12327 C_{ch}\right)$ is the specific concentration of fulvic acid, $a^*_f = 35.959\,\mathrm{m^2/mg}$ is the specific absorption coefficient of fulvic acid, $k_f = 0.0189\,\mathrm{nm}^{-1}$, $C_h = 0.19334 C_{ch} \exp\left(0.12343 C_{ch}\right)$ is the specific concentration of humic acid, $a^*_h = 18.828\,\mathrm{m^2/mg}$ is the specific absorption coefficient of humic acid, and $k_h = 0.01105\,\mathrm{nm}^{-1}$ [21, 53].

In this chapter, Eqs. (A.9) and (A.11) are used to model $a_{SPM}$ and $a_{CDOM}$, respectively. The corresponding vertical distribution of chlorophyll concentration is prescribed based on [162]

$$C_{ch}(z) = C_{ch,0}\frac{C_{const} + C_m \exp[-((z + h_{max})\sigma_z)^2]}{C_{const} + C_m \exp[-(h_{max}\sigma_z)^2]}, \tag{A.12}$$

where

$$C_{const} = 10^{[-0.0437+0.8644 \log C_{ch,0} - 0.0883(\log C_{ch,0})^2]}, \tag{A.13}$$

$$\begin{aligned} C_m \ &= \ 0.269 + 0.245 \log C_{ch,0} + 1.51(\log C_{ch,0})^2 \\ &\quad +2.13(\log C_{ch,0})^3 + 0.814(\log C_{ch,0})^4, \end{aligned} \tag{A.14}$$

$$\begin{aligned} h_{max} \ &= \ 17.9 - 44.6 \log C_{ch,0} + 38.1(\log C_{ch,0})^2 \\ &\quad +1.32(\log C_{ch,0})^3 - 10.7(\log C_{ch,0})^4, \end{aligned} \tag{A.15}$$

and

$$\begin{aligned} \sigma_z \ &= \ 0.01 \Big[4.08 + 2.17 \log C_{ch,0} + 0.239(\log C_{ch,0})^2 \\ &\quad +0.562(\log C_{ch,0})^3 + 0.514(\log C_{ch,0})^4\Big], \end{aligned} \tag{A.16}$$

and the surface concentration of chlorophyll is assumed to be $C_{ch,0} = C_{ch}(0) = 0.1\,\mathrm{mg/m^3}$ [162].

The last term $a_d$ in Eq. (A.6) accounts for the absorption due to suspended oil droplets, which depends on the droplet number density $N_d$ and droplet diameter $d$. It can be modeled based on Mie theory as [57, 105, 145]

$$a_d(d, N_d; \lambda_l) = (\pi d^2/4)\, Q_{ab}(d; \lambda_l)\, N_d, \tag{A.17}$$

where $Q_{ab}$ is the absorption efficiency. Details on how to model $Q_{ab}$ using Mie theory are given further below.

The light scattering coefficient $b$ can be modeled as [137, 145]

$$b(C_{ch}, d, N_d; \lambda_l) = b_w(\lambda_l) + b_{\scriptscriptstyle SPM}(C_{ch}; \lambda_l) + b_d(d, N_d; \lambda_l). \tag{A.18}$$

Here, $b_w$ corresponds to the scattering caused by water molecules,

$$b_w(\lambda_l) = 5.83{\times}10^{-3}(\lambda_{l,r}/\lambda_l)^{4.322}. \tag{A.19}$$

Besides, $b_{\scriptscriptstyle SPM}$ corresponds to the scattering caused by the SPM,

$$b_{\scriptscriptstyle SPM}(C_{ch}; \lambda_l) = b_s^*(\lambda_l)C_s(C_{ch}) + b_l^*(\lambda_l)C_l(C_{ch}), \tag{A.20}$$

where $b_s^*$ (measured in $\mathrm{m}^2/\mathrm{mg}$) and $C_s$ (measured in $\mathrm{mg}/\mathrm{m}^3$) are the specific scattering coefficient and concentration of small-size SPM, respectively, and $b_l^*$ and $C_l$ are the corresponding quantities for large-size SPM. They can be parameterized as [53, 137]

$$b_s^*(\lambda_l) = 1.513{\times}10^{-3}\,(\lambda_{l,r}/\lambda_l)^{1.7}\,, \tag{A.21}$$

$$b_l^*(\lambda_l) = 3.411{\times}10^{-4}\,(\lambda_{l,r}/\lambda_l)^{0.3}\,, \tag{A.22}$$

$$C_s(C_{ch}) = 17.39 C_{ch} \exp\left(0.11631 C_{ch}\right), \tag{A.23}$$

and

$$C_l(C_{ch}) = 762.84 C_{ch} \exp\left(0.03092 C_{ch}\right). \tag{A.24}$$

The last term $b_d$ accounts for the scattering due to suspended oil, which can be modeled based on Mie theory as [57, 105, 145]

$$b_d(d, N_d; \lambda_l) = (\pi d^2/4)\, Q_{sc}(d; \lambda_l)\, N_d, \tag{A.25}$$

where $Q_{sc}$ is the scattering efficiency. Details on how to model $Q_{sc}$ using Mie theory are given further below.

The scattering direction is determined by the total scattering phase function, which is expressed as a weighted sum of the three contributions [145],

$$\begin{aligned} B(\Delta\theta, C_{ch}, d, N_d; \lambda_l) \; &= \; \frac{B_w(\Delta\theta; \lambda_l) b_w(\lambda_l)}{b(C_{ch}, d, N_d; \lambda_l)} + \frac{B_{SPM}(\Delta\theta) b_{SPM}(\lambda_l)}{b(C_{ch}, d, N_d; \lambda_l)} \\ &+ \frac{B_d(\Delta\theta; \lambda_l) b_d(d, N_d; \lambda_l)}{b(C_{ch}, d, N_d; \lambda_l)}, \end{aligned} \tag{A.26}$$

where $\Delta\theta$ is the relative polar angle away from the incident direction due to scattering, and $B_w(\Delta\theta; \lambda_l)$, $B_{SPM}(\Delta\theta)$ and $B_d(\Delta\theta, \lambda_l)$ are the scattering phase functions of seawater, SPM, and other particles, respectively. Values for $B_w(\Delta\theta; \lambda_l)$ can be found in [98, 100]; $B_{SPM}(\Delta\theta)$ is modeled by the Petzold phase function [113, 137, 145]; and $B_d(\Delta\theta, \lambda_l)$ is modeled based on Mie theory with details given below. Note that in Eq. (A.26) the dependance on the change of azimuthal angle $\varphi$ is not included by assuming homogeneity of the scattering direction with respect to $\varphi$.

Figure A.1 shows the result of a MCS test case for radiative transfer of 500 nm light in a natural ocean condition (without oil) with a mean surface chlorophyll concentration of $C_{ch,0} = 1\,\mathrm{mg/m^3}$, where the prediction based on the empirical model of [163] is shown using the symbols and the current MCS result is shown using the solid line. In this test case, a calm sea condition is assumed so that the sea-surface is modeled to be flat.. In this test case the vertical profile of the chlorophyll concentration is modeled based on Eq. (A.12) and $C_{ch,0}$; the corresponding seawater absorption and scattering coefficients are modeled based on Eqs. (A.6) and (A.18); and the scattering phase function is modeled based on Eq. (A.26). The corresponding diffuse attenuation coefficient $K_d$ as a function of the vertical coordinate $z$ can be calculated based on the empirical model as [162, 163]:

$$K_d(z) = K_w + C_{ch}(z)\{C_1 \exp[-a_1 C_{ch}(z)] + K_{d,i}\}. \tag{A.27}$$

For the $\lambda_l = 500\,\mathrm{nm}$ light, the model constants are $K_w = 0.0276\,\mathrm{m^{-1}}$, $C_1 = 0.0672\,\mathrm{m^2/mg}$, $a_1 = 0.610\,\mathrm{m^3/mg}$, and $K_{d,i} = 0.0389\,\mathrm{m^2/mg}$. Overall, the vertical profile of $\langle E_d \rangle$ obtained from the current MCS model shows good agreement with the exponential decay profile $\langle E_d \rangle(z) = \langle E_{d,0} \rangle \exp[\int_0^z K_d(\zeta)\mathrm{d}\zeta]$ predicted by the empirical model of [163], where the $K_d$ profile is given by Eq. (A.27).

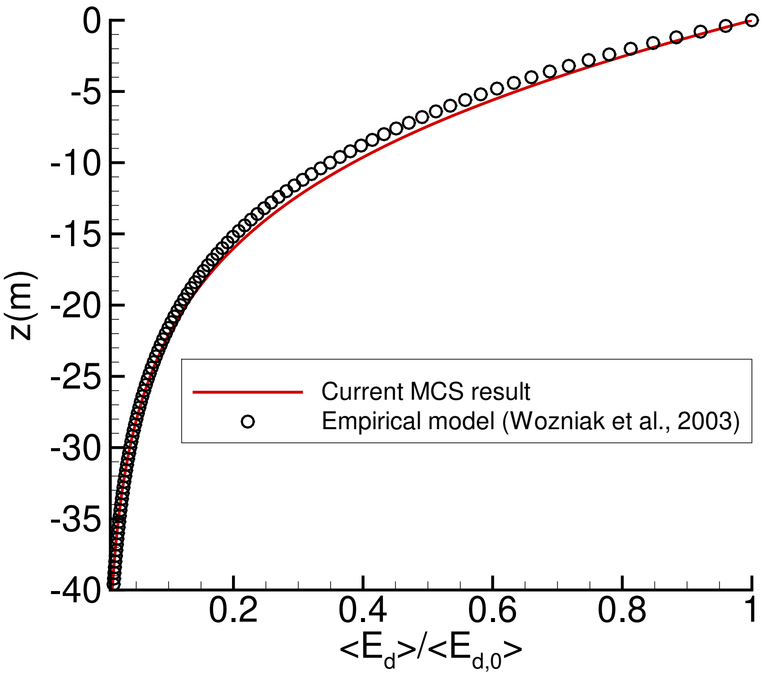


Figure A.1: Vertical attenuation of horizontally averaged downward irradiance in seawater with a mean surface chlorophyll concentration of $C_{ch,0} = 1\,\mathrm{mg/m^3}$.

### A.2.2 Modeling light scattering by oil droplets based on Mie theory

The corresponding absorbing and scattering coefficient of oil droplets can be calculated via Mie theory [13, 97]. In particular, the extinction efficiency $Q_{ex}$, scattering efficiency $Q_{sc}$ and absorption efficiency $Q_{ab}$ due to suspended oil droplets are calculated as [13]

$$Q_{sc}=\frac{2}{\chi^2}\sum_{n=1}^{\infty}(2n+1)(|a_n|^2+|b_n|^2), \tag{A.28}$$

$$Q_{ex}=\frac{2}{\chi^2}\sum_{n=1}^{\infty}(2n+1)[\Re(a_n+b_n)], \tag{A.29}$$

and

$$Q_{ab}=Q_{ex}-Q_{sc}, \tag{A.30}$$

where $\chi = \pi d/\lambda_l$ is the diffraction parameter, $\Re(\cdot)$ is the real part of the sum of the complex numbers $a_n$ and $b_n$,

$$a_n = \frac{[D_n(m\chi)/m + n/\chi]\psi_n(\chi) - \psi_{n-1}(\chi)}{[D_n(m\chi)/m + n/\chi]\xi_n(\chi) - \xi_{n-1}(\chi)}, \tag{A.31}$$

and

$$b_n = \frac{[D_n(m\chi)m + n/\chi]\psi_n(\chi) - \psi_{n-1}(\chi)}{[D_n(m\chi)m + n/\chi]\xi_n(\chi) - \xi_{n-1}(\chi)}. \tag{A.32}$$

$m = n_d/n_w$ is the relative refractive index, $n_d$ is the refractive index of oil droplet, $n_w$ is the refractive index of seawater, and $D_n(\varrho) = \mathrm{d}(\ln\psi_n(\varrho))/\mathrm{d}\varrho$ is the logarithmic derivative, which satisfies the recurrence relation

$$D_{n-1}(\varrho) = \frac{n}{\varrho} - \frac{1}{D_n(\varrho)+n/\varrho}. \tag{A.33}$$

The Ricatti–Bessel functions $\psi_n(x)$ and $\xi_n(x)$ satisfy the following upward recurrence relation [13]

$$\psi_{n+1}(\chi)=\frac{2n+1}{\chi}\psi_n(\chi)-\psi_{n-1}(\chi), \tag{A.34}$$

and

$$\xi_{n+1}(\chi)=\frac{2n+1}{\chi}\xi_n(\chi)-\xi_{n-1}(\chi), \tag{A.35}$$

beginning with and

$$\psi_0(\chi) = \sin(\chi), \tag{A.36}$$

$$\psi_{-1}(\chi) = \cos(\chi), \tag{A.37}$$

$$\xi_0(\chi) = \sin(\chi) - i\cos(\chi), \tag{A.38}$$

and

$$\xi_{-1}(\chi) = \cos(\chi) + i\sin(\chi), \tag{A.39}$$

where $i = \sqrt{-1}$. In this chapter, the complex refractive index of spherical oil droplet is set to be $n_d = 1.494 + 0.0089\, i$ for light with wavelength $\lambda_l = 450\,\mathrm{nm}$ [106], and the refractive index of seawater is $n_w = 1.34$.

The scattering function due to oil droplets can also be determined based on $a_n$ and $b_n$ as [13, 48]

$$P_d(\Delta\theta) = \frac{2}{\chi^2 Q_{sc}}(|S_1(\Delta\theta)|^2 + |S_2(\Delta\theta)|^2), \tag{A.40}$$

where $S_1$ and $S_2$ are the amplitude functions,

$$S_1(\Delta\theta) = \sum_{n=1}^{\infty} \frac{2n+1}{n(n+1)}[a_n\pi_n(\cos\Delta\theta) + b_n\tau_n(\cos\Delta\theta)], \tag{A.41}$$

and

$$S_2(\Delta\theta) = \sum_{n=1}^{\infty} \frac{2n+1}{n(n+1)}[a_n\tau_n(\cos\Delta\theta) + b_n\pi_n(\cos\Delta\theta)]. \tag{A.42}$$

Here, the angular functions $\pi_n$ and $\tau_n$ are defined as $\pi_n = P_n^1/\sin\Delta\theta$ and $\tau_n = \mathrm{d}P_n^1/\mathrm{d}(\Delta\theta)$, where $P_n^1$ are the associated Legendre functions of the first kind of degree $n$ and order 1. In the simulation, $\pi_n$ and $\tau_n$ can be calculated based on the following upward recurrence relations [13],

$$\pi_n(\varsigma) = \frac{2n-1}{n-1}\varsigma\pi_{n-1}(\varsigma) - \frac{n}{n-1}\pi_{n-2}(\varsigma), \tag{A.43}$$

and

$$\tau_n(\varsigma) = n\varsigma\pi_n(\varsigma) - (n+1)\pi_{n-1}(\varsigma), \tag{A.44}$$

beginning with

$$\pi_1(\varsigma) = 1, \tag{A.45}$$

and

$$\pi_0(\varsigma) = 0, \tag{A.46}$$

where $\varsigma = \cos\Delta\theta$. The scattering phase function used in Eq. (A.26) can then be obtained as $B_d = P_d/4\pi$.

Figure A.2 shows some sample results for the scattering phase functions for various diffraction parameters obtained using Mie theory, where the values calculated by Mie theory module in the current MCS model are shown by the solid lines, and the values reported by [48] (also based on Mie theory) are shown by the symbols.. The results computed by Mie theory scattering module in the current MCS model are plotted together with the theoretical results from [48]. Note that the values from [48] are reproduced by digitalizing the results reported in their Fig. 5, so some small artificial errors may be induced during this image digitalization process. Nevertheless, Fig. A.2 shows good agreement between the two independent calculations, which shows that the Mie scattering model is implemented correctly in the current MCS model framework.

It should be noted that Mie theory may not always provide accurate prediction of the volume scattering functions for nonspherical particles. The oil droplets dispersed in the upper ocean boundary layer may exhibit noticeable deformations due to the forcing induced by the oceanic flows (such as turbulence and waves), which has not been well studied due to the complex physical processes involved. Moreover, to the best of the authors' knowledge, up to date there is no reliable and accurate empirical models for the volume scattering functions of oil–seawater mixture in a dynamic ocean environment. Like what is pointed out by [13], for the complex problem studied in this chapter, Mie theory seems to be one of the only few feasible methods for modeling the light-scattering properties of the oil-contaminated seawater. However, if new advancements are made in the future on the empirical or theoretical modeling of the effects of oil droplets on light scattering, the current MCS model can be readily improved by implementing these new scattering models to replace the existing Mie theory module.

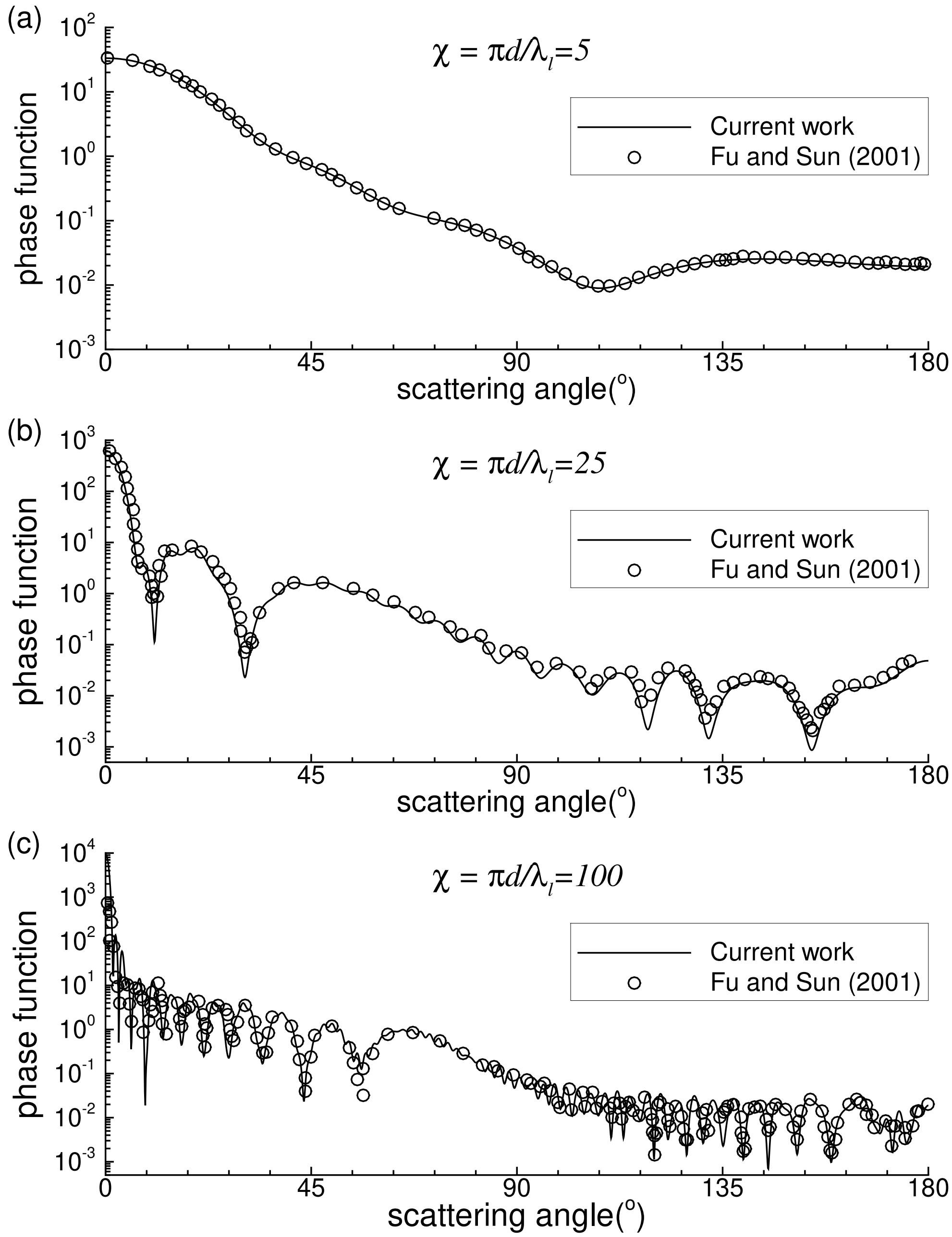


Figure A.2: Scattering phase function as a function of the scattering angle for spherical particles with diffraction parameters: (a) $\chi = 5$; (b) $\chi = 25$; (c) $\chi = 100$. Here, the particle's refractive index is set to be $n_d = 1.0$ and the medium's refractive index is set to be 1.34.

### A.2.3 Light refraction at the air–water interface

When an unpolarized light enters the water through the air–water interface, the refraction follows the Snell's law [98]:

$$n_a \sin(\gamma_i) = n_w \sin(\gamma_t), \tag{A.47}$$

where $\gamma_i$ is the incident angle with respect to the interface normal direction, $\gamma_t$ is the transmitted angle on the water side, and $n_a$ and $n_w$ are the optical refractive indices of air and water, respectively. The reflectance $r$ of the radiant energy is given by the Fresnel equations [98]:

$$r = \begin{cases} \dfrac{1}{2}\left\{\left[\dfrac{\sin(\gamma_i - \gamma_t)}{\sin(\gamma_i + \gamma_t)}\right]^2 + \left[\dfrac{\tan(\gamma_i - \gamma_t)}{\tan(\gamma_i + \gamma_t)}\right]^2\right\}, & \text{if } \gamma_i \neq 0, \\ \left(\dfrac{n_a - n_w}{n_a + n_w}\right)^2, & \text{if } \gamma_i = 0. \end{cases} \tag{A.48}$$

In the MCS model, for a photon packet passing the air–water interface, the refraction of its trajectory is modeled based on Eq. (A.47) and the transmitted energy that the photon packet carries into the water is $E_t = E_i(1 - r)$, where $E_i$ is the incident energy of the photon packet and $r$ is determined by Eq. (A.48) [77].

Figure A.3 shows the downward irradiance $E_d$ in the seawater without oil plumes for the LC and CC cases. For comparison, an additional reference case with a flat sea surface is also shown. This figure illustrate the effect of sea-surface waves for the downward irradiance shown in Figs. 3.8 and 3.9. The presence of the sea-surface wave field causes a small fraction of the incident light energy to reflect back to the air, resulting smaller downward irradiance under the wave surface than that under the flat water surface (corresponding to the idealized calm-sea condition). Note that the wave fields in the LC and CC cases obey the same empirical wave spectrum model from [40]. Although the peak wavelengths of sea-surface waves in these two cases are different (see Section 3.3.1), the surface slopes of the waves in the high wavenumber range are similar between the two cases, resulting in similar initial downward irradiance underneath the wave surface. The downward irradiances for the LC and CC cases obtained without oil plumes are used as the reference value $E_{d,r}$ in Figs. 3.8(d) and 3.9(d) for obtaining the oil-induced deficit.

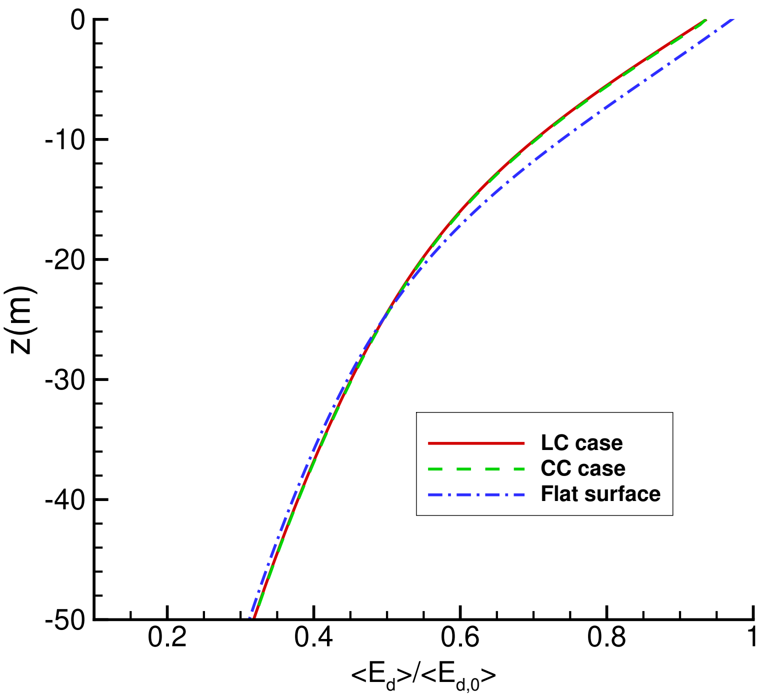


Figure A.3: Vertical profiles of horizontally averaged downward irradiance $\langle E_d \rangle$ in the seawater without oil plumes. The profiles are normalized by the reference value of the incident light $\langle E_{d,0} \rangle$ at the sea surface.